Theory of Charge and Flux Noise in Superconducting Wires

by

José Alberto Nava Aquino
B.Sc., Universidad Nacional Autónoma de México, 2017

A Dissertation Submitted in Partial Fulfillment of the
Requirements for the Degree of

DOCTOR OF PHILOSOPHY

in the Department of Physics and Astronomy

University of Victoria

Theory of Charge and Flux Noise in Superconducting Wires

by

José Alberto Nava Aquino
B.Sc., Universidad Nacional Autónoma de México, 2017

Supervisory Committee

Dr. Rogério de Sousa, Supervisor
(Department of Physics and Astronomy)

Dr. Pavel Kovtun, Departmental Member
(Department of Physics and Astronomy)

Dr. Mohammad Amin, Outside Member
(D-Wave Systems)

Abstract

Superconducting qubits are at the forefront of efforts to develop scalable quantum computers due to their potential to perform complex computations beyond the capabilities of classical systems. However, maintaining the quantum coherence of these qubits remains a significant challenge, primarily due to various noise sources such as flux noise, dielectric loss, and quasiparticle poisoning. This dissertation presents a detailed theoretical investigation into two noise mechanisms affecting superconducting qubits: flux noise from spin impurities and charge/flux noise from non-equilibrium superconducting quasiparticle distributions.

The first part of the research focuses on developing a general theoretical framework to calculate flux noise arising from spin impurities. This framework accounts for spin diffusion and spin-lattice relaxation, incorporating a discrete diffusion model to handle confinement effects and inhomogeneities. Analytical and numerical results show that the spin relaxation model aligns with experimental observations in aluminum devices, while the spin diffusion model better matches experiments in niobium devices.

The second part of the thesis proposes a theory addressing charge and flux noise due to non-equilibrium superconducting quasiparticle distributions within superconducting wires. This theory highlights the significant impact of ohmic loss generated by these quasiparticles, revealing their contribution to charge noise at intermediate frequencies and a nearly white flux noise background.

Comparative analysis with experimental data provides some validation for the theoretical models and gives insights into the temperature-dependent behavior of flux noise and the distinctive noise characteristics in aluminum and niobium devices. The findings highlight the necessity of addressing wire-resident quasiparticles and magnetic impurities to enhance the performance and scalability of superconducting qubits.

Table of Contents

Supervisory Committee ii

Abstract iii

Table of Contents iv

List of Figures viii

List of Publications x

List of Acronyms xi

Acknowledgements xiii

Dedication xiv

1 Introduction 1

2 Superconductivity and Superconducting Qubits 4

2.1 Superconductivity 4

2.1.1 The London Equations 5

2.1.2 Ginzburg-Landau Theory 9

2.1.3 Josephson Relations 10

2.1.4 Quantization of Magnetic Flux 11

2.2 Superconducting Qubits . . . 12
2.2.1 LC Resonator . . . 13
2.2.2 Transmon . . . 14
2.2.3 Flux-Tunable Transmon . . . 16
2.2.4 rf-SQUID as Flux Qubit . . . 18
2.2.5 Fluxonium . . . 20

3 Noise in Superconducting Qubits **22**
3.1 Noise and Decoherence . . . 22
3.1.1 Bloch-Sphere Representation . . . 22
3.1.2 Relaxation . . . 23
3.1.3 Dephasing . . . 24
3.1.4 Noise Power Spectral Density . . . 26
3.1.5 Bloch–Wangsness–Redfield Master Equation . . . 27
3.2 Sources of Decoherence in Superconducting Qubits . . . 28
3.2.1 Flux Noise . . . 28
3.2.2 Flux Noise in Aluminum Devices . . . 30
3.2.3 Flux Noise in Niobium Devices . . . 31
3.2.4 Charge Noise . . . 32
3.2.5 Non-equilibrium Superconducting Quasiparticle Distributions . . . 33

4 General Spin Dissipation Theory of Flux Noise **34**
4.1 Introduction . . . 34
4.2 Spin Flux Noise Model . . . 36
4.3 General Spin Dissipation Model . . . 37
4.3.1 Free Energy in the Mean Field Approximation . . . 37
4.3.2 Spin Dynamics . . . 40
4.3.3 Dissipation Matrix . . . 42
4.4 Conclusions . . . 45

5 Flux Noise due to Spin-Lattice Relaxation and Dependence on External Magnetic Fields **46**

5.1 Introduction . . . 46
5.2 Single Spin Model . . . 47
5.3 Impact of Cross Relaxation . . . 52
5.3.1 Cross Relaxation . . . 52
5.3.2 Disorder in a Spin Ensemble: $1/f$ Noise . . . 53
5.4 Impact of Direct Spin Relaxation . . . 55
5.4.1 Direct Relaxation . . . 55
5.4.2 Reduced Disorder: $1/f$ to Lorentzian Noise . . . 55
5.5 Conclusions . . . 58

6 Flux Noise Results in the General Spin Dissipation Theory **59**

6.1 Introduction . . . 59
6.2 General Results . . . 59
6.2.1 Linear Equation of Motion . . . 59
6.2.2 Dynamical Susceptibilities . . . 61
6.2.3 Flux Noise and Paramagnon Density . . . 62
6.3 Homogeneous Magnet in the Paramagnetic Phase . . . 63
6.3.1 Susceptibility and Spin Noise . . . 64
6.3.2 Flux Noise and Paramagnon Flux Density . . . 68
6.3.3 Long Wavelength Regime . . . 69
6.3.4 Phenomenological Flux Noise Model in a Homogeneous Magnet in the Paramagnetic Phase . . . 70
6.4 Confined Magnet in the Paramagnetic Phase . . . 74
6.4.1 Impact of Confinement . . . 74
6.4.2 Impact of Disorder due to Vacancies . . . 77
6.4.3 Impact of Disorder due to a Wide Distribution of Relaxation Rates . . . 78
6.5 Conclusions . . . 79

7 Charge and Flux Noise from Wire-Resident Superconducting Quasiparticles **80**

7.1 Introduction 80

7.2 Conductivity of a Superconductor in Mattis-Bardeen Theory 81

7.3 Effective Impedance Model of Quasiparticles 86

7.3.1 Dynamical Susceptibility 86

7.3.2 Quasithermal Energy Distribution 87

7.3.3 Charge Noise 87

7.3.4 Flux Noise 90

7.4 Conclusions 92

8 Conclusions **93**

Bibliography **98**

A Generalized Fluctuation-Dissipation Theorem **110**

List of Figures

2.1 Temperature dependence of the resistance of a superconductor and a normal metal. 6
2.2 The Meissner effect in a sphere of superconducting material. 7
2.3 Temperature dependence of the critical field in a type I superconductor. 8
2.4 A Josephson Junction. 10
2.5 Superconducting ring. 12
2.6 LC resonator. 15
2.7 Transmon. 17
2.8 Flux-tunable transmon. 18
2.9 rf-SQUID in an external flux. 20
2.10 The rf-SQUID double-well potential. 21
2.11 Fluxonium qubit. 21

3.1 Bloch Sphere 23
3.2 Longitudinal (T_1) and transverse (T_2) relaxation times measurements of a transmon qubit. 26
3.3 Frequency and temperature dependence of flux noise in Al 30
3.4 Magnetic field dependence of flux noise in Al 31
3.5 Temperature dependence of exponent α and amplitude A^2 in Nb 32

5.1 Single spin on the surface of the superconducting wire 47
5.2 Spin noise produced by a single spin in a magnetic field $\boldsymbol{h}^{\mathrm{eq}}$ 51
5.3 $1/f$ flux noise from a wide distribution of spins 54
5.4 Energy level structure for a spin coupled to an amorphous TLS 56
5.5 $1/f$ to lorentzian flux noise due to a magnetic field 57

6.1 Infinite plane of spins . . . 64
6.2 Frequency dependence of flux noise in an infinite ferromagnet in the paramagnetic phase . . . 67
6.3 Frequency dependence of flux noise in an infinite antiferromagnet in the paramagnetic phase . . . 68
6.4 Frequency dependence of the paramagnon flux density in an infinite magnet . . . 71
6.5 Temperature dependence of flux noise in an infinite magnet . . . 72
6.6 Section of a superconducting wire with spin impurities randomly distributed on its surface. . . . 74
6.7 Frequency dependence of flux noise in a confined ferromagnet in the paramagnetic phase . . . 75
6.8 Frequency dependence of flux noise in a confined antiferromagnet in the paramagnetic phase . . . 76
6.9 Temperature dependence of flux noise in a confined magnet . . . 77
6.10 Spin density dependence of exponent α . . . 78
6.11 Impact of spin-lattice relaxation in exponent α . . . 79

7.1 Origin of non-equilibrium quasiparticle densities at low temperatures . . . 82
7.2 Numerical calculation of $\sigma_1(\omega)$ . . . 86
7.3 Charge noise from wire-resident QPs compared to capacitive dielectric loss, $\ell =$ 1.5 mm . . . 88
7.4 Charge noise from wire-resident QPs compared to capacitive dielectric loss, $\ell =$ 15 mm . . . 89
7.5 Flux noise from wire-resident QPs, $\ell = 1.5$ mm . . . 91

List of Publications

The work presented in this dissertation can be found in the following publications:

- José Alberto Nava Aquino and Rogério de Sousa. Flux noise in disordered spin systems. *Phys. Rev. B.*, 106:144506, October 2022. URL https://doi.org/10.1103/PhysRevB.106.144506.
  Chapters 4 and 6 are based on this work.

- José Alberto Nava Aquino and Rogério de Sousa. Model for 1/f flux noise in superconducting aluminum devices: Impact of external magnetic fields. *Applied Physics Letters*, 122(22): 224003, 06 2023. URL https://doi.org/10.1063/5.0147500.
  Chapter 5 is based on this work.

- José Alberto Nava Aquino and Rogério de Sousa. Charge and flux noise from nonequilibrium quasiparticle energy distributions in superconducting wires, 2024. URL https://doi.org/10.48550/arXiv.2407.21177.
  Chapter 7 is based on this work.

List of Acronyms

SC Superconducting

QP Quasiparticle

BCS Bardeen–Cooper–Schrieffer

Al Aluminum

Nb Niobium

SQUID Superconducting Quantum Interference Device

QHO Quantum Harmonic Oscillator

AHO Anharmonic Oscillator

PSD Power Spectral Density

TLS Two-Level System

BWR Bloch-Wangsness-Redfield

FM Ferromagnetic

AFM Antiferromagnetic

NN Nearest Neighbour

b.c. Boundary Conditions

HA Homogeneous Approximation

CPW Coplanar Waveguide

Acknowledgements

I would like to thank:

My family and Jen, for support and encouragement throughout this process.

Dr. Rogério de Sousa, for mentoring and guidance throughout the Ph.D.

My supervisory committee, for taking the time to review my thesis and for the useful comments and suggestions.

My friends, for companionship, and the memorable moments we shared.

D-Wave systems, for the opportunity to intern with them in 2023.

EQuS group at MIT, for hosting me during my research visit in 2024.

What songs the Sirens sang?
What name Achilles assumed when he hid himself among women?
Although puzzling questions are not beyond all conjecture.
Sir Thomas Browne.

Dedication

A mis padres y familia, por apoyarme a lo largo de los años.

CHAPTER 1

Introduction

Superconducting (SC) qubits, pivotal in the pursuit of scalable quantum computing [4], are highly susceptible to various types of noise that can significantly degrade their performance. These qubits, leveraging the principles of superconductivity and quantum mechanics, hold great promise for performing complex computations far beyond the capabilities of classical computers. However, their practical realization is limited by persistent noise issues that undermine their coherence and fidelity.

The primary sources of noise in SC devices include flux noise [5–8], dielectric loss [9, 10], and quasiparticle (QP) poisoning [11–13]. Flux noise, caused by fluctuating magnetic dipoles intrinsic to the materials forming the SC circuits, leads to decoherence and energy dissipation. Dielectric loss, which arises from electric dipoles intrinsic to these materials, further contributes to decoherence. QP poisoning, involving the presence of excitations of the SC material (QPs), introduces additional complications, making the SC resistive, leading to unwanted energy dissipation.

Addressing and mitigating these noise sources is crucial for advancing SC qubit technology and realizing its full potential. Without effective noise reduction strategies, quantum computers' scalability and practical application remain limited. Therefore, understanding the mechanisms behind these noise sources and developing robust theoretical models to predict and counteract their effects is important for the field of quantum computing.

This dissertation presents a comprehensive theoretical framework for calculating flux noise from spin impurities. This framework accounts for the impact of both spin diffusion and spin-lattice relaxation in flux noise. A key feature of this theory is the introduction of a discrete version of diffusion, which can model confinement effects and accommodate systems with finite

boundaries. Additionally, it considers vacancies, clusters, and external magnetic fields, making it general and adaptable. This framework also incorporates spin-lattice relaxation, allowing for energy exchange between spins and the lattice. Furthermore, we propose a second theory focused on charge and flux noise arising from non-equilibrium SC QP distributions within the SC wire. This theory highlights the often-overlooked contribution of ohmic loss generated by these QPs, revealing that their impact can be substantial.

The results of my research are divided into two main parts, corresponding to the two proposed theories.

Firstly, within the spin dissipation (diffusion and relaxation) framework, analytical calculations of flux noise can be obtained in two specific scenarios: considering only spin-lattice relaxation and accounting for spin diffusion in a homogeneous, infinite spin system. Additionally, we obtain numerical results for the general case, which includes both mechanisms and considers disorder and confinement effects. These results suggest that a spin relaxation model aligns qualitatively with experimental observations in aluminum (Al) devices, while a spin diffusion model better matches experiments in niobium (Nb) devices.

Secondly, the theory of charge and flux noise due to non-equilibrium QP distributions reveals that QPs can contribute significantly to charge noise at intermediate frequencies (in the MHz range) and produce current fluctuations that, via inductance, generate a nearly white flux noise background. This background noise aligns well with experimental data, highlighting the importance of wire-resident QPs in understanding noise in SC qubits.

The research presented here provides a deeper understanding of noise mechanisms and proposes models to calculate their contributions.

This document is structured as follows:

Chapter 1 contains the introduction and summarizes the contents in the dissertation.

Chapter 2 provides an introduction to superconductivity and SC qubits, offering the necessary background for understanding the fundamental concepts that are the focus of this research.

Chapter 3 discusses noise and decoherence in SC qubits, identifying the key challenges and their implications for qubit performance.

Chapter 4 presents a general theoretical framework for the calculation of flux noise from impurity spins, accounting for both spin-spin interactions and spin-lattice relaxation.

Chapter 5 presents results considering spin-lattice relaxation only and the impact of external magnetic fields in flux noise, including analytical calculations.

Chapter 6 presents results that account for both spin relaxation and spin diffusion mechanisms, with a focus on numerical analysis and its agreement with experimental observations.

Chapter 7 presents the theory of charge and flux noise due to non-equilibrium SC QP distributions residing within SC wires, detailing the theoretical predictions.

Chapter 8 contains conclusions, summarizing the key findings of the research, discussing their implications, and suggesting potential directions for future work.

CHAPTER 2

Superconductivity and Superconducting Qubits

Before delving into the main topic of this dissertation, noise from wires in SC qubits, it is necessary to introduce a foundational understanding of superconductivity and SC qubits. Section 2.1 provides a summary of the phenomenology of superconductivity based on References [14–16]. Section 2.2 provides a summary and introduction to SC qubits based on References [17–20].

2.1 Superconductivity

Superconductivity, discovered in 1911 by H. Kamerlingh Onnes [21], was first observed when metals like mercury, lead, and tin exhibited *zero electrical resistance* when cooled below a characteristic critical temperature T_c, unique to each material. In contrast, typical metals show a gradual reduction in electrical resistance as temperature decreases; see Fig 2.1. Superconductors also exhibit *perfect diamagnetism*, meaning they expel magnetic fields from their interior (Meissner effect). This behavior is distinct from perfect conductors, which would allow magnetic fields to be frozen in their interior, see Fig. 2.2.

Microscopically, superconductivity is explained by the formation of Cooper pairs, where two electrons with opposite spins and momenta form a bound state due to attractive interactions mediated by lattice vibrations (phonons), as explained by The Bardeen-Cooper-Schrieffer (BCS) theory [22]. The formation of these pairs opens up an energy gap Δ in the electronic density of states. This gap means that a minimum amount of energy 2Δ is required to break a Cooper pair and create excitations. In the normal state, the density of states at the Fermi level is ρ_0.

However, in the superconducting state, the density of states is modified and given by:

$$\rho(E) = \rho_0 \frac{E}{\sqrt{E^2 - \Delta^2}}, \tag{2.1}$$

where $E \equiv E = \sqrt{\xi^2 + \Delta^2}$ is the BCS QP energy (excitations of the SC condensate), with ξ the free electron energy measured from the Fermi level. This equation shows that there are no states available within the energy gap $|E| < \Delta$, and the density of states diverges at the gap edge $E = \pm\Delta$.

Superconductors are classified into two types:

- **Type I Superconductors**: These have a single critical magnetic field, H_c, and exhibit a complete Meissner effect up to this field. For fields greater than H_c, the superconducting state is destroyed. Empirical findings show that $H_c(T)$ is well approximated by a parabolic relationship:

  $$H_c(T) \approx H_c(0)[1 - (T/T_c)^2] \tag{2.2}$$

  as illustrated in Fig. 2.3.

- **Type II Superconductors**: These have two critical fields, H_{c1} and H_{c2}. Between these fields, they exhibit a mixed state where magnetic vortices penetrate the material. The magnetic field penetrates the superconductor in the form of quantized flux tubes or vortices. The lower critical field H_{c1} marks the onset of vortex penetration, while the upper critical field H_{c2} marks the field strength at which superconductivity is completely destroyed.

2.1.1 The London Equations

The two main electrodynamic properties of superconductivity (zero resistance and perfect diamagnetism) were effectively described in 1935 by the London brothers [24] who proposed two phenomenological equations:

$$\boldsymbol{E} = \frac{\partial}{\partial t}(\Lambda \boldsymbol{J}_s), \tag{2.3}$$

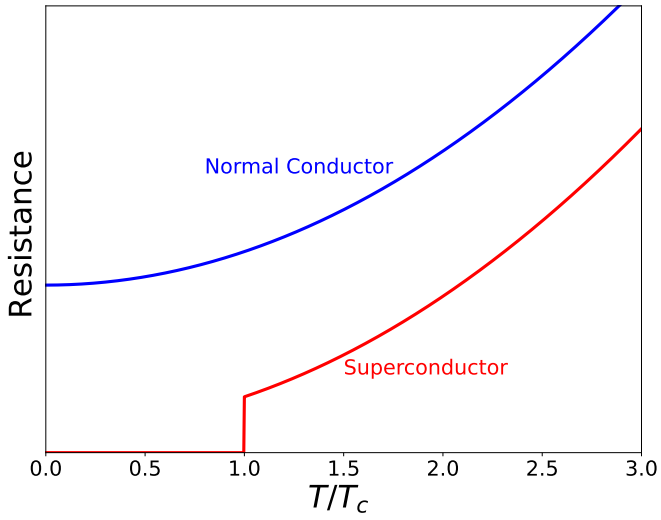

Figure 2.1: ***Temperature dependence of the resistance of a superconductor and a normal metal.***

$$\boldsymbol{B} = -\nabla \times (\Lambda \boldsymbol{J}_s), \tag{2.4}$$

where

$$\Lambda = \mu_0 \lambda^2 \tag{2.5}$$

is a phenomenological parameter, with $\boldsymbol{E}$ and $\boldsymbol{B}$ representing the electric and magnetic fields respectively, λ is the *penetration depth* and $\boldsymbol{J}_s$ being the supercurrent density.

Although the London equations were based on experimental observations and not derived from first principles, we can still offer a simple derivation from a classical approach. In the standard Drude model of electrical conductivity, applying classical mechanics to electron motion gives us:

$$m\frac{d\boldsymbol{v}}{dt} = e\boldsymbol{E} - m\frac{\boldsymbol{v}}{\tau}, \tag{2.6}$$

where $\boldsymbol{v}$ is the average or "drift" velocity of the electrons, and τ is a phenomenological relaxation time representing the time it takes for scattering from defects to nullify the drift velocity of the electrons. In normal metals, the steady-state drift velocity is $\boldsymbol{v} = e\boldsymbol{E}\tau/m$. For conduction

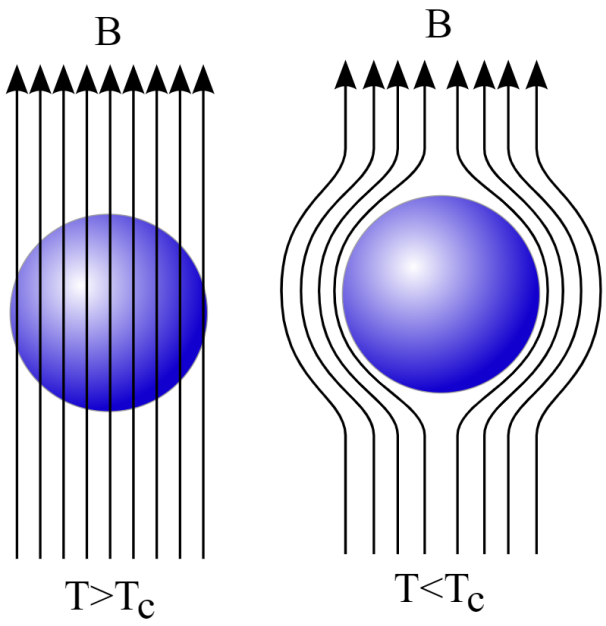

Figure 2.2: ***The Meissner effect in a sphere of superconducting material.***
As the temperature is lowered below the critical temperature T_c, the external magnetic field is expelled. Figure taken from Ref. [23].

electrons per unit volume n, this generates an electric current density $\boldsymbol{J} = ne\boldsymbol{v} = (ne^2\tau/m)\boldsymbol{E} = \sigma\boldsymbol{E}$, which is Ohm's law.

To describe the perfect conductivity of a superconductor, we can postulate that a certain density n_s of electrons behaves as if there were no scattering term (by letting $\tau \to \infty$). Thus, we have $d\boldsymbol{v}_s/dt = e\boldsymbol{E}/m$, leading to an equation of motion for the total supercurrent $\boldsymbol{J}_s$

$$\frac{d\boldsymbol{J}_s}{dt} = (n_s e^2/m)\boldsymbol{E} = \boldsymbol{E}/\Lambda = (1/\mu_0\lambda^2)\boldsymbol{E}, \tag{2.7}$$

which corresponds to the first London equation along with the definition (2.5) of Λ and λ. From this, we can estimate the penetration depth,

$$\lambda^2 = \frac{m}{\mu_0 n_s e^2}. \tag{2.8}$$

Equation (2.3) describes perfect conductivity since any electric field accelerates the supercon-

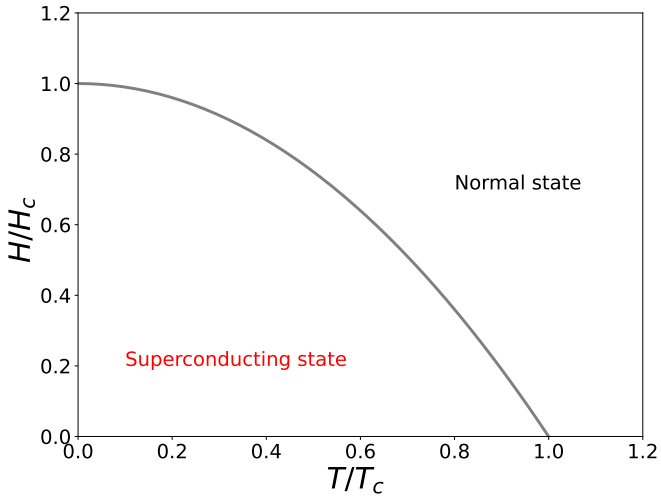

Figure 2.3: ***Temperature dependence of the critical field in a type I superconductor.*** *The critical field $H_c(T)$ destroys superconductivity by breaking cooper pairs in the metal.*

ducting electrons in contrast to normal conductors, where an electric field results in a steady velocity (Ohm's law).

The second London equation can be derived from the first by applying the curl operator to both sides of the first equation and utilizing Maxwell's equation $\nabla \times \boldsymbol{E} = -\frac{\partial \boldsymbol{B}}{\partial t}$. When combined with Maxwell's equation $\nabla \times \boldsymbol{B} = \mu_0 \boldsymbol{J}$, the second London equation (2.4) leads to:

$$\nabla^2 \boldsymbol{B} = \frac{\boldsymbol{B}}{\lambda^2}. \tag{2.9}$$

This indicates that a magnetic field is exponentially screened from the interior of a superconductor with a penetration depth λ, illustrating the Meissner effect. The temperature dependence of λ can be approximately described by [14]:

$$\lambda(T) \approx \lambda(0)[1 - (T/T_c)^4]^{-1/2}. \tag{2.10}$$

2.1.2 Ginzburg-Landau Theory

The Ginzburg-Landau theory, developed in 1950 [25], is a phenomenological approach to understanding superconductivity. The theory describes superconductors using a complex pseudo-wavefunction ψ as an order parameter within Landau's general theory of second-order phase transitions. This order parameter can be written as

$$\psi(\boldsymbol{r}, t) = |\psi| e^{i\phi}. \tag{2.11}$$

In the Ginzburg-Landau theory, $|\psi|^2 = n_s$ denotes the Cooper pair density and ϕ represents the phase. This order parameter takes the value of zero in the normal metal state and a non-zero value in the SC state. The free-energy density f can be expanded in a Taylor series in powers of $|\psi|^2$ if ψ is small and varies slowly in space (valid near T_c):

$$f = f_n + \alpha|\psi|^2 + \frac{\beta}{2}|\psi|^4 + \frac{1}{2m^*}\left|\left(\frac{\hbar}{i}\boldsymbol{\nabla} - e^*\boldsymbol{A}\right)\psi\right|^2 + \frac{1}{2\mu_0}\left|\nabla \times \boldsymbol{A}\right|^2, \tag{2.12}$$

where m^* and e^* are the effective mass and electric charge of the SC charge carriers (Cooper pairs), $\hbar$ the reduced Planck's constant, $\boldsymbol{A}$ is the vector potential, and f_n is the free energy density in the normal state. α and β are expansion parameters.

Equating the functional derivative $\delta f/\delta\psi^*$ to zero we get the first Ginzburg-Landau equation,

$$\frac{1}{2m^*}\left(\frac{\hbar}{i}\boldsymbol{\nabla} - e^*\boldsymbol{A}\right)\psi + \beta|\psi|^2\psi = -\alpha(T)\psi. \tag{2.13}$$

Similarly, minimizing the free energy with respect to the distribution of magnetic fields implies $\delta f/\delta A(\boldsymbol{r}) = 0$, leading to the second Ginzburg-Landau equation,

$$\boldsymbol{J}_s = \frac{e^*\hbar}{i2m^*}\left(\psi^*\boldsymbol{\nabla}\psi - \psi\boldsymbol{\nabla}\psi^*\right) - \frac{e^{*2}}{m^*}\psi\psi^*\boldsymbol{A}. \tag{2.14}$$

In terms of the ψ magnitude and phase, assuming $|\psi|$ is uniform:

$$\boldsymbol{J}_s = \frac{e^*}{m}|\psi|^2\left(\hbar\boldsymbol{\nabla}\phi - e^*\boldsymbol{A}\right). \tag{2.15}$$

2.1.3 *Josephson Relations*

The Josephson relations describe the behavior of supercurrents through a Josephson junction (tunneling of Cooper pairs), which consists of two superconductors separated by a thin insulating barrier, see Fig. 2.4. These relations, predicted by Josephson in 1962 [26], form the foundation of many superconducting quantum devices. The first and second Josephson relation are:

$$I_s = I_c \sin(\phi), \tag{2.16}$$

and

$$\frac{\partial \phi}{\partial t} = -\frac{2e}{\hbar} V. \tag{2.17}$$

I_c is the critical current, the maximum supercurrent that can pass through the junction without applying a voltage, ϕ is the phase difference across the junction and V is a constant voltage applied across the junction. When no voltage is applied across the junction, a constant supercurrent flows through the insulating barrier (first relation). In contrast, when a constant voltage is applied across the junction, the phase difference ϕ varies linearly with time (second relation).

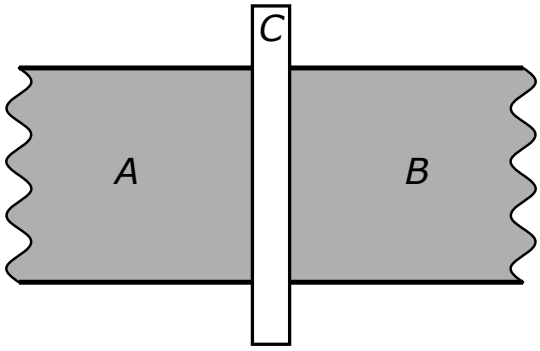

Figure 2.4: ***A Josephson Junction.***
A and B represent superconductors, and C is an insulating barrier (weak link) between them. Figure taken from Ref. [27].

2.1.4 Quantization of Magnetic Flux

Flux quantization in SC rings arises from the quantum mechanical nature of the superconducting state, this property of SC circuits is exploited by SC qubits as will be seen in section 2.2. To prove this, consider a SC ring enclosing a total magnetic flux Φ as in Fig. 2.5 and let the wavefunction of the SC condensate be $\psi = |\psi|e^{i\phi}$. If the SC ring is thicker than the penetration depth λ, the supercurrent density $\boldsymbol{J}_s$ must be zero inside the ring from the Meissner effect. From Eq. (2.15), inside the ring:

$$\hbar\nabla\phi = e^*\mathbf{A}. \tag{2.18}$$

Taking the integral around the closed loop $\mathcal{C}$ gives

$$e^* \oint_{\mathcal{C}} \mathbf{A}\cdot d\mathbf{l} = \hbar \oint_{\mathcal{C}} \nabla\phi \cdot d\mathbf{l} = \hbar(\phi_2 - \phi_1), \tag{2.19}$$

$\phi_2 - \phi_1$ is the phase difference across the loop $\mathcal{C}$. Since ψ must be a single-valued function:

$$\phi_2 - \phi_1 = 2\pi k, \tag{2.20}$$

where k is an integer. Applying Stokes' theorem to Eq. (2.19) gives

$$\oint_{\mathcal{C}} \mathbf{A}\cdot d\mathbf{l} = \int_{\mathcal{S}} (\nabla\times\mathbf{A})\cdot d\mathbf{a} = \int_{\mathcal{S}} \mathbf{B}\cdot d\mathbf{a} = \Phi. \tag{2.21}$$

where da is the area element on a surface $\mathcal{S}$ bounded by $\mathcal{C}$, Φ is the magnetic flux through $\mathcal{S}$. Using the condition of Eq. (2.20) and $e^* = 2e$, we get

$$\Phi = \frac{h}{2e}k = k\Phi_0, \tag{2.22}$$

where $\Phi_0 = \frac{h}{2e}$ is the flux quantum. Therefore, the flux through the SC ring is quantized in integer multiples of Φ_0 [16].

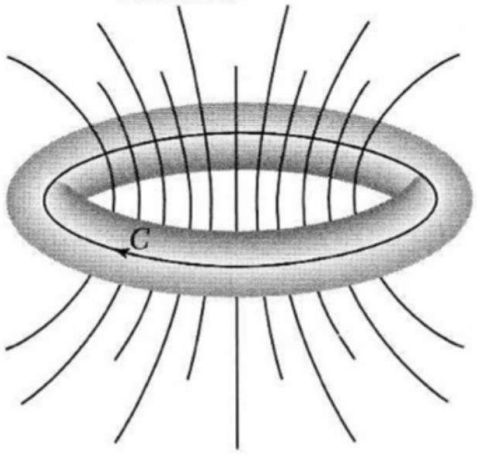

Figure 2.5: ***Superconducting ring.***
Path of integration C through the center of the material in a SC ring. Figure taken with permission from Ref. [16].

2.2 Superconducting Qubits

As explained in the previous section, SC circuits can exhibit quantum mechanical properties on a macroscopic scale, as opposed to other qubit technologies [28–31]. The quantum state in SC circuits is associated with discrete energy levels, which are determined by the circuit's design. The addition of Josephson junctions introduces a non-linearity, allowing these energy levels to be tunable and non-harmonic. Furthermore, the circuit can transition between these energy levels by applying microwave pulses at specific frequencies, effectively changing its quantum state. These properties make superconducting circuits promising candidates for implementation as qubits in quantum computers. In this section, we start by introducing the LC resonator as an example of a simple quantum circuit, which is also the base for some of the most common types of SC qubits. We then extend the discussion to some of these qubits, like transmons and radio-frequency superconducting quantum interference devices (rf-SQUIDs).

2.2.1 LC Resonator

The quantum LC resonator is one of the simplest lumped-element SC circuits that is also the base for the main SC qubits considered here. Consider a classical LC resonator characterized by its inductance L and capacitance C, see Fig. 2.6b. The total energy of this circuit is given by the sum of its charging and inductive energies:

$$\mathcal{H} = \frac{Q^2}{2C} + \frac{1}{2L}\Phi^2 = \frac{Q^2}{2C} + \frac{C\omega_r^2}{2}\Phi^2, \tag{2.23}$$

where Q is the charge on the capacitor, Φ is the magnetic flux threading the inductor and $\omega_r = 1/\sqrt{LC}$. This expression makes clear the analogy between an LC resonator and a mechanical harmonic oscillator with a coordinate Φ, conjugate momentum Q and a mass C. In order to describe this system quantum-mechanically, we promote the charge and flux coordinates to quantum operators that satisfy a commutation relation:

$$[\hat{\Phi}, \hat{Q}] = \hat{\Phi}\hat{Q} - \hat{Q}\hat{\Phi} = i\hbar, \tag{2.24}$$

where the operators are indicated by hats. From this point forward, however, we omit the hats writing $\hat{\Phi} = \Phi, \hat{Q} = Q$. Defining the reduced flux $\phi \equiv 2\pi\Phi/\Phi_0$ and the reduced charge $n = Q/2e$, we can write down the circuit Hamiltonian as

$$\mathcal{H} = 4E_C n^2 + \frac{1}{2}E_L\phi^2, \tag{2.25}$$

where $E_C = e^2/(2C)$ and $E_L = (\Phi_0/2\pi)^2/L$. From Eq. (2.24)

$$[\phi, n] = i, \tag{2.26}$$

therefore, these two operators form a canonical conjugate pair.

Following the harmonic oscillator analogy, we define the operators ϕ, n in terms of creation

and annihilation operators $a^\dagger, a$:

$$\phi = \phi_{zpf}(a^\dagger + a), \tag{2.27a}$$

$$n = in_{zpf}(a^\dagger - a). \tag{2.27b}$$

$n_{zpf} = [E_L/(32E_C)]^{1/4}$ and $\phi_{zpf} = [2E_C/E_L]^{1/4}$ are the *zero point fluctuations* of the charge and phase variables. Under this transformation, the LC resonator Hamiltonian takes the form

$$\mathcal{H} = \hbar\omega_r \left(\hat{a}^\dagger \hat{a} + \frac{1}{2}\right), \tag{2.28}$$

identical to the Hamiltonian of a quantum harmonic oscillator (QHO), see Fig. 2.6a. The ladder operators follow the relations: $[\hat{a}, \hat{a}^\dagger] = 1$, $\hat{a}|k\rangle = \sqrt{k}|k-1\rangle$, and $\hat{a}^\dagger|k\rangle = \sqrt{k+1}|k+1\rangle$ for the eigenstates $|k\rangle$ of the QHO. Note that in order to operate an LC resonator in a regime where quantum effects are important, the system must be cooled to very low temperatures where the thermal energy k_BT, with k_B the Boltzmann constant, is much smaller than the energy difference between quantum levels, allowing the system to occupy its ground state or low energy excited states. Aditionally, the LC resonator should have a high quality factor (Q-factor), which means low dissipation or loss. The resonator can thus remains coherent for a long time, making quantum effects relevant in this regime.

2.2.2 Transmon

The uniform energy spacing in a QHO makes it challenging to access and manipulate individual eigenstates, which is crucial for quantum computation. To address this, we introduce a non-linearity into the circuit in the form of a Josephson junction. This non-linearity disrupts the harmonic spacing of the energy levels, allowing the transition frequencies between energy states to be sufficiently different. The potential energy of the Josephson junction can be calculated using both Josephson equations, Eqs. (2.16), (2.17):

$$U_L = \int_{-\infty}^{t} V(t')I(t')dt' = \frac{\hbar I_c}{2e}\int_{-\infty}^{t} \frac{d\phi}{dt'} sin(\phi)dt' = -E_J cos(\phi), \tag{2.29}$$

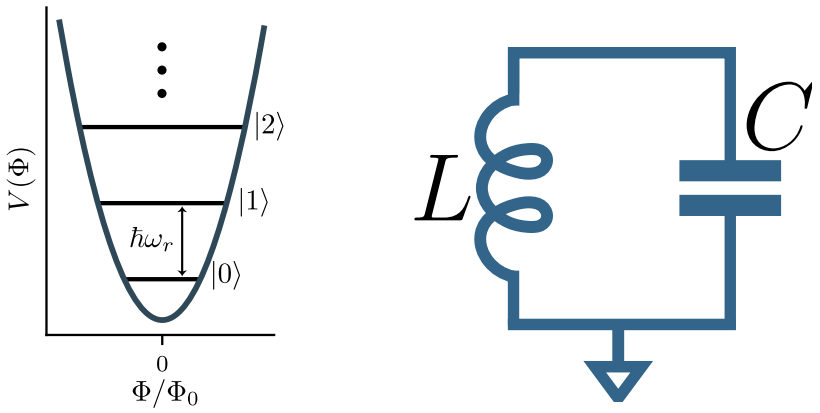

(a) *LC potential.* **(b)** *LC circuit.*

Figure 2.6: ***LC resonator.***
(a) *Harmonic potential of LC resonator vs flux, the energy levels are equivalent to a QHO.* **(b)** *Lumped-element LC resonator [32].*

where $E_J = I_c\hbar/(2e)$ is the Josephson energy. Replacing the lumped-element inductor in the LC resonator by a Josephson junction acting as a non-linear inductor (see Fig. 2.7b), the Hamiltonian is modified to

$$\mathcal{H} = 4E_C n^2 - E_J \cos(\phi), \tag{2.30}$$

where $E_C = e^2/(2C_\Sigma)$, $C_\Sigma = C_s + C_J$ is the total capacitance, including both shunt capacitance C_s and the self-capacitance of the junction C_J. The spectrum of Eq. (2.30) will be determined by the ratio E_J/E_C. When $E_J \ll E_C$ (charge qubits), the system is highly sensitive to charge noise, and the energy eigenstates are approximately the charge operator n eigenstates with slight perturbations due to the Josephson junction. When $E_J \gg E_C$, the potential energy landscape is dominated by the Josephson junction, leading to well-defined phase states (ϕ is a good quantum number). The transmon corresponds to this regime [33]. When $E_J \approx E_C$, the system exhibits characteristics of both charge and phase regimes, leading to complex energy level structures. This regime can be hard to handle as it does not fully leverage the advantages of either extreme. For the rest of this section, we focus on the transmon ($E_J \gg E_C$) regime. Since $\Delta\phi \ll 1$ in this regime, we can expand Eq. (2.30) into a power series in ϕ,

$$\mathcal{H} = 4E_C n^2 + \frac{1}{2}E_J\phi^2 - \frac{1}{4!}E_J\phi^4 + O(\phi^6). \tag{2.31}$$

Using Eqs. (2.27) in Eq. (2.31) leads to the Hamiltonian [17]

$$\mathcal{H} = \sqrt{8E_C E_J}a^\dagger a - \frac{E_C}{12}(a^\dagger + a)^4 \approx \hbar\omega_q a^\dagger a - \frac{E_C}{2}a^\dagger a^\dagger a a, \tag{2.32}$$

with $\omega_q = \sqrt{8E_C E_J} - E_C$. Note that in the second equality of Eq. (2.32), we dropped non-resonant terms (terms with unequal numbers of $a, a^\dagger$). From this expression we can conclude that the transmon resembles a weakly anharmonic oscillator (AHO), see Fig. 2.7a, and thus allows for the identification of an addressable quantum two-level system (TLS).

2.2.3 Flux-Tunable Transmon

Qubit frequency tunability is essential to circumvent the frequency crowding problem faced by SC circuits with more than 100 qubits [34, 35]. A widely used technique to achieve frequency

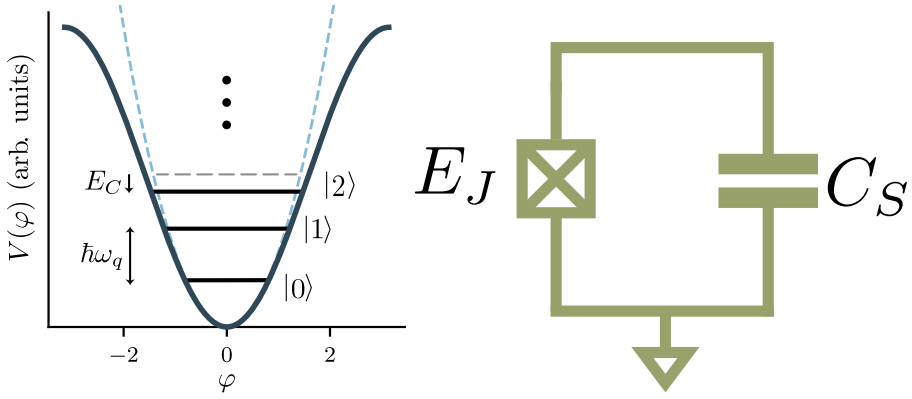

(a) *Transmon potential.* **(b)** *Transmon circuit.*

Figure 2.7: ***Transmon.***
(a) *Potential well of the transmon qubit vs reduced flux compared to the LC potential in dashed lines. The transmon potential is anharmonic with* $\omega_{01} \neq \omega_{12}$. **(b)** *Lumped-element transmon qubit, the linear inductance in the LC resonator is replaced by a Josephson junction [32].*

tunability consists in replacing the single Josephson junction in a transmon with a loop interrupted by two identical junctions, forming a DC superconducting quantum interference device (dc-SQUID), see Fig. 2.8. This also introduces sensitivity to random flux fluctuations, known as flux noise as will be discussed in chapter 3. Defining $\phi_{1(2)}$ as the phase across junction 1 (2), Φ_{ext} an external flux, $\phi_{ext} = 2\pi\Phi_{ext}/\Phi_0$ the reduced external flux and noting that flux quantization requires $\phi_1 - \phi_2 + \phi_{ext} = 2k\pi$, the effective Hamiltonian of the flux-tunable transmon is

$$\begin{aligned}\mathcal{H} &= 4E_C n^2 - E_J\cos(\phi_1) - E_J\cos(\phi_2) \\ &= 4E_C n^2 - E_J\cos(\phi + \phi_{ext}/2) - E_J\cos(\phi - \phi_{ext}/2) \\ &= 4E_C n^2 - 2E_J\cos(\phi_{ext}/2)\cos(\phi) \\ &\equiv 4E_C n^2 - E'_J(\phi_{ext})\cos(\phi),\end{aligned} \tag{2.33}$$

where $E'_J(\phi_{ext}) = 2E_J\cos(\phi_{ext}/2)$, $\phi = (\phi_1 + \phi_2)/2$. Eq. (2.33) is analogous to Eq. (2.30), with E_J replaced by $2E_J\cos(\phi_{ext}/2)$. This is effectively a transmon qubit with an E_J that can be tuned with Φ_{ext}.

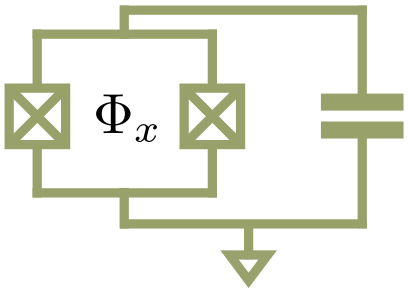

Figure 2.8: ***Flux-tunable transmon.***
The single Josephson junction in the transmon is replaced by a symmetric loop with two junctions. In this circuit, the Josephson energy E_J is flux-tunable by the external flux Φ_x [32].

2.2.4 rf-SQUID as Flux Qubit

The rf-SQUID is a SC loop interrupted by a single Josephson junction (Figure 2.9). The energy of the SQUID can be split into the Josephson energy, magnetostatic energy and electrostatic energy

(an LC resonator with a junction). If there is an external flux Φ_{ext} threading the loop, the total flux is $\Phi = \Phi_{\text{ext}} + LI$. The Hamiltonian is thus

$$\mathcal{H} = -E_J \cos(\phi) + \frac{1}{2}E_L(\phi - \phi_{\text{ext}})^2 + 4E_C n^2. \tag{2.34}$$

Using $Q = i\hbar\frac{\partial}{\partial\Phi}$ or $n = i\frac{\partial}{\partial\phi}$ since Q and Φ are a conjugate pair, we can write the Hamiltonian as

$$\mathcal{H} = -E_J \cos(\phi) + \frac{1}{2}E_L(\phi - \phi_{\text{ext}})^2 - 4E_C\frac{\partial^2}{\partial\phi^2} = V(\phi) - \frac{\hbar^2}{2m}\frac{d^2}{d\phi^2}. \tag{2.35}$$

This is the Hamiltonian of a particle of mass $m = \frac{\hbar^2}{8E_C}$ under a potential $V(\phi)$. When $\Phi_{\text{ext}} = \frac{\Phi_0}{2}$,

$$V(\phi) = E_J \cos(\phi - \pi) + \frac{E_L}{2}(\phi - \pi)^2. \tag{2.36}$$

For $x \equiv (\phi - \pi) << 1$, we can expand this as,

$$V(x) = E_J\left[1 - \frac{x^2}{2} + \frac{x^4}{4!} + O(x^6)\right] + \frac{E_L}{2}x^2, \tag{2.37}$$

$$= E_J - \frac{1}{2}(E_J - E_L)x^2 + \frac{E_J}{4!}x^4 + O(x^6). \tag{2.38}$$

Thus, as E_J increases, the coefficient of x^2 changes sign, and the rf-SQUID potential goes from a single well to a double well potential near $\phi \approx \pi$ ($\Phi = \frac{\Phi_0}{2}$), see Fig. 2.10. E_J can be tuned by replacing the Josephson junction with a tunable DC SQUID as described in subsection 2.2.3. The state in each well can be thought of as the current in the SQUID circulating clockwise (↻) or counter-clockwise (↺). The energy eigenstates of this system are:

$$|0\rangle = \frac{1}{\sqrt{2}}(|\circlearrowleft\rangle + |\circlearrowright\rangle), \tag{2.39}$$

$$|1\rangle = \frac{1}{\sqrt{2}}(|\circlearrowleft\rangle - |\circlearrowright\rangle). \tag{2.40}$$

Therefore, through the application of an external flux, the SQUID behaves effectively as a qubit at low temperatures [36, 37].

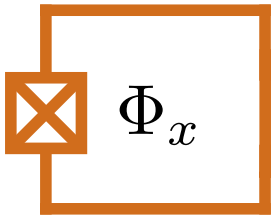

Figure 2.9: ***rf-SQUID in an external flux.***
The rf-SQUID consist of a SC loop interrupted by one Josephson junction, Φ_x is an external flux.

2.2.5 Fluxonium

The fluxonium is an extension of rf-SQUIDs achieved by the inclusion of a superinductor, an array of Josephson junctions. This superinductor provides high inductance (much larger than the geometric inductance of SC wires) without introducing significant losses, enhancing the qubit's coherence time [39, 40]. In this case, the Josephson energy term becomes $-E_J\cos(\phi+\phi_{ext})-NE'_J\cos(\phi/N)$, the first term is due to a single Josephson junction with energy E_J and the second term is due to an array of N junctions with energy $E'_J > E_J$ forming a superinductor, see Fig. 2.11. Note that here ϕ/N is the phase across each Josephson junction composing the superinductor. For large N, the argument in the cosine term ϕ/N becomes small and a second order expansion provides a good approximation. The fluxonium Hamiltonian is thus

$$H = 4E_C n^2 - \frac{E'_J}{N}\phi^2 - E_J\cos(\phi+\phi_{ext}), \tag{2.41}$$

where E'_J/N is the inductive energy of the effective inductance contributed by the junction array. We can thus treat the potential energy as a quadratic term modulated by a sinusoidal term as we did in the rf-SQUID case.

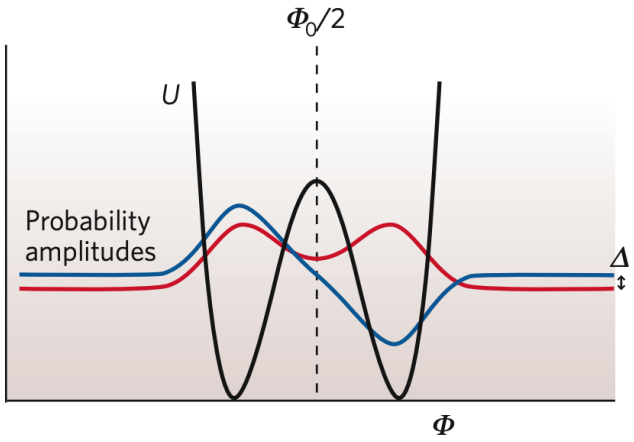

Figure 2.10: ***The rf-SQUID double-well potential.***
The double-well potential (black) versus total flux Φ contained in a flux qubit. The two wells are symmetrical when the externally applied magnetic flux is $\Phi_0/2$. The coloured curves are the eigenfunctions (probability amplitudes) for the ground state (symmetrical, red) and first excited state (antisymmetrical, blue) [38].

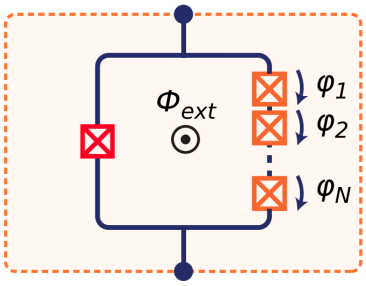

Figure 2.11: ***Fluxonium qubit.***
A small junction is inductively shunted with a large array of N junctions forming a superinductor [41].

CHAPTER 3

Noise in Superconducting Qubits

The performance of SC qubits is significantly limited by decoherence mechanisms, random fluctuations that couple to the qubits limiting their relaxation and coherence times. Understanding these processes is crucial for the advancement of quantum computing. Section 3.1 provides an introduction to noise and decoherence in SC qubits based on References [4, 18, 42]. Section 3.2 discusses the main sources of decoherence in SC qubits and provides a survey on some of the state-of-the-art experimental measurements of flux noise, as that is the main issue addressed in most of this dissertation.

3.1 Noise and Decoherence

3.1.1 Bloch-Sphere Representation

Before starting our discussion on relaxation and dephasing, it is useful to introduce the Bloch-sphere representation as a visualization tool for a quantum state. The Bloch sphere is a unit sphere used to represent the quantum state of a TLS or qubit. The state $|\psi\rangle = \alpha\,|0\rangle + \beta\,|1\rangle$ is depicted as a Bloch vector on the sphere with $|\alpha|^2 + |\beta|^2 = 1$ for pure quantum states. The Bloch vector is defined by $\boldsymbol{v} = \langle\psi|\boldsymbol{\sigma}|\psi\rangle$, where $\boldsymbol{\sigma} = (\sigma_x, \sigma_y, \sigma_z)$ is the vector of Pauli matrices. The north pole of the Bloch sphere corresponds to the state $|0\rangle$, and the south pole corresponds to $|1\rangle$, see Fig. 3.1. The longitudinal axis (z-axis), represents the qubit quantization axis for the states $|0\rangle$ and $|1\rangle$. We can represent a general quantum state in the Bloch sphere in terms of a polar angle $0 \leq \theta \leq \pi$ and an azimuthal angle $0 \leq \phi < 2\pi$:

$$|\psi\rangle = \alpha\,|0\rangle + \beta\,|1\rangle = \cos\frac{\theta}{2}\,|0\rangle + e^{i\phi}\sin\frac{\theta}{2}\,|1\rangle\,. \tag{3.1}$$

This state corresponds to Bloch vector $\boldsymbol{v} = (\sin\theta\cos\phi, \sin\theta\sin\phi, \cos\theta)$. In a rotating frame where the x and y axes rotate around the z-axis at the qubit frequency $\omega_q = \frac{E_1 - E_0}{\hbar}$, the Bloch vector representing the state ψ will remain stationary in time. In the following, the references to the Bloch-sphere representation assume a rotating frame such as this.

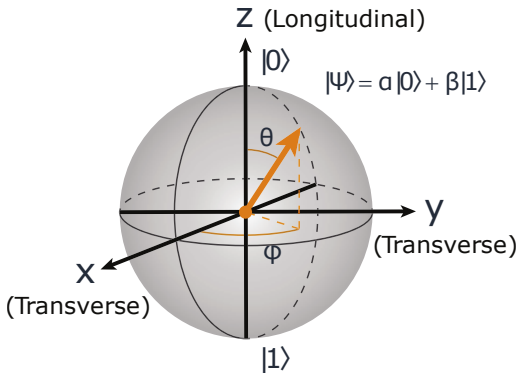

Figure 3.1: ***Bloch Sphere.***
Bloch-sphere representation of a general quantum state $|\psi\rangle = \alpha\,|0\rangle + \beta\,|1\rangle$ *[41].*

3.1.2 Relaxation

Relaxation, also known as energy relaxation or longitudinal relaxation, refers to the process by which a qubit in an excited state $|1\rangle$ loses energy to its environment and transitions to the ground state $|0\rangle$. This process is characterized by the time T_1, which represents the $1/e$ decay for the qubit polarization (along z in the Bloch-sphere representation).

The standard method for measuring T_1 consists in the following steps:

1. Initialize the qubit in the ground state $|0\rangle$.

2. Apply a π-pulse (this effectively rotates the qubit state by an angle π around the x axis in the Bloch-sphere representation) to the qubit to excite it to the state $|1\rangle$.

3. Allow the qubit to evolve freely for a variable delay time τ.

4. Measure the probability $P_1(\tau)$ of finding the qubit in the excited state $|1\rangle$ as a function of τ (to estimate $P_1(\tau)$, many repetitions of this measurement are needed).

The excited state population decays exponentially:

$$P_1(\tau) = P_1(0)e^{-\tau/T_1}. \tag{3.2}$$

By fitting the decay curve to this exponential function, T_1 can be extracted. Fig. 3.2a shows a T_1 measurement example.

3.1.3 Dephasing

Dephasing, or phase relaxation, refers to the loss of phase coherence between the components of a quantum superposition state in a qubit. There are 2 contributions to dephasing:

- **Pure Dephasing (T_ϕ)**: Phase fluctuations caused by environmental noise, with no energy exchange. Intuitively, the impact of pure dephasing can be seen as fluctuations in the qubit frequency that will provoke a rotation around z for a state ψ in the Bloch-sphere representation.

- **Relaxation-Induced Dephasing**: Contribution to dephasing due to energy relaxation.

We define two different timescales that characterize dephasing: T_2^* and T_2. T_2^* characterizes the timescale at which a qubit's superposition state loses coherence due to both intrinsic dephasing and external inhomogeneities (time-dependent fluctuations) that can be different in each measurement repetition. It is related to relaxation and pure dephasing time by $1/T_2^* = 1/(2T_1)+1/T_\phi$ and is typically measured using Ramsey interferometry by performing the following steps:

1. The qubit is initialized in the ground state $|0\rangle$.

2. A $\pi/2$ pulse is applied changing the state to a superposition state $\frac{1}{\sqrt{2}}(|0\rangle + |1\rangle)$, effectively rotating the state vector to the equator.

3. The qubit evolves freely for a time τ. During this period, the state vector in the Bloch-sphere precesses around the z axis at a frequency $\omega = \langle\omega_q\rangle + \Delta\omega(t)$ where $\langle\omega_q\rangle$ is the average qubit frequency over all repetitions, and $\Delta\omega(t)$ is the frequency shift at the specific repetition instant.

4. Another $\pi/2$ pulse is applied. This pulse converts the phase information into a population difference.

5. The probability $P_1(\tau)$ of finding the qubit in the $|1\rangle$ state is measured. The probability oscillates with τ due to the interference pattern, and the envelope of these oscillations decays due to dephasing.

The envelope of these oscillations decays exponentially with T_2^*:

$$P_1(\tau) \propto e^{-\tau/T_2^*}. \tag{3.3}$$

By fitting the decay of the oscillation envelope, T_2^* can be extracted. Fig. 3.2b shows a T_2^* measurement example.

On the other hand, T_2 is defined as the decay time measured in a Hahn echo experiment. This measurement is much less susceptible to low frequency fluctuations over the time length of the experiment (the time it takes for all repetitions), and is performed by the steps:

1. The qubit is initialized in the ground state $|0\rangle$.

2. A $\pi/2$ pulse is applied to change the state to a superposition state $\frac{1}{\sqrt{2}}(|0\rangle + |1\rangle)$, effectively rotating the state vector to the equator.

3. The qubit evolves freely for a time $\tau/2$. The state vector in the Bloch-sphere precesses around the z axis, accumulating a phase.

4. A π pulse is applied, this pulse inverts the state vector through the xz plane, reversing the phase accumulation.

5. The qubit evolves for another time $\tau/2$. The state vector precesses again around the z axis, accumulating phase in the opposite direction. The state vector returns to the same

position it had before the first free evolution, refocusing some of the dephasing due to time-dependent fluctuations of ω_q on frequency scales less than $\approx 1/\tau$.

6. Another $\pi/2$ pulse is applied, the state vector is projected back toward the poles.

7. The probability $P_1(\tau)$ of finding the qubit in the $|1\rangle$ state is measured.

The decay of the echo amplitude as a function of τ is:

$$P_1(\tau) \propto e^{-\tau/T_2}. \tag{3.4}$$

By fitting the decay curve, T_2 can be extracted. Fig. 3.2c shows a T_2 measurement example. The timescale that characterizes dephasing is thus highly dependent on the pulse sequence used to measure it.

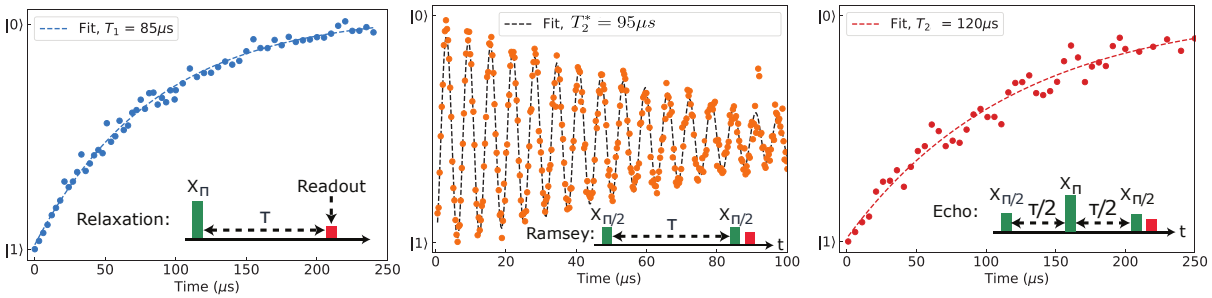

(a) *T_1 measurement.* **(b)** *Ramsey interferometry.* **(c)** *Hahn echo experiment.*

Figure 3.2: ***Longitudinal (T_1) and transverse (T_2) relaxation times measurements of a transmon qubit.***
(a) *Longitudinal relaxation T_1 measurement [41].* **(b)** *T_2^* measurement via Ramsey interferometry [41].* **(c)** *T_2 measurement via a Hahn echo experiment [41].*

3.1.4 Noise Power Spectral Density

The Power Spectral Density (PSD) $\tilde{S}_\eta(\omega)$ of a noise source η is defined as

$$\tilde{S}_\eta(\omega) = \int_{-\infty}^{\infty} d\tau \langle \eta(\tau)\eta(0)\rangle e^{i\omega\tau}, \tag{3.5}$$

where η is an operator defined in some space. The PSD is thus the Fourier transform of the autocorrelation function $S_\eta(\tau) = \langle \eta(\tau)\eta(0)\rangle$ of the noise source η. Similarly, S can be calculated from $\tilde{S}$ taking the inverse Fourier transform:

$$S_\eta(\tau) = \frac{1}{2\pi}\int_{-\infty}^{\infty} d\omega \tilde{S}_\eta(\omega) e^{-i\omega\tau}. \tag{3.6}$$

Note that the PSD can also be written in terms of the system's eigenstates:

$$\tilde{S}_\eta(\omega) = \int_{-\infty}^{\infty} d\tau e^{i\omega\tau} \sum_{\alpha,\gamma} \rho_{\alpha\alpha}\langle\alpha|\eta(\tau)|\gamma\rangle\langle\gamma|\eta(0)|\alpha\rangle, \tag{3.7}$$

where we have assumed that the density matrix ρ is diagonal in the energy eigenbasis and time-independent. This yields the spectral-decomposition expression for the PSD,

$$\begin{aligned}\tilde{S}_\eta(\omega) &= \int_{-\infty}^{\infty} d\tau e^{i\omega\tau} \sum_{\alpha,\gamma} \rho_{\alpha\alpha} e^{i(\epsilon_\alpha - \epsilon_\gamma)\tau/\hbar} \left|\langle\alpha|\eta|\gamma\rangle\right|^2 \\ &= 2\pi\hbar \sum_{\alpha,\gamma} \rho_{\alpha\alpha} \left|\langle\alpha|\eta|\gamma\rangle\right|^2 \delta(\epsilon_\gamma - \epsilon_\alpha - \hbar\omega).\end{aligned} \tag{3.8}$$

3.1.5 Bloch–Wangsness–Redfield Master Equation

The Bloch–Wangsness–Redfield (BWR) master equation is a generalization of the Bloch equations that includes interactions with an environment, capturing the effects of noise in a more rigorous framework compared to the phenomenological approach of Bloch equations. Consider an effective Hamiltonian

$$\mathcal{H} = \frac{\hbar\omega_q}{2}\sigma_z + \frac{1}{2}\sum_{k=x,y,z} \eta_k(t)\sigma_k. \tag{3.9}$$

The first term corresponds to the qubit Hamiltonian, and the second term models the coupling between the qubit and environmental noise sources η_k where the σ_k are the Pauli operators for $k = x, y, z$. In the Markovian and weak-coupling limit, the average values of the σ_k satisfy the BWR master equation [42, 43]:

$$\frac{d}{dt}\langle\boldsymbol{\sigma}\rangle = \frac{i\omega_q}{2}\langle[\sigma_z,\boldsymbol{\sigma}]\rangle - \frac{1}{T_1}\langle\sigma_z\rangle\hat{\boldsymbol{z}} - \frac{1}{T_{2x}}\langle\sigma_x\rangle\hat{\boldsymbol{x}} - \frac{1}{T_{2y}}\langle\sigma_y\rangle\hat{\boldsymbol{y}}, \tag{3.10}$$

with

$$\frac{1}{T_1} = \frac{1}{4\hbar^2}\sum_{k=x,y}\left[\tilde{S}_{\eta_k}(\omega_q) + \tilde{S}_{\eta_k}(-\omega_q)\right], \tag{3.11a}$$

$$\frac{1}{T_{2x}} = \frac{1}{4\hbar^2}\left[\tilde{S}_{\eta_y}(\omega_q) + \tilde{S}_{\eta_y}(-\omega_q)\right] + \frac{1}{2\hbar^2}\tilde{S}_{\eta_z}(0), \tag{3.11b}$$

$$\frac{1}{T_{2y}} = \frac{1}{4\hbar^2}\left[\tilde{S}_{\eta_x}(\omega_q) + \tilde{S}_{\eta_x}(-\omega_q)\right] + \frac{1}{2\hbar^2}\tilde{S}_{\eta_z}(0). \tag{3.11c}$$

Eqs. (3.11) assume $\langle\eta_k(t)\eta_{k'}(0)\rangle = 0$ for $k \neq k'$. From Eq. (3.10), it can be shown that the amplitude $|\langle\sigma_x + i\sigma_y\rangle|$ decays with a rate

$$\frac{1}{T_2^*} = \frac{1}{2}\left(\frac{1}{T_{2x}} + \frac{1}{T_{2y}}\right) = \frac{1}{2T_1} + \frac{1}{T_\phi} \tag{3.12}$$

with $1/T_\phi = \frac{1}{2\hbar^2}\tilde{S}_{\eta_z}(0)$.

These equations are a generalization of Fermi's golden rule and provide a clear connection between the PSD of a noise source $\tilde{S}_\eta$ and relaxation/dephasing times. Note that this relationship, however, assumes Eq. (3.10) is valid, and thus, all σ_k can be described by an exponential decay time dependence. This is not the case in general. In the presence of $1/f$ noise, for example, the expressions are more complicated [42, 44]. For these reasons, it is convenient to focus on the quantity $\tilde{S}_\eta$, as it provides a way to characterize noise that depends only on the noise source η and is independent of the coupling between the qubit and the environment or the pulse sequence used in dephasing time measurements.

3.2 Sources of Decoherence in Superconducting Qubits

3.2.1 Flux Noise

Although extensive research has been conducted, the fundamental cause of flux noise remains elusive, making it challenging to reduce its effects. It is widely believed, however, that flux noise

originates from the dynamics of magnetic impurities near the SC wires [5–7, 45–48]. This conclusion is supported by experiments showing noise amplitude following the Curie susceptibility law ($\tilde{\chi}(\omega = 0) \propto 1/T$, where T is temperature) [7]. There is no clear consensus on the magnetic order of the spins causing noise. While some authors claimed proximity to a spin glass phase [7, 8], recent experiments observed a Curie-Weiss susceptibility $\tilde{\chi}(\omega = 0) \propto 1/(T - T_{\rm CW})$ which rules out the spin glass scenario. Quintana et al. [48] measured $T_{\rm CW} \approx -10$ mK < 0 indicating proximity to an *antiferromagnetic* (AFM) phase, while Lanting et al. [49] measured $T_{CW} \approx +5$ mK > 0 indicating proximity to a *ferromagnetic* (FM) phase.

The general consensus regarding the identity of these spin impurities suggests two main types: electron spins (such as dangling bonds and interface states) and nuclear spins. A dangling bond is a paramagnetic defect typically linked to an oxygen vacancy at the metal/metal-oxide interface in superconducting devices. When there is a vacancy, not all of an atom's valence electrons will be paired to form covalent bonds with other atoms; these unpaired electrons possess a magnetic moment [6].

Localized electron spins at the metal-insulator boundary can also contribute to noise. Under ideal conditions with smooth interfaces, electrons travel through the metal as Bloch waves and decay in the insulator. However, an uneven surface causes fluctuations in the electronic potential at the boundary. As a result, a significant fraction of metal-induced gap states with single occupancy become strongly localized near the interface, producing the observed paramagnetic spin [50]. Finally, nuclear spins are always present, even in perfect lattices. Although their density is much larger than the unpaired electron spin density, their magnetic moment is about three orders of magnitude smaller. Explicit calculations of flux noise due to nuclear spins suggest they may account for a small fraction (less than 5%) of the observed flux noise [51].

Experimental measurement of the flux noise spectrum in different materials and qubit architectures suggest the following empirical law,

$$\tilde{S}_\Phi(f) = \frac{A_\Phi^2}{f^\alpha}. \tag{3.13}$$

Most measurements of flux noise have been done in devices made of two SC materials: Al and Nb.

3.2.2 *Flux Noise in Aluminum Devices*

For Al, Quintana et al. reported an approximately $1/f$ frequency dependence for the symmetric component of flux noise $\tilde{S}^{+}_{\Phi}(f) \equiv \tilde{S}_{\Phi}(f) + \tilde{S}_{\Phi}(-f)$ over several decades of frequency and an Ohmic or super-Ohmic dependence above the classical-quantum crossover point $f = k_B T/h$ [48], these results are shown in Fig. 3.3a. The source of the observed $1/f$ low-frequency noise and the shift to high-frequency Ohmic noise, remains unidentified. They also observed a $1/(T+T_0)$ temperature dependence below 100 mK for the antisymmetric component of flux noise $\tilde{S}^{-}_{\Phi}(f) \equiv \tilde{S}_{\Phi}(f) - \tilde{S}_{\Phi}(-f)$ with $T_0 = 10\text{mK}$, see Fig. 3.3b. Considering that the antisymmetric component of flux noise is proportional to the imaginary part of the susceptibility, this result might be taken as evidence for paramagnetic spins that would behave antiferromagnetically at lower temperatures, although more data is required to confirm this. There is no data on the temperature dependence of the exponent α for Al devices.

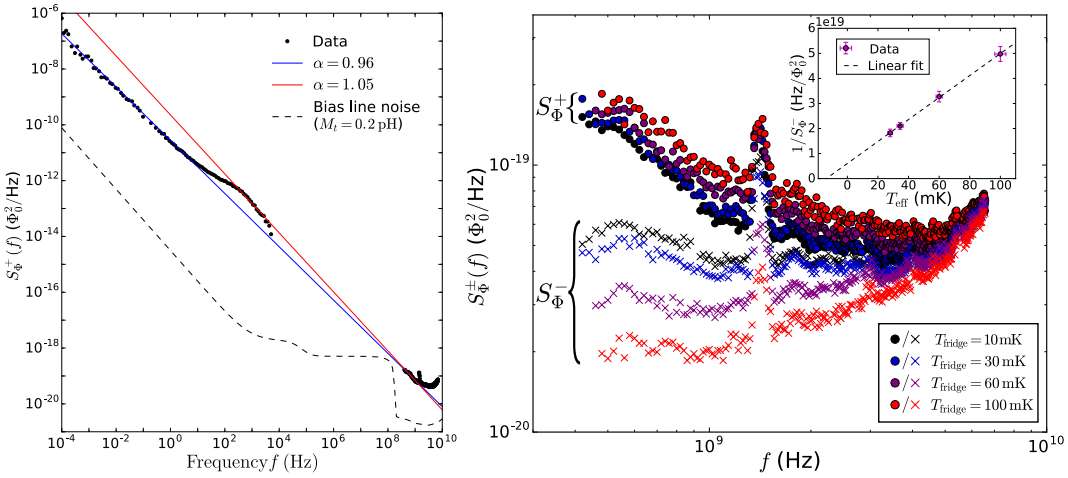

(a) *Freq. dependence.* **(b)** *Temp. dependence.*

Figure 3.3: ***Frequency and temperature dependence of flux noise in Al.*** **(a)** *Symmetric spectrum of flux noise $\tilde{S}^{+}_{\Phi}(f)$ results from [48]. Flux noise shows an approximately $1/f$ frequency dependence up to frequencies of 1 Ghz and an Ohmic or super-Ohmic dependence after this point [52].* **(b)** *Antisymmetric spectrum of flux noise $\tilde{S}^{-}_{\Phi}(f)$ (f = 500 MHz) from [48], showing a $1/(T+T_0)$ dependence, as plotted in the inset, T_0=10 mK [52].*

Additionally, a recent experiment measured for the first time the impact of weak magnetic fields in an Al SC flux qubit with a field oriented in the plane of the device [53]. For low

frequencies, 0.1 - 10 Hz, they observed an increase in the noise and a $1/f$ (B = 0 G) to approximately Lorentzian (B $\gtrsim$ 20 G) transition. The noise appears to show a non-monotonic behaviour, with a general increase with magnetic field from B = 0 G to B = 80 G and decreasing from B = 80 G to B = 100 G, the results can be seen in Fig. 3.4a. At higher frequencies, in the order of MHz they observed a suppression of the flux noise in fields up to B = 30 G with approximately $1/f$ noise, these results are shown in Fig. 3.4b. The origin of this magnetic field dependence in noise remains unknown.

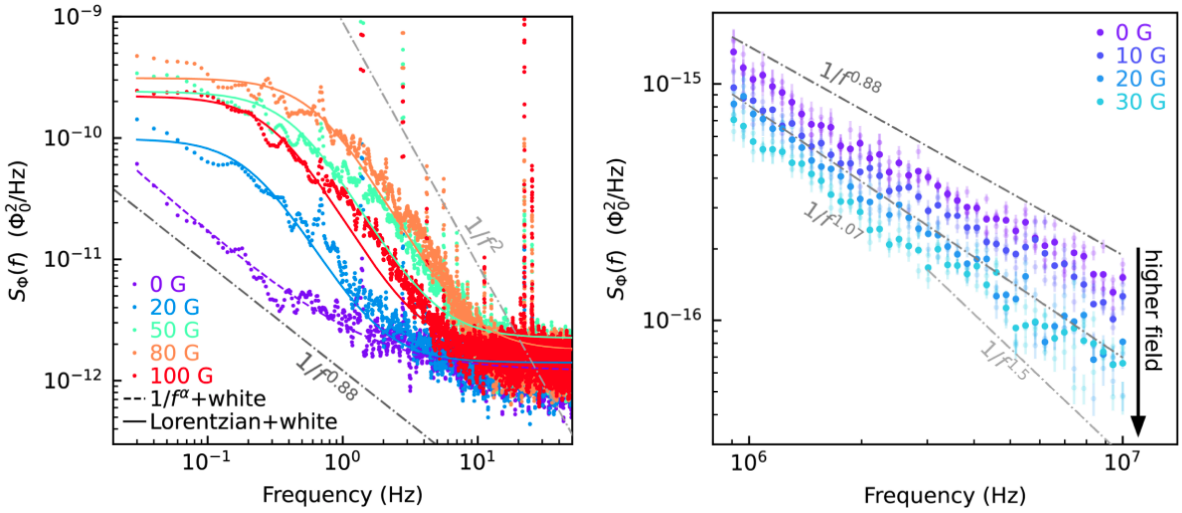

(a) *Low freq.* **(b)** *High freq.*

Figure 3.4: ***Magnetic field dependence of flux noise in Al.***
(a) *Low frequency results from [53]. The B = 0 G data is fit to a $1/f$ + white noise model and data at each non zero field is fit to a Lorentzian + white noise model. Noise shows a transition from $1/f$ to approximately Lorentzian noise with increasing field and a non-monotonic behaviour in amplitude, increasing with increasing field up to B = 80 G and decreasing for B = 80-100 G [54].* **(b)** *High frequency (in the MHz range) results from [53]. Data shows a decrease in noise with increasing field for approximately $1/f$ noise [54].*

3.2.3 Flux Noise in Niobium Devices

Anton et al. reported measurements of the temperature dependence of the exponent α in ten different Nb devices. They found that α decreases with temperature from 0.8 to 0.4 for T=0.1 -

4 K. The squared flux amplitude A_Φ^2 also decreases with temperature with some devices showing weaker dependence than others. These results are are incompatible with a model based on random single flips of independent spins [55]. Results shown in Fig. 3.5.

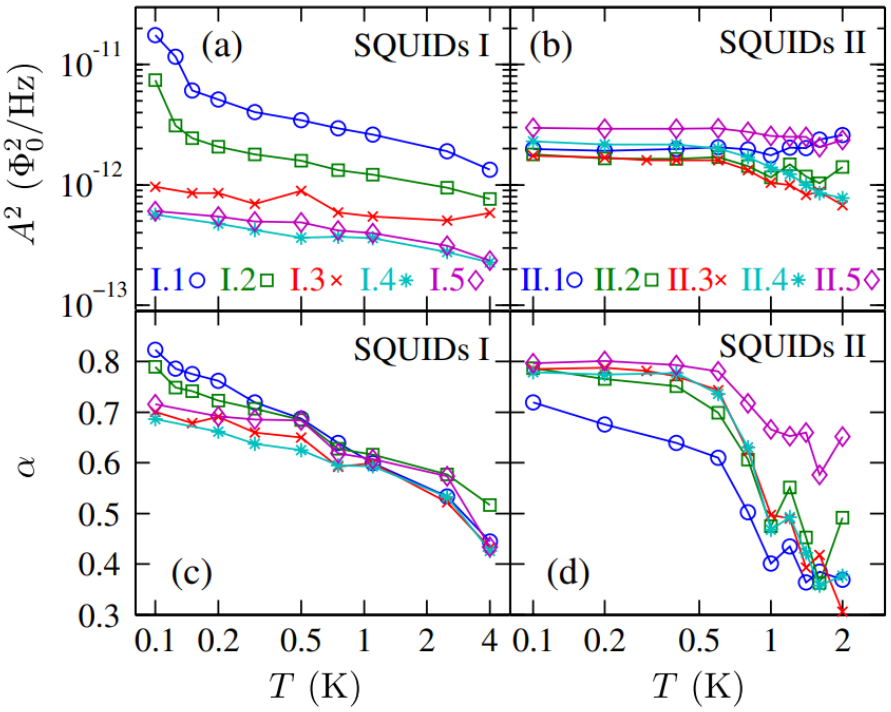

Figure 3.5: ***Temperature dependence of exponent α and amplitude A^2 in Nb.***
Results from [55]. The exponent α and squared flux amplitude A^2 decrease with temperature for T=0.1 - 4 K [56].

3.2.4 Charge Noise

Charge noise in qubits is often found to provide the dominant source of qubit energy relaxation, the $1/T_1$ rate. It refers to the unwanted fluctuations in the electric charge environment surrounding a qubit, and it originates from various sources, such as fluctuating single charges (trapping centers [57]) and fluctuating electric dipoles. The latter is often denoted "dielectric loss" as it causes single photon absorption. Candidate electric dipoles are TLSs [10, 58] and acoustic

phonons that acquire electric dipole moment due to the piezoelectric effect [59]. Another mechanism of charge noise is due to the presence of superconducting excitations called quasiparticles (See Chapter 7). Mitigating charge noise involves material purification and improved fabrication techniques. The charge noise in modern devices is often found to be dominated by either fluctuating electric dipoles from unknown TLSs [60] or by non-equilibrium QP densities.

Charge noise can be modeled in terms of the dielectric loss tangent $\tan(\delta)$, a measure of the energy dissipation within the dielectric materials used in the qubit. In a capacitor (see chapter 7 for a derivation):

$$\tilde{S}_Q(f) = 2\hbar C \tan(\delta) \left[n_B(f) + 1 \right], \tag{3.14}$$

where C is the capacitance and $n_B(f) = 1/(e^{hf/(k_B T)} - 1)$ is the Bose-Einstein distribution. The loss tangent is dominated by the group of TLSs whose energy splitting is resonant with the qubit. However, off-resonant TLSs may give rise to $1/f$ charge noise; this contribution may not be relevant in qubits that are insensitive to charge fluctuations, such as transmons.

3.2.5 Non-equilibrium Superconducting Quasiparticle Distributions

Several experiments find an unusually large population of QP excitations in superconducting devices, several orders of magnitude above their expected thermal population These non-equilibrium distributions are believed to arise due to ionizing radiation from cosmic rays and other sources. QP can absorb or emit energy, causing transitions between the qubit states and thus disrupting the delicate quantum superpositions necessary for quantum computation. QP-tunneling across junctions is particularly problematic because it can lead to both energy relaxation and dephasing of the qubit states [11–13, 61]. Chapter 7 delves more deeply into this loss mechanism and suggests that QPs can also be a source of charge and flux noise, even when they are not tunneling across Josephson junctions.

CHAPTER 4

General Spin Dissipation Theory of Flux Noise

This chapter is an expanded version of section II-IV in publication [1].

4.1 Introduction

As mentioned above, spin impurities are believed to be the main source of flux noise in flux-tunable devices. Two main models have been proposed to explain the noise currently observed in experiments: the single-spin-flip model and the spin-diffusion model due to spin-spin interactions.

The main mechanism for single spin-flips in FM metals, the so called Gilbert damping, relies on magnetic excitations (magnons) decaying into electron-hole pair excitations in the metal. In a superconductor these are exponentially suppressed at temperatures much lower than the SC energy gap, making the Gilbert damping constant exponentially small [62]. The only remaining mechanism for spin energy decay in superconductors is due to the interaction between each impurity spin with nearby amorphous TLS [6]. Such an interaction leads to wide distributions of single-spin-flip (relaxation) rates for different impurity spins [63].

When there are no single-spin flips in the system, the total spin magnetization is conserved, and the spin fluctuations due to spin-spin exchange interaction necessarily obey a spin diffusion equation at long wavelengths [64, 65]. Spin diffusion is a fundamental concept in condensed matter physics. The phenomenon of spin diffusion arises when there is a non-uniform distribution of spin polarization in a material, leading to a net flow of spin angular momentum. A recent "pump and probe" experiment [49] measured the flux time correlation function $\langle\hat{\Phi}(t)\hat{\Phi}(0)\rangle$ in SQUIDs, and showed that it behaved similar to Brownian motion in the $1 - 1000$ μs time range,

this provides evidence that the dynamics of flux Φ in a SC device is described by the phenomena of diffusion in this time range.

Describing spin diffusion from "first principles", i.e. by integrating the Heisenberg equations of motion for a model of interacting spins, is a well known challenge of theoretical physics [65]. The standard method is what we call "third-principles approach": It assumes the spins can be described by a continuous magnetization density $\boldsymbol{M}(\boldsymbol{r},t)$ that satisfies the phenomenological equation $\frac{\partial \boldsymbol{M}}{\partial t} = D\nabla^2\boldsymbol{M}$, with D the spin diffusion constant. With all physical properties lumped into a phenomenological constant D, the third-principles theory can not establish a connection to microscopic model spin Hamiltonians, spin spatial distributions, and the impact of inhomogeneity and clusters.

A serious shortcoming of the third principles approach is that it requires the assumption of a hard boundary condition such as $\boldsymbol{M}(\boldsymbol{r},t) = \boldsymbol{0}$ at wire edges and the surface of spin clusters in order to ensure total spin conservation across the boundaries [45, 49]. A hard boundary condition like this is unjustifiable and, in fact, is known to be violated in magnetic systems due to the appearance of confined surface or edge magnons [66]. Developing a theory of spin dynamics that properly accounts for the boundary effects is of crucial importance because flux noise is known to be dominated by spins at the edge of the wire where the supercurrent is maximum [5, 51].

The purpose of this chapter is to propose a "second principles" theoretical framework for spin dissipation (diffusion plus relaxation) that includes quantum noise and is more "microscopic" than the usual third-principles approach. The goal is to establish a connection between flux noise measured in experiments and microscopic spin Hamiltonians without the prohibitive computational cost associated with the first-principles approach. To do this, we assume spin dissipation according to a random walk model governed by the parameters of the spin Hamiltonian such as the microscopic exchange interaction between each pair of spins.

This chapter is organized as follows: Section 4.2 describes the flux noise model due to spins used in the following sections. Section 4.3 describes the spin dissipation model including diffusion from spin-spin interactions and spin-lattice relaxation, we present a proposed equation of motion and a discrete version of the diffusion operator. We finalize with the conclusions of this chapter in section 4.4.

4.2 Spin Flux Noise Model

In this section, we describe the impact of wire currents on impurity spins and how it leads to a general expression for flux noise. Consider a system of spins placed on the surface of a SC wire. The magnetic moment of an impurity spin is given by $-g\mu_B\hat{\boldsymbol{s}}_i$, where $g \approx 2$ is the g-factor, μ_B is the Bohr magneton, and $\hat{\boldsymbol{s}}_i$ is a dimensionless spin operator for an impurity located at position $\boldsymbol{R}_i$. It couples to the SC wire current density by producing a flux [51],

$$\hat{\Phi} = -\sum_i x_i \boldsymbol{F}(\boldsymbol{R}_i) \cdot \hat{\boldsymbol{s}}_i, \tag{4.1}$$

where the sum goes over all sites $\boldsymbol{R}_i$ of a virtual square lattice containing N sites. The variable $x_i = 1$ when there is a spin at the virtual site, and $x_i = 0$ otherwise, and the spin density is $\sigma = \sum_i x_i/N = N_s/N$, where N_s is the number of spins. The flux vector $\boldsymbol{F}(\boldsymbol{r})$ is directly proportional to $\boldsymbol{B}_I(\boldsymbol{r})$, the magnetic field produced by the wire's current density: $\boldsymbol{F}(\boldsymbol{r}) = g\mu_B\boldsymbol{B}_I(\boldsymbol{r})/I$, where I is the total current flowing through the wire.

The wire's current in turn affect spins by imprinting an *external* local field

$$\boldsymbol{h}_i = -g\mu_B\boldsymbol{B}_I(\boldsymbol{R}_i) = -I\boldsymbol{F}(\boldsymbol{R}_i), \tag{4.2}$$

that couples to the spin according to $\mathcal{H}_c = -\sum_i x_i\boldsymbol{h}_i \cdot \hat{\boldsymbol{s}}_i$, so $\boldsymbol{h}_i$ has dimensions of energy. When the local field $\boldsymbol{h}_i$ is time-dependent, the spins respond according to

$$\langle \hat{s}_i^a(t)\rangle_{h\neq 0} = \langle \hat{s}_i^a(t)\rangle_{h=0} + \sum_{j,b}\int_{-\infty}^{\infty} dt' \chi_{ij}^{ab}(t-t')h_j^b(t'), \tag{4.3}$$

where $a, b = x, y, z$ and $\chi_{ij}^{ab}(t)$ is the dynamical susceptibility. Defining spin noise as

$$\tilde{S}_{ij}^{ab}(\omega) = x_i x_j \int_{-\infty}^{\infty} dt e^{i\omega t}\langle[\hat{s}_i^a(t) - \langle\hat{s}_i^a\rangle][\hat{s}_j^b(0) - \langle\hat{s}_j^b\rangle]\rangle, \tag{4.4}$$

we can relate this expression to the imaginary part of the dynamical susceptibility using the fluctuation-dissipation theorem (see Appendix A). The fluctuation-dissipation theorem for spins

is

$$\tilde{S}_{ij}^{ab}(\omega) = 2\hbar\,(n_B(\omega)+1)\,\mathrm{Im}\{\tilde{\chi}_{ij}^{ab}(\omega)\}, \tag{4.5}$$

with $n_B(\omega) = 1/(e^{\hbar\omega/(k_BT)}-1)$ is the Bose-Einstein distribution. $\tilde{\chi}_{ij}^{ab}(\omega)$ is the Fourier transform of $\chi_{ij}^{ab}(t)$:

$$\tilde{\chi}_{ij}^{ab}(\omega) = \int_{-\infty}^{\infty} dt e^{i\omega t}\chi_{ij}^{ab}(t), \tag{4.6}$$

and

$$\chi_{ij}^{ab}(t) = \frac{1}{2\pi}\int_{-\infty}^{\infty} d\omega e^{-i\omega t}\tilde{\chi}_{ij}^{ab}(\omega). \tag{4.7}$$

The flux noise, the PSD of flux fluctuations as defined in Eq. (3.5), is then given by

$$\begin{aligned}\tilde{S}_{\Phi}(\omega) &= \int_{-\infty}^{\infty} dt \mathrm{e}^{i\omega t}\left\langle \delta\hat{\Phi}(t)\delta\hat{\Phi}(0)\right\rangle \\ &= \sum_{i,j,a,b} F^a(\boldsymbol{R}_i)\tilde{S}_{ij}^{ab}(\omega)F^b(\boldsymbol{R}_j),\end{aligned} \tag{4.8}$$

where $\delta\hat{\Phi}(t) = \hat{\Phi}(t) - \langle\hat{\Phi}\rangle$ denotes flux fluctuation.

4.3 General Spin Dissipation Model

In this section we present an extension to the usual third principles approach for spin diffusion by proposing a discrete version of diffusion and considering reactive dynamics ignored in simpler models, this approach is able to account for disorder and thermal effects, as well as the effects of external magnetic fields. We also incorporate spin-lattice relaxation in the spins' equation of motion, accounting for disorder due to a wide distribution of individual spin-flip rates Γ_i

4.3.1 Free Energy in the Mean Field Approximation

Consider a system of spins $\mathbf{s}_i$ interacting with each other, each spin is also coupled to an external local field $\mathbf{h}_i$. The system is thus described by the Heisenberg Hamiltonian

$$\mathcal{H} = -\frac{1}{2}\sum_{i,j} x_i x_j J_{ij}\hat{\boldsymbol{s}}_i\cdot\hat{\boldsymbol{s}}_j - \sum_i x_i\boldsymbol{h}_i\cdot\hat{\boldsymbol{s}}_i. \tag{4.9}$$

Here, J_{ij} is the exchange interaction between spins i and j. This interaction can be FM, $J_{ij} > 0$; or AFM, $J_{ij} < 0$.

In mean-field theory we neglect higher order fluctuations by approximating $\langle \hat{s}_i^a \hat{s}_j^b \rangle \approx \langle \hat{s}_i^a \rangle \langle \hat{s}_j^b \rangle$. We simplify the notation by writing $\langle \hat{\boldsymbol{s}}_i \rangle = \boldsymbol{s}_i$, i.e. the spin vector without a hat denotes the average of the spin operator (a real vector). The mean-field approximation is exactly the same as the "classical spin model" used by many authors, e.g. [67]. An additional approximation in mean-field theory is to assume the system's entropy can be written as a sum of single-spin entropies. To calculate the average entropy of a single spin, we assume the spin is coupled to an average magnetic field B by a Hamiltonian $\mathcal{H}_1 = g\mu_B B \hat{s}^z$. The partition function in the canonical ensemble is given by

$$\mathcal{Z} = 2\cosh\left(\frac{g\mu_B B}{2k_B T}\right), \tag{4.10}$$

and the free energy of the single-spin system is

$$\mathcal{F}_1 = -k_B T \log(\mathcal{Z}) = \langle \mathcal{H}_1 \rangle - T\langle \mathcal{S}_1 \rangle, \tag{4.11}$$

where $\mathcal{S}_1$ is the entropy of the spin and T is the temperature of the thermal bath. We can calculate the entropy:

$$\langle \mathcal{S}_1 \rangle / k_B = \frac{g\mu_B B}{k_B T} s + \log\left(2\cosh\left(\frac{g\mu_B B}{2k_B T}\right)\right). \tag{4.12}$$

s is the thermal average of the spin:

$$s = \langle \hat{s}^z \rangle = \frac{1}{\mathcal{Z}} \sum_\alpha \langle \alpha | \hat{s}^z | \alpha \rangle = -\frac{1}{2}\tanh\left(\frac{g\mu_B B}{2k_B T}\right). \tag{4.13}$$

From this relation, the magnetic field B can be written as

$$B = \frac{k_B T}{g\mu_B} \log\left(\frac{1-2s}{1+2s}\right), \tag{4.14}$$

for $-\frac{1}{2} < s < \frac{1}{2}$. The entropy is then

$$\begin{aligned}\langle \mathcal{S}_1 \rangle / k_B &= \log 2 - s\log\left(\frac{1+2s}{1-2s}\right) - \frac{1}{2}\log\left(1-4s^2\right) \\ &\approx \log 2 - 2s^2 - \frac{4}{3}s^4, \end{aligned} \tag{4.15}$$

where in the last line we assumed that $\boldsymbol{s}$ is sufficiently small (B is small) and dropped higher order terms. The free energy of the entire system is thus given by

$$\begin{aligned}\mathcal{F} &= \langle \mathcal{H} \rangle - T\langle \mathcal{S} \rangle = -\frac{1}{2}\sum_{i,j} x_i x_j J_{ij} \boldsymbol{s}_i \cdot \boldsymbol{s}_j - \sum_i x_i \boldsymbol{h}_i \cdot \boldsymbol{s}_i \\ &\quad -k_B T \sum_i x_i \left[\log 2 - 2|\boldsymbol{s}_i|^2 - \frac{4}{3}|\boldsymbol{s}_i|^4\right], \end{aligned} \tag{4.16}$$

note that this is a good approximation when $h_i^z = g\mu_B B \ll k_B T$ and $T \gg T_c^{\mathrm{mag}}$, where T_c^{mag} is a critical temperature for a phase where $s_i > 0$.

In the opposite limit $s \to= -\frac{1}{2}$ ($s \to= \frac{1}{2}$), we can interpret this as the result of a large local field $B > 0$ ($B < 0$) on spin $\boldsymbol{s}$ (either from a large external magnetic field or due to strong interactions with neighbouring spins). In this case the entropy is

$$\begin{aligned}\langle \mathcal{S}_1 \rangle / k_B &= \frac{g\mu_B B}{k_B T} s + \log\left(2\cosh\left(\frac{g\mu_B B}{2k_B T}\right)\right) \\ &\approx -\frac{g\mu_B B}{2k_B T} + \log\left(\exp\left(\frac{g\mu_B B}{2k_B T}\right)\right) = 0. \end{aligned} \tag{4.17}$$

The free energy in this regime can then be approximated by:

$$\mathcal{F} = \langle \mathcal{H} \rangle = -\frac{1}{2}\sum_{i,j} x_i x_j J_{ij} \boldsymbol{s}_i \cdot \boldsymbol{s}_j - \sum_i x_i \boldsymbol{h}_i \cdot \boldsymbol{s}_i. \tag{4.18}$$

We will assume that $|s| \ll \frac{1}{2}$ and use Eq. (4.16) to calculate the free energy hereinafter, the opposite limit can be obtained by taking $T \to 0$ in the free energy expression.

Thermal equilibrium is realized by the set of $\boldsymbol{s}_i$ that leads to the global minimum of the free energy. For example, take $x_i = 1, h_i = 0$ for all i, $J_{ij} = J > 0$ for nearest neighbors (NN) and zero otherwise, and a lattice with periodic boundary conditions (b.c.). In this case the global minimum of $\mathcal{F}$ is realized by $\boldsymbol{s}_i = \boldsymbol{s}^{\rm eq}$ for all i (the FM homogeneous state), with free energy given by

$$\frac{\mathcal{F}}{N} = \left(2k_BT - \frac{\gamma J}{2}\right)(s^{\rm eq})^2 + \frac{4}{3}k_BT(s^{\rm eq})^4 - k_BT\ln 2, \tag{4.19}$$

where γ is the number of NN for each site of the lattice. From this expression we see that a global minimum with $s^{\rm eq} > 0$ appears only when the first term changes sign, leading to critical temperature $k_BT_c^{\rm mag} = k_BT_{\rm CW} = \gamma J/4$. The same calculation can be done for $J < 0$ when the lattice can be partitioned into two sublattices with one being n.n. to the other. For this case the global minimum of $\mathcal{F}$ is realized by $\boldsymbol{s}_i = +\boldsymbol{s}^{\rm eq}$ for one sublattice and $\boldsymbol{s}_i = -\boldsymbol{s}^{\rm eq}$ for the other (AFM homogeneous state). This leads to $k_BT_c^{\rm mag} = \gamma|J|/4$. However, $k_BT_{\rm CW} = -\gamma|J|/4$ because the magnetic susceptibility does not have a singularity at $T_c^{\rm mag}$. These are the well-known mean-field results for phase transitions in the spin-$1/2$ Heisenberg model [68].

4.3.2 Spin Dynamics

We propose that spin dynamics follow the generalized equation of motion

$$\frac{d\boldsymbol{s}_i}{dt} = \frac{1}{\hbar}\boldsymbol{s}_i \times \boldsymbol{H}_i - \sum_j D_{ij}\boldsymbol{H}_j - \Gamma_i(\boldsymbol{s}_i - \boldsymbol{s}_i^{\rm inst\ eq}), \tag{4.20}$$

where $\boldsymbol{H}_i$ is an internal spin field, defined below. This equation is expected to be valid for frequencies smaller than a cut-off Ω_c to be discussed later. In addition to the usual spin precession, this includes a discrete version of the *intra-spin dissipation* operator D_{ij}, together with *spin energy relaxation* Γ_i assumed to be isotropic. The Γ_i drives $\boldsymbol{s}_i$ towards its "instantaneous equilibrium" value

$$\boldsymbol{s}_i^{\rm inst\ eq} = \boldsymbol{s}_i^{\rm eq} + \sum_j \tilde{\chi}_{ij}(0)\delta\boldsymbol{h}_j(t), \tag{4.21}$$

which is time-dependent due to local field dynamics, $\boldsymbol{h}_i(t) = \boldsymbol{h}_i^{\rm eq} + \delta\boldsymbol{h}_i(t)$, where $\boldsymbol{h}_i^{\rm eq}$ is the static part. The quantities $\boldsymbol{s}_i^{\rm eq}$ do not depend on time, they are thermal equilibrium averages calculated

assuming $\delta\boldsymbol{h}_i(t) = 0$, i.e. they only depend on $\boldsymbol{h}_i^{\rm eq}$ and other static free energy parameters; $\tilde{\chi}_{ij}^{ab}(0) = \partial(s_i^{\rm eq})^a/\partial h_j^b$ is the $\omega = 0$ susceptibility, assumed isotropic ($\propto \delta_{ab}$) to be consistent with our Hamiltonian, Eq. (4.9). We call Eq. (4.21) the "instantaneous approximation", because it assumes the other degrees of freedom causing spin energy relaxation relax much faster than the spins themselves, so that the spin system remains in thermal equilibrium with the other non-spin degrees of freedom at all times. Note how Eq. (4.21) introduces the $\omega = 0$ susceptibility *self-consistently* into the equation of motion (4.20).

The *internal* spin field is defined as

$$\boldsymbol{H}_i = -\frac{\partial \mathcal{F}}{\partial \boldsymbol{s}_i} = x_i \left\{ \sum_j x_j J_{ij} \boldsymbol{s}_j + \boldsymbol{h}_i - 4k_B T \left[1 + \frac{4}{3} s_i^2 \right] \boldsymbol{s}_i \right\}, \tag{4.22}$$

and the thermal equilibrium spin averages $\boldsymbol{s}_i^{\rm eq}$ are determined by imposing time independence, $\boldsymbol{h}_i(t) - \boldsymbol{h}_i^{\rm eq} = \delta\boldsymbol{h}_i(t) = \boldsymbol{0}$ and $\frac{d\boldsymbol{s}_i}{dt} = \boldsymbol{0}$ for all i. This implies $\boldsymbol{s}_i^{\rm eq}$ must be found by solving the system of equations

$$\frac{1}{\hbar} \boldsymbol{s}_i^{\rm eq} \times \boldsymbol{H}_i^{\rm eq} - \sum_j D_{ij} \boldsymbol{H}_j^{\rm eq} = \boldsymbol{0}, \tag{4.23}$$

where $\boldsymbol{H}_i^{\rm eq}$ is Eq. (4.22) with $\boldsymbol{s}_i = \boldsymbol{s}_i^{\rm eq}$ and $\boldsymbol{h}_i = \boldsymbol{h}_i^{\rm eq}$. Note how Eq. (4.23) is always satisfied for $\boldsymbol{H}_i^{\rm eq} = \boldsymbol{0}$, a smooth local minimum of the free energy. However, other solutions with $\boldsymbol{H}_i^{\rm eq} \neq \boldsymbol{0}$ may arise in the presence of site-dependent local fields $\boldsymbol{h}_i^{\rm eq}$.

The three terms in the right hand side of Eq. (4.20) correspond to reactive dynamics, intra-spin-system dissipation (e.g. diffusion), and spin energy relaxation due to other degrees of freedom, respectively. The reactive term is non-dissipative, it does not change sign under time reversal $t \to -t$ so it has the same symmetry as the left hand side. The second and third terms on the right hand side do change sign under time reversal, leading to an irreversible approach to thermal equilibrium (the arrow of time). These terms must be added *ad hoc* to the linearized equations of motion so that the zeroth (attainment of thermal equilibrium) and second (entropy always increases) laws of thermodynamics are obeyed. That is, the system is able to reach thermal equilibrium, and the free energy always decreases as a function of time when the system is in contact with a thermal reservoir.

The normal modes of Eq. (4.20) are called *magnons* and *paramagnons*, to be defined below.

The reactive terms of Eq. (4.20) describe the dynamics of noninteracting (para)magnons obtained by the mean-field approximation. Exactly the same results are obtained from different methods, e.g. using a Holstein-Primakoff transformation to convert spin operators into Bosonic creation/destruction operators; transforming Hamiltonian (4.9) and keeping contributions that are quadratic in these Bosonic operators leads to the same magnon modes as Eq. (4.20) with $D_{ij} = \Gamma_i = 0$ [66]. However, the higher order terms that are neglected in this quadratic approximation can be interpreted as describing (para)magnon-(para)magnon interactions. The introduction of $D_{ij} \neq 0$ serves to account for these interactions phenomenologically.

4.3.3 Dissipation Matrix

To go beyond the third-principles assumption of long wavelength spin diffusion we need to come up with a specification for D_{ij} that respects several physical constraints. To do this, we take inspiration from random walk models in a lattice. The key idea is that exchange interaction J_{ij} is the main driver for each random walk step, a spin "flip-flop". A sequence of many flip-flops will lead to diffusion. The constraint of total spin conservation motivates our postulation of the following spin dissipation matrix:

$$D_{ij} = \frac{d_0(T)}{\hbar \bar{J}_i^c} \left(x_i x_j |J_{ij}| - \delta_{ij} \sum_k x_i x_k |J_{ik}| \right). \tag{4.24}$$

Here $d_0(T)$ is a function of temperature to be determined by fitting the theory to experiments (note $d_0(T)$ is dimensionless). This additional temperature dependence is introduced to account for critical behaviour of the spin diffusion constant near T_c^{mag} [69]. However, when all $J_{ij} = 0$, we necessarily have $D_{ij} = 0$, i.e. no diffusion can occur. Because of this we also expect $d_0(T) \to 0$ when all $J_{ij} \to 0$. The quantity

$$\bar{J}_i^c = \frac{1}{N_c} \sum_{j,k \in \text{cluster } c} x_j x_k |J_{jk}| \tag{4.25}$$

is the average exchange times coordination number for c^{th} cluster, the cluster that contains spin i. Such a cluster is defined as the set of all spins j such that either $J_{ij} \neq 0$ or there exists a set of

sites $k_1, k_2, \ldots, k_n$ such that $J_{ik_1}J_{k_1k_2}J_{k_2k_3}\cdots J_{k_nj} \neq 0$. N_c is the number of spins in the isolated cluster c. The following motivates this choice:

1. When the local external field $\boldsymbol{h}_i$ and spin relaxation rate Γ_i are both zero, Eq. (4.24) preserves total spin. From Eq. (4.20), for each isolated spin cluster:

$$\begin{aligned}\frac{d}{dt}\left(\sum_{i\in\text{cluster}} \boldsymbol{s}_i\right) &= -\sum_{i,j\in\text{cluster}} D_{ij}\boldsymbol{H}_j \\ &= -\frac{d_0(T)}{\hbar}\sum_{i,j\in\text{cluster}}\frac{1}{\bar{J}_i^c}\left(x_ix_j|J_{ij}| - \delta_{ij}\sum_k x_ix_k|J_{ik}|\right) \\ &\times \left(\sum_q x_qJ_{jq}\boldsymbol{s}_q - 4k_BT\left[1+\frac{4}{3}s_j^2\right]\boldsymbol{s}_j\right) = \boldsymbol{0}, \end{aligned} \tag{4.26}$$

   so the total spin in each cluster is a constant of the motion. Therefore, we do not need to assume hard boundary conditions [45, 49] to describe confined systems such as spin clusters and wire edges.

2. This choice for D_{ij} gives rise to diffusion in the long wavelength regime when $\Gamma_i = 0$ for all i. For the homogeneous NN model in the square lattice with $J_{ij} = J_{i,i+\boldsymbol{v}} = J$ for $\boldsymbol{v} = \pm a_0\hat{x}, \pm a_0\hat{z}$ with a_0 the inter-atomic distance and $x_i = 1$ for all i, defining the magnetization density $\boldsymbol{M}(\boldsymbol{r}) = -\sum_i \boldsymbol{s}_i\delta(\boldsymbol{r}-\boldsymbol{R}_i)$ and assuming high temperature ($k_BT \gg J$ and $(\boldsymbol{s}_i)^2 \ll 1$), we calculate:

$$\begin{aligned}\frac{d}{dt}\boldsymbol{M}(\boldsymbol{r}) &= \sum_{i,j}\delta(\boldsymbol{r}-\boldsymbol{R}_i)D_{ij}\boldsymbol{H}_j \\ &\approx -\frac{4d_0(T)k_BT}{\hbar}\sum_{i,j}\delta(\boldsymbol{r}-\boldsymbol{R}_i)\frac{1}{\bar{J}_i^c}\left(|J_{ij}| - \delta_{ij}\sum_k|J_{ij}|\right)\boldsymbol{s}_j \\ &= \frac{d_0(T)k_BT}{\hbar}\sum_i\delta(\boldsymbol{r}-\boldsymbol{R}_i)\left(4\boldsymbol{s}_i - \sum_{\boldsymbol{v}}\boldsymbol{s}_{i+\boldsymbol{v}}\right) \\ &= \frac{d_0(T)a_0^2k_BT}{\hbar}\nabla^2\boldsymbol{M}(\boldsymbol{r}), \end{aligned} \tag{4.27}$$

where $\boldsymbol{s}_{i+\boldsymbol{v}}$ is the spin $\boldsymbol{s}$ at the location $\boldsymbol{R}_i + \boldsymbol{v}$ and the discrete derivative in the lattice is $\frac{df_i}{dx} = \frac{f_{i+a_0\hat{\boldsymbol{x}}} - f_{i-a_0\hat{\boldsymbol{x}}}}{2a_0}$. Equation (4.27) may be compared to experiments that show a spin diffusion constant increasing with temperature [8].

3. Consider the time derivative of the free energy in each isolated spin cluster when $\boldsymbol{h}_i$ is independent of time:

$$\begin{aligned}\frac{d\mathcal{F}}{dt} &= \sum_i \frac{\partial \mathcal{F}}{\partial \boldsymbol{s}_i} \cdot \frac{d\boldsymbol{s}_i}{dt} = \frac{d_0(T)}{\hbar} \sum_i \frac{1}{\bar{J}_i^c} \boldsymbol{H}_i \cdot \sum_j x_i x_j |J_{ij}| (\boldsymbol{H}_j - \boldsymbol{H}_i) + \sum_i \Gamma_i \boldsymbol{H}_i \cdot (\boldsymbol{s}_i - \boldsymbol{s}_i^{\mathrm{eq}}) \\ &= -\frac{d_0(T)}{\hbar} \sum_{i<j} \frac{1}{\bar{J}_i^c} x_i x_j |J_{ij}| (\boldsymbol{H}_i - \boldsymbol{H}_j)^2 - \sum_i \Gamma_i \left(\mathcal{F}(\boldsymbol{s}_i) - \mathcal{F}(\boldsymbol{s}_i^{\mathrm{eq}}) + \mathcal{O}\left[(\delta \boldsymbol{s}_i)^2 \right] \right) \end{aligned} \quad (4.28)$$

The first term on the RHS is always negative, showing that our choice for D_{ij} always tends to decrease the free energy as time increases (i.e. it obeys the 2nd law of thermodynamics). This justifies our use of modulus of J_{ij} in Eq. (4.24).

The second term on the RHS of Eq. (4.28) is negative provided that the deviation out of equilibrium is small and $\mathcal{F}(\boldsymbol{s}_i^{\mathrm{eq}})$ is a local minimum of the free energy. Therefore, the coupling to other non-spin degrees of freedom Γ_i pushes the system towards a local minimum of the free energy, without subjecting to spin conservation.

We remark that our choice of using the local field H_j in the dissipation term of Eq. (4.20) guarantees both the first and seconnd law of thermodynamics are satisfied:

1. $\frac{d\boldsymbol{s}_i}{dt} = 0$ for a smooth local minimum of the free energy, $\boldsymbol{H}_i^{\mathrm{eq}} = \boldsymbol{0}$, even when local fields are inhomogeneous.

2. This choice allows us to group the product $\boldsymbol{H}_i \cdot (\boldsymbol{H}_j - \boldsymbol{H}_i)$ as $(\boldsymbol{H}_i - \boldsymbol{H}_j)^2$ in Eq. (4.28). This guarantees that the entropy always increases with time.

This justifies our choice of the term $D_{ij} H_j$ in Eq. (4.20). Note, however, that other choices could satisfy these conditions.

4.4 Conclusions

We developed a "second principles" theory of flux noise due to spin dissipation due to spin-spin interactions and spin-lattice relaxation. The theory is able to account for the confinement and disorder present in realistic impurity spins systems on SC devices. The theory proposes a discrete version of dissipation given by the matrix D_{ij}, Eq. (4.24). D_{ij} depends on spin Hamiltonian parameters such as exchange interaction, establishing a direct connection between flux noise and model spin Hamiltonians. This framework also allows for energy exchange between the spins and other degrees of freedom like phonons and amorphous TLSs modeled as relaxation terms Γ_is. The theoretical framework allows explicit prediction of the amplitude and exponent of flux noise due to different wire geometries and spin disorder scenarios, such as random vacancies and relaxation rates. We use this theory to calculate flux noise explicitely in chapters 5 and 6.

CHAPTER 5

Flux Noise due to Spin-Lattice Relaxation and Dependence on External Magnetic Fields

This chapter is an expanded version of publication [2].

5.1 Introduction

In this chapter we propose a theoretical model based on the assumption of an ensemble of independent impurity spins placed on the surface of the SC wire with dynamics governed by single spin flips (spin relaxation), this model is equivalent to the general model presented in chapter 4 with no spin-spin interactions, $D_{ij} = J_{ij} = 0$, in this case, each spin can be treated independently and flux noise can be calculated analytically. The model provides a possible explanation for many of the less understood aspects of flux noise in Al devices, such as $1/f$ noise and its dependence on the magnetic field. In section 5.2 we start by defining the general properties of our model for a single spin under spin relaxation, this results in lorentzian flux noise. In section 5.3 we consider an ensemble of spins with a wide distribution of cross-relaxation rates, this model results in $1/f$ noise in a large interval of frequencies. In section 5.4 we consider the effect of direct spin relaxation, in this model, the transition from $1/f$ to lorentzian noise observed in experiments is a natural consequence on the magnetic field dependence of direct relaxation. Finally, section 5.5 presents the conclusions.

5.2 Single Spin Model

Consider a single spin on the surface of a SC wire as in Figure 5.1. The spin is coupled to the wire's current according to the Hamiltonian,

$$\mathcal{H} = g\mu_B \boldsymbol{B} \cdot \hat{\boldsymbol{s}}, \tag{5.1}$$

where $\boldsymbol{B} = \boldsymbol{B}_I(\boldsymbol{R}) + \boldsymbol{B}_{\text{ext}}$ is the spin's local field, including $\boldsymbol{B}_I(\boldsymbol{r})$, the magnetic field produced by the wire's current density, and an externally applied field $\boldsymbol{B}_{\text{ext}}$. For typical SQUIDs, $I \lesssim 1$ μA, leading to peak $B_I < \mu_0 I/b \sim 0.1$ G where $b \sim 0.1$ μm is the thickness of the SC wire. As a result it is safe to approximate $\boldsymbol{B} \approx \boldsymbol{B}_{\text{ext}}$ when $B_{\text{ext}} > 1$ G. From this point on we write $\boldsymbol{h} = -g\mu_B \boldsymbol{B}$ as in Eq. (4.2).

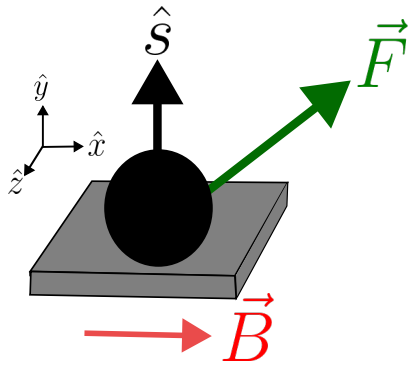

Figure 5.1: ***Single spin on the surface of the superconducting wire.***
The spin $\hat{\boldsymbol{s}}$ is coupled to the magnetic field generated by the wire's current and to an external magnetic field, the total field is $\boldsymbol{B}$. $\boldsymbol{F}$ is the flux vector at the spin's location.

Note that $\tilde{S}^{ab}(\omega) = -\tilde{S}^{ba}(\omega)$ when $a \neq b$, this follows from the fluctuation-dissipation theorem for spins, Eq.(4.5), and the observation that the susceptibility $\tilde{\chi}^{ab}(\omega)$ is real when $a \neq b$. The flux noise produced by the spin, Eq. (4.8), simplifies to

$$\begin{aligned} \tilde{S}_\Phi(\omega) &= \left|\boldsymbol{F} \cdot \hat{\boldsymbol{h}}\right|^2 \tilde{S}^{\parallel}(\omega) + \left|\boldsymbol{F} \times \hat{\boldsymbol{h}}\right|^2 \tilde{S}^{\perp}(\omega) \\ &= |F^z|^2 \, \tilde{S}^{zz}(\omega) + |F^x|^2 \, \tilde{S}^{xx}(\omega). \end{aligned} \tag{5.2}$$

Here $\hat{\boldsymbol{h}}$ is the unit vector pointing along the local magnetic field acting on the spin, $\tilde{S}^{\parallel}(\omega) \equiv \tilde{S}^{\hat{h}\hat{h}}(\omega)$, and $\tilde{S}^{\perp}(\omega) \equiv \tilde{S}^{\hat{P}\hat{P}}(\omega)$ were $\hat{\boldsymbol{P}}$ is any direction perpendicular to $\boldsymbol{h}$. Without loss of generality we chose $\parallel = zz, \perp = xx = yy$ in Eq. (5.2).

When relaxation processes are considered, the evolution of the ensemble average of the spin operator $\boldsymbol{s} = \langle \hat{\boldsymbol{s}} \rangle$ is described by the Bloch equations [70]:

$$\frac{d}{dt}s^x = \frac{g\mu_B}{\hbar}[\boldsymbol{B} \times \boldsymbol{s}]^x - \Gamma_2[s^x - s^{\text{inst eq, } x}], \tag{5.3a}$$

$$\frac{d}{dt}s^y = \frac{g\mu_B}{\hbar}[\boldsymbol{B} \times \boldsymbol{s}]^y - \Gamma_2[s^y - s^{\text{inst eq, } y}], \tag{5.3b}$$

$$\frac{d}{dt}s^z = \frac{g\mu_B}{\hbar}[\boldsymbol{B} \times \boldsymbol{s}]^z - \Gamma_1[s^z - s^{\text{inst eq, } z}]. \tag{5.3c}$$

In addition to spin precession, this equation includes *spin energy relaxation rate* $\Gamma_1 = \frac{1}{T_1}$ and *spin decoherence rate* $\Gamma_2 = \frac{1}{T_2} \geq \Gamma_1/2$. These drive $\boldsymbol{s}$ towards its "instantaneous equilibrium" value

$$\boldsymbol{s}^{\text{inst eq}} = \boldsymbol{s}^{\text{eq}} + \sum_{a=x,y,z} \tilde{\chi}^{aa}(0)\delta\boldsymbol{h}^a(t), \tag{5.4}$$

where $\tilde{\chi}^{zz}(0)$ and $\tilde{\chi}^{xx}(0) = \tilde{\chi}^{yy}(0)$ are the $\omega = 0$ longitudinal and transverse susceptibilities, respectively. Eq. (5.3a) is equivalent to Eq. (4.20) for a single spin with no spin-spin interactions, $D_{ij} = J_{ij} = 0$, note that in this case we assume the relaxation rates along the directions parallel and perpendicular to the external magnetic field are not necessarily equal, this also implies the zero-frequency susceptibilities along x and z can differ from each other. For small deviations from equilibrium we write $\boldsymbol{h} \to \boldsymbol{h}^{\text{eq}} + \delta\boldsymbol{h}(t)$, and $\boldsymbol{s} \to \boldsymbol{s}^{\text{eq}} + \delta\boldsymbol{s}(t)$, where both $\delta\boldsymbol{h}(t)$ and $\delta\boldsymbol{s}(t)$ are small time-dependent perturbations. Plugging these into Eq. (5.3a) and dropping non-linear terms enables the calculation of the dynamical susceptibility. In the $\hat{z}$ direction, the equation of motion in Fourier space is

$$(\omega + i\Gamma_1)\delta\tilde{s}^z = i\Gamma_1\tilde{\chi}^{zz}(0)\delta\tilde{h}^z. \tag{5.5}$$

Using Eq. (4.3), we can calculate the dynamical susceptibility:

$$\tilde{\chi}^{zz}(\omega) = \frac{\delta\tilde{s}^z}{\delta\tilde{h}^z} = \frac{i\Gamma_1\tilde{\chi}^{zz}(0)}{\omega + i\Gamma_1}. \tag{5.6}$$

We can calculate the zero-frequency susceptibility $\tilde{\chi}^{zz}(0)$ by calculating the equilibrium spin state $\boldsymbol{s}^{\mathrm{eq}}$ using Maxwell-Boltzmann statistics:

$$s^{\mathrm{eq}} = \frac{\sum_i s_i e^{-E_i/k_BT}}{\sum_j e^{-E_j/k_BT}} = \frac{1}{2}\left(\frac{e^{h^{\mathrm{eq}}/2k_BT} - e^{-h^{\mathrm{eq}}/2k_BT}}{e^{h^{\mathrm{eq}}/2k_BT} + e^{-h^{\mathrm{eq}}/2k_BT}}\right) = \frac{1}{2}\tanh(h^{\mathrm{eq}}/2k_BT), \tag{5.7}$$

and from Eq. (5.4), the zero-frequency susceptibility is

$$\tilde{\chi}^{zz}(0) = \frac{\partial s^{\mathrm{eq}}}{\partial h^{\mathrm{eq}}} = \frac{1}{4k_BT\cosh^2(h^{\mathrm{eq}}/2k_BT)}. \tag{5.8}$$

Similarly, in the $\hat{x}$ and $\hat{y}$ directions:

$$(\omega + i\Gamma_2)\delta\tilde{s}^x - \frac{i}{\hbar}h^{\mathrm{eq}}\delta\tilde{s}^y = -\frac{i}{\hbar}s^{\mathrm{eq}}\delta\tilde{h}^y + i\Gamma_2\tilde{\chi}^{xx}(0)\delta\tilde{h}^x, \tag{5.9a}$$

$$(\omega + i\Gamma_2)\delta\tilde{s}^y + \frac{i}{\hbar}h^{\mathrm{eq}}\delta\tilde{s}^x = \frac{i}{\hbar}s^{\mathrm{eq}}\delta\tilde{h}^x + i\Gamma_2\tilde{\chi}^{yy}(0)\delta\tilde{h}^y. \tag{5.9b}$$

Defining $\delta s^+ = \delta s^x + i\delta s^y$, we can combine both equations summing Eq. (5.9a) to Eq. (5.9b) multiplied by i:

$$\left(\omega + i\Gamma_2 - \frac{1}{\hbar}h^{\mathrm{eq}}\right)\delta\tilde{s}^+ = \left(i\Gamma_2\tilde{\chi}^{xx}(0) - \frac{1}{\hbar}s^{\mathrm{eq}}\right)\delta\tilde{h}^+, \tag{5.10}$$

where $\delta h^+ = \delta h^x + i\delta h^y$ and by symmetry $\tilde{\chi}^{xx}(0) = \tilde{\chi}^{yy}(0)$. Therefore,

$$\tilde{\chi}^{++}(\omega) = \frac{i\Gamma_2\tilde{\chi}^{xx}(0) - \frac{1}{\hbar}s^{\mathrm{eq}}}{\omega + i\Gamma_2 - \frac{1}{\hbar}h^{\mathrm{eq}}}. \tag{5.11}$$

We can calculate the susceptibilities in all other directions using this result. Note that:

$$\delta\tilde{s}^x = \tilde{\chi}^{xx}\delta\tilde{h}^x + \tilde{\chi}^{xy}\delta\tilde{h}^y, \tag{5.12a}$$

$$\delta\tilde{s}^y = \tilde{\chi}^{yx}\delta\tilde{h}^x + \tilde{\chi}^{yy}\delta\tilde{h}^y. \tag{5.12b}$$

Therefore:

$$\begin{aligned}\delta\tilde{s}^{\pm} &= (\tilde{\chi}^{xx} \pm i\tilde{\chi}^{yx})\,\delta\tilde{h}^{x} + (\tilde{\chi}^{xy} \pm i\tilde{\chi}^{yy})\,\delta\tilde{h}^{y}_{j} \\ &= (\tilde{\chi}^{xx} \pm i\tilde{\chi}^{yx} - i\tilde{\chi}^{xy} \pm \tilde{\chi}^{yy})\,\frac{\delta\tilde{h}^{+}}{2} \\ &+ (\tilde{\chi}^{xx} \pm i\tilde{\chi}^{yx} + i\tilde{\chi}^{xy} \mp \tilde{\chi}^{yy})\,\frac{\delta\tilde{h}^{-}}{2}. \end{aligned} \tag{5.13}$$

From Eq. (5.10) we know that $\tilde{\chi}^{+-}(\omega) = \tilde{\chi}^{-+}(\omega) = 0$, therefore $\tilde{\chi}^{xx}(\omega) = \tilde{\chi}^{yy}(\omega)$ and $\tilde{\chi}^{xy}(\omega) = -\tilde{\chi}^{yx}(\omega)$. And since $\tilde{\chi}^{ab}(-\omega) = [\tilde{\chi}^{ab}(\omega)]^{*}$ for $a, b = x, y, z$, we get the missing susceptibility components:

$$\tilde{\chi}^{yy}(\omega) = \tilde{\chi}^{xx}(\omega) = \frac{1}{2}\left(\tilde{\chi}^{++}(\omega) + [\tilde{\chi}^{++}(-\omega)]^{*}\right), \tag{5.14a}$$

$$\tilde{\chi}^{yx}(\omega) = -\tilde{\chi}^{xy}(\omega) = \frac{1}{2i}\left(\tilde{\chi}^{++}(\omega) - [\tilde{\chi}^{++}(-\omega)]^{*}\right). \tag{5.14b}$$

Note that the flux noise contributions of $\tilde{S}^{xy}(\omega), \tilde{S}^{yx}(\omega)$ will cancel each other out, this follows from the definition of flux noise, Eq. (4.8) and the fact that $\tilde{\chi}^{xy}(\omega) = -\tilde{\chi}^{yx}(\omega)$, therefore the only relevant susceptibilities are $\tilde{\chi}^{zz}(\omega)$ and $\tilde{\chi}^{xx}(\omega)$ ($\tilde{\chi}^{yy}(\omega)$). Note that for zero external magnetic field, $\tilde{\chi}^{zz}_{ij}(\omega) = \tilde{\chi}^{xx}_{ij}(\omega)$. The xx component of the dynamical susceptibility is thus

$$\tilde{\chi}^{xx}(\omega) = \frac{1}{2}\left(\frac{i\Gamma_2\tilde{\chi}^{xx}(0) - \frac{1}{\hbar}s^{\mathrm{eq}}}{\omega + i\Gamma_2 - \frac{1}{\hbar}h^{\mathrm{eq}}} + \frac{i\Gamma_2\tilde{\chi}^{xx}(0) + \frac{1}{\hbar}s^{\mathrm{eq}}}{\omega + i\Gamma_2 + \frac{1}{\hbar}h^{\mathrm{eq}}}\right). \tag{5.15}$$

the zero-frequency susceptibility $\tilde{\chi}^{xx}(0)$ is found by taking the limit of Eq. (5.15) when $\omega \to 0$,

$$\tilde{\chi}^{xx}(0) = \frac{s^{\mathrm{eq}}}{h^{\mathrm{eq}}} = \frac{1}{2h^{\mathrm{eq}}}\tanh(h^{\mathrm{eq}}/2k_BT). \tag{5.16}$$

The spin noise can be found using the fluctuation-dissipation theorem, Eq. (4.5) and the found values of the dynamical susceptibilities, Eqs. (5.6), (5.15). In the current single spin model the

spin noise can be calculated analytically:

$$\tilde{S}^{zz}(\omega) = \frac{2\hbar\omega}{1-e^{-\hbar\omega/k_BT}}\frac{\Gamma_1\tilde{\chi}^{zz}(0)}{\omega^2+\Gamma_1^2}, \tag{5.17a}$$

$$\tilde{S}^{xx}(\omega) = \frac{\hbar\omega\Gamma_2\tilde{\chi}^{xx}(0)}{1-e^{-\hbar\omega/k_BT}}\left[\frac{1}{(\omega-h^{\mathrm{eq}}/\hbar)^2+\Gamma_2^2} + \frac{1}{(\omega+h^{\mathrm{eq}}/\hbar)^2+\Gamma_2^2}\right]. \tag{5.17b}$$

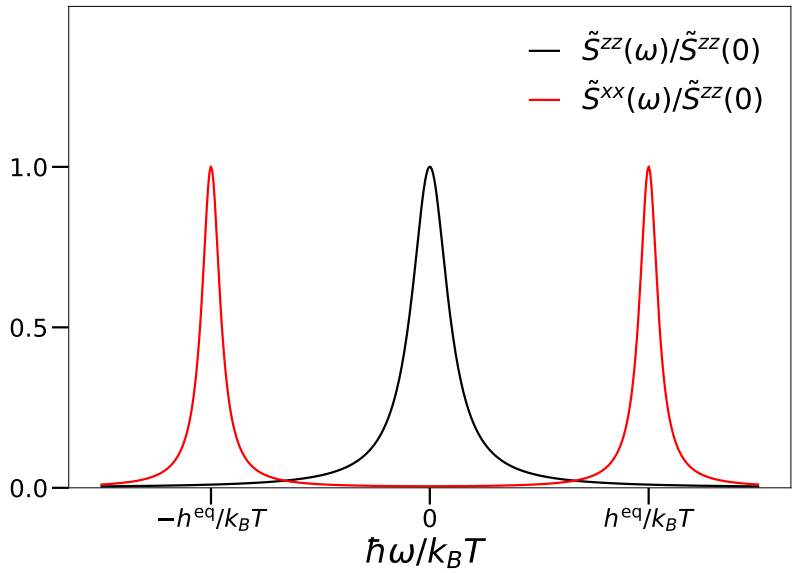

Figure 5.2: ***Spin noise produced by a single spin in a magnetic field h^{eq}.***
Spin fluctuations along $\boldsymbol{h}^{\mathrm{eq}}$ ($\tilde{S}^{zz}(\omega)$) remain peaked at $\omega = 0$. In contrast, spin fluctuations perpendicular to $\boldsymbol{h}^{\mathrm{eq}}$ ($\tilde{S}^{xx}(\omega)$) give rise to "spin precession peaks" centered at $\omega = \pm h^{\mathrm{eq}}/\hbar$. As a result the flux noise contribution due to the component of the flux vector perpendicular to $\boldsymbol{h}^{\mathrm{eq}}$ is expelled from the low frequency range (See Eq. (5.2)). Both contributions are Lorentzian with linewidth set by the corresponding spin decay rate Γ_1, Γ_2. The figure assumes $\Gamma_1 = 2\Gamma_2 = 0.1\ h^{\mathrm{eq}}/\hbar$.

In the presence of an external magnetic field, $\tilde{S}^{zz}(\omega)$ is drastically different from $\tilde{S}^{xx}(\omega)$, as illustrated in Fig. 5.2. From Eq. (5.2) it follows that at each spin location, the flux vector's component parallel to the external field will produce Lorentzian flux noise peaked at $\omega = 0$. In contrast, the component of the flux vector perpendicular to $\boldsymbol{h}^{\mathrm{eq}}$ will produce instead two

Lorentzians peaked at $\omega = \pm h^{\mathrm{eq}}/\hbar = \pm 2\pi(B/1\ \mathrm{G}) \times 2.8\ \mathrm{MHz}$. This shows that even fields of a few Gauss have huge impact on flux noise: They shift the perpendicular flux vector contribution to a much higher frequency range. This effect is the spin analogue of high-frequency charge noise produced by quantum coherent TLSs in amorphous materials [71]. The magnetic external field will also have an effect on the amplitude of the zero-frequency susceptibility and therefore on the amplitude of noise. This dependence is very weak for small fields h^{eq} since $\tilde{\chi}^{xx}(0) = \tilde{\chi}^{zz}(0) \approx 1/4k_BT$ in this limit. For large fields $h^{\mathrm{eq}} \gg k_BT$, $\tilde{\chi}^{xx}(0) \propto 1/h^{\mathrm{eq}}$ and $\tilde{\chi}^{zz}(0) \propto e^{-h^{\mathrm{eq}}}$, the zero-frequency susceptibility thus shows a strong dependence on large external fields.

5.3 Impact of Cross Relaxation

5.3.1 Cross Relaxation

Cross relaxation, in the context of this dissertation, refers to the phenomenon where impurity spins relax due to phonon-induced transitions of amorphous TLSs. These systems are typically defects or non-crystalline structures within the material that can absorb and emit energy at quantum scales and can be modeled by a double well potential. The impurity spin couples to the TLS either through spin-orbit or hyperfine interaction, both of which are modulated by the TLS transition. In environments where such amorphous TLSs are present, spins can exchange energy with these defects, leading to relaxation processes that differ significantly from those observed in more orderly crystalline structures.

The cross-relaxation rate, whereby an impurity spin $\boldsymbol{s}_j$ flips simultaneously with an amorphous TLS switch (red arrow in Fig. 5.4), is given by [6, 63]

$$\Gamma_{1,j} = \Gamma_c e^{-\lambda_j}, \tag{5.18}$$

where Γ_c is a cut-off for $\Gamma_{1,j}$, and λ_j is a random variable uniformly distributed in the interval $[0, \lambda_{\max}]$; it models the barrier for TLS switch. Since the majority of these processes occur for TLSs with energy splitting of the order of k_BT, cross relaxation is independent of magnetic field

when $g\mu_B B < k_B T$ [6]. Such a model is described by the probability density

$$p(\Gamma) = \frac{1}{\lambda_{\max}} \frac{1}{\left|\frac{d\Gamma}{d\lambda}\right|} = \frac{1}{\lambda_{\max}} \frac{1}{\Gamma}, \tag{5.19}$$

for $\Gamma_{\min} < \Gamma < \Gamma_{\max}$, and zero otherwise, where $\Gamma_{\min} = \Gamma_c e^{-\lambda_{\max}}$ and $\Gamma_{\max} = \Gamma_c$.

5.3.2 *Disorder in a Spin Ensemble:* $1/f$ *Noise*

Let's now consider an ensemble of multiple spins, we assume that independent spin flips dominate $\omega > 0$ noise, so that $\tilde{S}_{jk}(\omega) \ll \tilde{S}_{jj}(\omega)$ when $j \neq k$, i.e., interactions between spins are not relevant, under this consideration, the total flux noise produced by this system is simply the sum of the flux noise generated by each spin, Eq (5.2). We introduce disorder in the system assuming each spin decays with a relaxation rate $\Gamma_{1,j}$ given by cross-relaxation as described earlier, Eq. (5.18). The disorder-averaged parallel spin noise is

$$\begin{aligned}
\tilde{S}^{zz}_{\text{avg}}(\omega) &= \int_{\Gamma_{\min}}^{\Gamma_{\max}} \tilde{S}^{zz}(\omega) p(\Gamma) d\Gamma = \frac{2\hbar\omega}{1 - e^{-\hbar\omega/k_B T}} \frac{\tilde{\chi}^{zz}(0)}{\lambda_{\max}} \int_{\Gamma_{\min}}^{\Gamma_{\max}} \frac{d\Gamma}{\omega^2 + \Gamma^2} \\
&= \frac{2\hbar\omega}{1 - e^{-\hbar\omega/k_B T}} \frac{\tilde{\chi}^{zz}(0)}{\omega\lambda_{\max}} \left[\arctan\left(\frac{\Gamma_{\max}}{\omega}\right) - \arctan\left(\frac{\Gamma_{\min}}{\omega}\right) \right] \\
&\approx \frac{k_B T \pi \tilde{\chi}^{zz}(0)}{\lambda_{\max}} \frac{1}{\omega},
\end{aligned} \tag{5.20}$$

where in the last line we assumed $\Gamma_{\min} \ll \omega \ll \Gamma_{\max}$ and $\hbar\omega \ll k_B T$. While a single spin produces Lorentzian noise, a system of disordered spins with a wide distribution of relaxation rates Γ_1 can give rise to $1/f$ noise in a large interval of frequencies [1, 6, 63], this can be seen in Fig. 5.3. This provides a possible explanation for the mechanism producing flux noise measured in Al devices as in Fig. 3.3a. Note that when $\omega \gg \Gamma_{\max}$, $\tilde{S}^{zz}_{\text{avg}}(\omega) \propto \frac{1}{\omega^2}$ and for very low frequencies $\omega \ll \Gamma_{\min}$, $\tilde{S}^{zz}_{\text{avg}}(\omega)$ has a lorentzian behaviour. Similarly, if we assume that spin decoherence is dominated by spin relaxation, $\Gamma_2 \approx \Gamma_1/2$, the disorder-averaged of the spin noise perpendicular component is

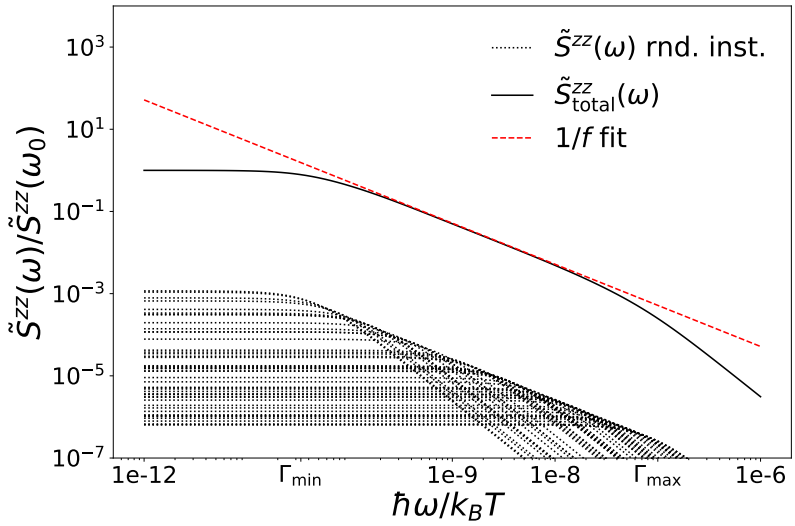

Figure 5.3: $1/f$ ***flux noise from a wide distribution of spins.***
Spin noise $\tilde{S}^{zz}(\omega)$ calculations for a random ensemble of spins. The dotted lines show each individual instance of $\tilde{S}^{zz}(\omega)$ for a particular random relaxation rate $\Gamma_{i,j}$ from Γ_{min} to Γ_{max} according to Eq. (5.18), the solid line represents the sum of all instances. The red dotted line is the $1/f$ fit for $\Gamma_{\text{min}} \ll \omega \ll \Gamma_{\text{max}}$, Eq. (5.20). 5000 instances were considered in the sum, only 50 are shown. $\hbar\omega_0/k_BT = 10^{-12}$, $\hbar\Gamma_{\text{max}}/k_BT = 10^{-7}$, $\lambda_{\text{max}} = 8$.

$$
\begin{aligned}
\tilde{S}^{xx}_{\text{avg}}(\omega) &= \int_{\Gamma_{\text{min}}/2}^{\Gamma_{\text{max}}/2} \tilde{S}^{xx}(\omega) p(\Gamma) d\Gamma \\
&= \frac{\hbar\omega}{1-e^{-\hbar\omega/k_BT}} \frac{\tilde{\chi}^{xx}(0)}{\lambda_{\text{max}}} \int_{\Gamma_{\text{min}}/2}^{\Gamma_{\text{max}}/2} d\Gamma \left[\frac{1}{(\omega - h^{\text{eq}}/\hbar)^2 + \Gamma^2} + \frac{1}{(\omega + h^{\text{eq}}/\hbar)^2 + \Gamma^2} \right] \\
&= \frac{\hbar\omega}{1-e^{-\hbar\omega/k_BT}} \frac{\tilde{\chi}^{xx}(0)}{\lambda_{\text{max}}} \left\{ \frac{1}{\omega - h^{\text{eq}}/\hbar} \left[\arctan\left(\frac{\Gamma_{\text{max}}/2}{\omega - h^{\text{eq}}/\hbar} \right) - \arctan\left(\frac{\Gamma_{\text{min}}/2}{\omega - h^{\text{eq}}/\hbar} \right) \right] \right. \\
&+ \left. \frac{1}{\omega + h^{\text{eq}}/\hbar} \left[\arctan\left(\frac{\Gamma_{\text{max}}/2}{\omega + h^{\text{eq}}/\hbar} \right) - \arctan\left(\frac{\Gamma_{\text{min}}/2}{\omega + h^{\text{eq}}/\hbar} \right) \right] \right\}. \qquad (5.21)
\end{aligned}
$$

From this result we see that $\tilde{S}^{xx}_{\text{avg}}(\omega) \propto 1/|\omega \pm h^{\text{eq}}/\hbar|$ for $\Gamma_{\text{min}} \ll |\omega \pm h^{\text{eq}}/\hbar| \ll \Gamma_{\text{max}}$, therefore, in a spin system dominated by spin relaxation, we can expect spin noise $\tilde{S}^{xx}_{\text{avg}}(\omega)$ to behave similarly to $\tilde{S}^{zz}_{\text{avg}}(\omega \simeq 0)$ at frequencies $\omega = \pm h^{\text{eq}}/\hbar$. In systems where $\Gamma_2 \gg \Gamma_1/2$ we can expect this

contribution to be less relevant.

5.4 Impact of Direct Spin Relaxation

5.4.1 *Direct Relaxation*

Direct relaxation involves the process by which spins return to thermal equilibrium with their surrounding lattice environment. This relaxation is characterized by the energy transfer from the excited spins to the lattice, typically mediated by phononic interactions in the material. The direct relaxation rate, corresponding to a spin-flip with the amorphous TLS state unchanged (blue arrow in Fig. 5.4) is given by

$$\Gamma_{1,j} = \Gamma_d (k_B T)(h^{\mathrm{eq}})^n, \tag{5.22}$$

independent of the spin $\boldsymbol{s}_j$. The rate scales linearly in T because they are proportional to the phonon occupation at the Zeeman frequency in the high temperature limit; it also scales as $(h^{\mathrm{eq}})^n$ because the direct mechanism requires the breaking of time-reversal symmetry and therefore vanishes at zero magnetic field. The exponent n depends on the interaction mediating the relaxation mechanism, $n = 2$ for hyperfine interaction and $n = 4$ for spin-orbit coupling [72, 73].

5.4.2 *Reduced Disorder: $1/f$ to Lorentzian Noise*

We propose the following relaxation rates for a spin $\boldsymbol{s}_j$ placed on the surface or interface of a SC wire,

$$\Gamma_{1,j} = \Gamma_c e^{-\lambda_j} + \Gamma_h. \tag{5.23}$$

We define $\Gamma_h \equiv \Gamma_d (k_B T)(h^{\mathrm{eq}})^n$ as the direct relaxation contribution to the spin relaxation. The $\Gamma_{1,j}$ are distributed according to probability density $p(\Gamma) = 1/(\lambda_{\max} |\frac{d\Gamma}{d\lambda}|)$, this expression accounts for both cross and direct spin relaxation. This leads to the disorder-averaged single spin noise,

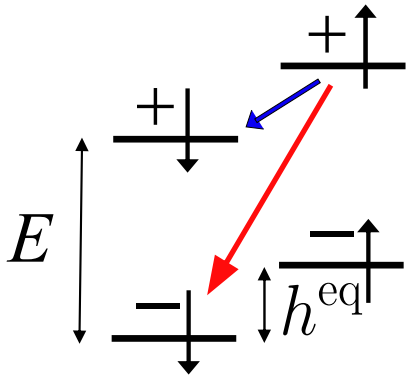

Figure 5.4: ***Energy level structure for a spin coupled to an amorphous TLS.***
4 level system of amorphous TLS coupled to a spin. E is the energy difference between the amorphous TLS's eigenstates ($\pm$) modeled by a double well potential coupled to the spin ($\uparrow$ / $\downarrow$). The red (blue) arrow illustrates cross (direct) relaxation, $\Gamma_{\pm,\uparrow/\downarrow} \to \Gamma_{\mp,\downarrow/\uparrow}$ ($\Gamma_{\pm,\uparrow/\downarrow} \to \Gamma_{\pm,\downarrow/\uparrow}$).

$$\begin{aligned}
\tilde{S}^{zz}_{\rm avg}(\omega) &= \int_{\Gamma_{\rm min}}^{\Gamma_{\rm max}} \tilde{S}^{zz}(\omega) p(\Gamma) d\Gamma = \frac{2\hbar\omega\tilde{\chi}^{zz}(0)}{1-e^{-\hbar\omega/k_BT}} \frac{1}{\lambda_{\rm max}} \int_{\Gamma_{\rm min}}^{\Gamma_{\rm max}} \frac{1+\frac{\Gamma_h}{\Gamma-\Gamma_h}}{\omega^2+\Gamma^2} d\Gamma \\
&= \frac{2\hbar\omega\tilde{\chi}^{zz}(0)}{1-e^{-\hbar\omega/k_BT}} \left\{ \frac{1}{\lambda_{\rm max}} \left(\frac{\omega^2}{\omega^2+\Gamma_h^2} \right) \frac{\arctan(\Gamma_{\rm max}/\omega) - \arctan(\Gamma_{\rm min}/\omega)}{\omega} \right. \\
&+ \left. \left[1 - \frac{1}{2\lambda_{\rm max}} \log\left(\frac{\Gamma_{\rm max}^2+\omega^2}{\Gamma_{\rm min}^2+\omega^2} \right) \right] \frac{\Gamma_h}{\omega^2+\Gamma_h^2} \right\}, \qquad (5.24)
\end{aligned}$$

where the minimum and maximum rates are $\Gamma_{\rm min} = \Gamma_0 e^{-\lambda_{\rm max}} + \Gamma_h$ and $\Gamma_{\rm max} = \Gamma_0 + \Gamma_h$.

When $h^{\rm eq} = 0$, $\Gamma_h = 0$ and the first term in the curly bracket of Eq. (5.24) gives rise to $1/|\omega|$ noise for a wide range of frequencies $\Gamma_{\rm min} \ll |\omega| \ll \Gamma_{\rm max}$. As $h^{\rm eq}$ is increased from zero, there will be a range of frequencies satisfying $|\omega| < \Gamma_h \approx \Gamma_{\rm min}$. In this range the $1/|\omega|$ contribution to flux noise is suppressed, and the second term in the curly bracket of Eq. (5.24) becomes important, with the square bracket approximately independent of ω. As $h^{\rm eq}$ increases further $\Gamma_{\rm min}$ gets close to $\Gamma_{\rm max}$ and the low frequency noise is converted into a simple "reduced disorder" Lorentzian, centered at $\omega = 0$ with width Γ_h.

Figure 5.5 shows the predicted transition from $1/\omega$ to Lorentzian flux noise with increasing magnetic field. The behavior is in qualitative agreement to recent experiments in Al devices (Fig.

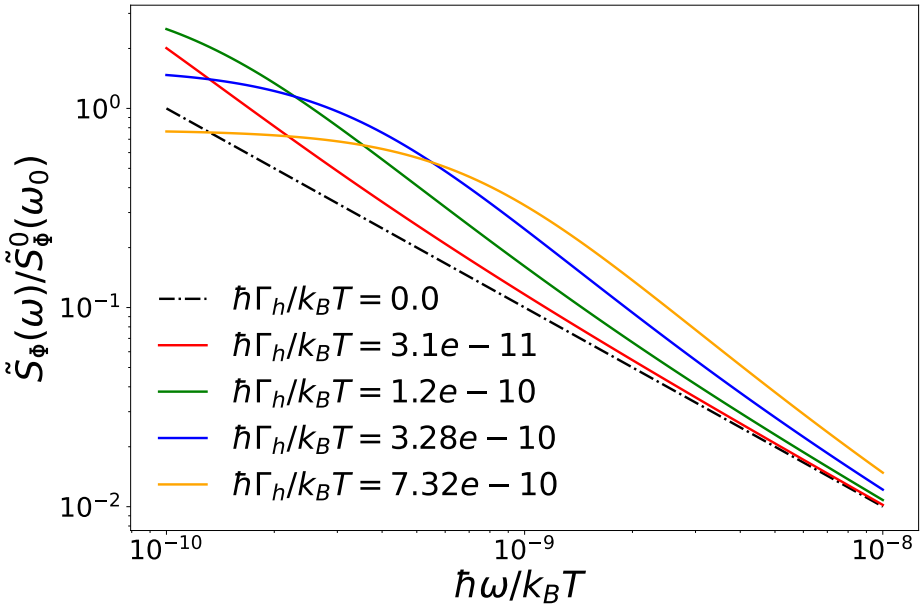

Figure 5.5: $1/f$ ***to lorentzian flux noise due to a magnetic field.***
Effect of external magnetic field $\boldsymbol{h}^{\rm eq}$ *on flux noise with* $\boldsymbol{F}_j = \boldsymbol{F} \parallel \boldsymbol{h}^{\rm eq}$. *The spin relaxation rates are assumed to be distributed according to Eq. (5.23), with exponent* $n = 4$ *representing direct phonon emission due to spin-orbit admixture. Flux noise transitions from* $1/\omega$ *"disorder" noise to an "undisordered" Lorentzian with increasing* $h^{\rm eq}$. *The noise is normalized by* $\tilde{S}^0_\Phi(\omega_0)$, *its value at* $h^{\rm eq} = 0$ *and* $\hbar\omega_0/k_BT = 10^{-10}$. *Parameters used in the calculation:* $\hbar\Gamma_c/k_BT = 1, \hbar\Gamma_d = 5 \times 10^{-6}(k_BT)^{-4}, \lambda_{\rm max} = 30$ *and* $h^{\rm eq}/k_BT = 0 - 0.11$.

3.4a). Our Eqs. (5.2) and (5.24) can explain the experimental data if we assume $\lambda_{\rm max} = 10 - 30$ and spin areal density $3 - 8 \times 10^{16}/\mathrm{m}^2$.

The spin precession peaks at $\omega = \pm h^{\rm eq}/\hbar$, the ones that occur due to the nonzero components of $\boldsymbol{F}_j \perp \boldsymbol{h}^{\rm eq}$, may also broaden due to disorder. If these are dominated by spin energy relaxation, we get $\Gamma_{2,j} \approx \frac{1}{2}\Gamma_{1,j}$ and the peaks transition from $\propto 1/|\omega \pm h^{\rm eq}/\hbar|$ at low $h^{\rm eq}$ to Lorentzians centered at $\pm h^{\rm eq}/\hbar$ with width Γ_h at higher $h^{\rm eq}$. Measuring the shape of these spin precession peaks will yield information about the distribution of spin decoherence rates $\Gamma_{2,j}$.

5.5 Conclusions

This chapter proposes a spin noise model to account for flux noise observations in SC Al devices. This model suggests that finite frequency fluctuations are primarily influenced by the interaction between each impurity spin and the vibrational modes of the lattice, which consists of amorphous TLSs and phonons, this corresponds to the general spin dissipation model proposed in chapter 4 with no spin-spin interactions. In this regime, spins can be treated independently and analytic results for flux noise can be calculated.

By accounting for cross relaxation between spins and amorphous TLSs, an analytic expression for flux noise is derived, the results show that $1/f$ flux noise measured in Al devices can be explained using this model. To explore the impact of external magnetic fields, we extend this theory to include direct relaxation, the result shows a shift from $1/f$ flux noise at $B = 0$ to Lorentzian noise in the frequency range where direct spin relaxation by phonon emission is more significant than cross relaxation due to amorphous TLSs. This transition mirrors recent experimental observations.

CHAPTER 6

Flux Noise Results in the General Spin Dissipation Theory

This chapter is an expanded version of sections V-X in publication [1].

6.1 Introduction

In this chapter we present results using the general theory described in chapter 4. In section 6.2 we present general results for the dynamical susceptibilities and flux noise in the paramagnetic case, these expressions are later used to get numerical results. Section 6.3 contains analytic results of the general theory in a homogeneous and infinite magnet, we also propose a phenomenological expression for flux noise based on these results. Section 6.4 presents results for a confined magnet, showing how confinement and disorder impact flux noise compared to the homogeneous case. Section 6.5 presents the conclusions.

6.2 General Results

6.2.1 Linear Equation of Motion

To calculate general expressions of dynamical susceptibility and flux noise we start by linearizing the equation of motion from our spin dissipation model. For small deviations from equilibrium, $\boldsymbol{h}_i = \boldsymbol{h}_i^{\mathrm{eq}} + \delta\boldsymbol{h}_i(t)$, and $\boldsymbol{s}_i = \boldsymbol{s}_i^{\mathrm{eq}} + \delta\boldsymbol{s}_i(t)$, where both $\delta\boldsymbol{h}_i(t)$ and $\delta\boldsymbol{s}_i(t)$ are small time-dependent perturbations. We plug these into the general equation of motion (4.20), drop non-linear terms

such as $(\delta \boldsymbol{s}_i)^2$, $(\delta \boldsymbol{h}_i(t))^2$, and use Eq. (4.23) to simplify:

$$\begin{aligned}\frac{d}{dt}(\delta \boldsymbol{s}_i) &= \frac{1}{\hbar}\boldsymbol{s}_i^{\rm eq} \times \left\{ (\delta \boldsymbol{h}_i) + \sum_j x_j J_{ij} (\delta \boldsymbol{s}_j) - 4k_B T \left[1 + \frac{4}{3}(s_i^{\rm eq})^2\right](\delta \boldsymbol{s}_i) - \frac{32}{3} k_B T [\boldsymbol{s}_i^{\rm eq} \cdot (\delta \boldsymbol{s}_i)] \boldsymbol{s}_i^{\rm eq} \right\} \\ &- \sum_j D_{ij} x_j \left\{ (\delta \boldsymbol{h}_j) + \sum_k x_k J_{jk} (\delta \boldsymbol{s}_k) - 4k_B T \left[1 + \frac{4}{3}(s_j^{\rm eq})^2\right](\delta \boldsymbol{s}_j) - \frac{32}{3} k_B T [\boldsymbol{s}_j^{\rm eq} \cdot (\delta \boldsymbol{s}_j)] \boldsymbol{s}_j^{\rm eq} \right\} \\ &+ \frac{1}{\hbar}(\delta \boldsymbol{s}_i) \times \boldsymbol{H}_i^{\rm eq} - \Gamma_i (\delta \boldsymbol{s}_i) + \Gamma_i \sum_j \tilde{\chi}_{ij}(0) (\delta \boldsymbol{h}_j). \end{aligned} \tag{6.1}$$

Assume $\boldsymbol{h}_i^{\rm eq} = h_i^{\rm eq} \hat{\boldsymbol{z}}$ (in-plane magnetic field), $\boldsymbol{s}_i^{\rm eq} = s_i^{\rm eq} \hat{\boldsymbol{z}}$ and thus $\boldsymbol{H}_i^{\rm eq} = H_i^{\rm eq} \hat{\boldsymbol{z}}$ and break this down into two equations, one for δs_i^z obtained by dot product with $\hat{\boldsymbol{z}}$ on both sides of Eq. (6.1), and the other for $\delta s_i^+ = \delta s_i^x + i \delta s_i^y$ obtained by dot product with $(\hat{\boldsymbol{x}} + i\hat{\boldsymbol{y}})$. Taking the time Fourier transform we get two decoupled equations:

$$(\omega \mathbf{I} - \mathbf{P}) \cdot \delta \tilde{\boldsymbol{s}}^z = i\,(\boldsymbol{\Gamma} \cdot \tilde{\boldsymbol{\chi}}_0 - \mathbf{D}) \cdot \delta \tilde{\boldsymbol{h}}^z, \tag{6.2a}$$

$$(\omega \mathbf{I} - \mathbf{M}) \cdot \delta \tilde{\boldsymbol{s}}^+ = \left[i\,(\boldsymbol{\Gamma} \cdot \tilde{\boldsymbol{\chi}}_0 - \mathbf{D}) - \frac{1}{\hbar}\mathbf{s}^{\rm eq} \right] \cdot \delta \tilde{\boldsymbol{h}}^+, \tag{6.2b}$$

where $\delta \tilde{\boldsymbol{s}}^z, \delta \tilde{\boldsymbol{s}}^+$ and $\delta \tilde{\boldsymbol{h}}^z, \delta \tilde{\boldsymbol{h}}^+$ are N-component column vectors, and $\mathbf{I}, \boldsymbol{\Gamma}, \tilde{\boldsymbol{\chi}}_0, \mathbf{D}, \mathbf{s}^{\rm eq}$ are $N \times N$ matrices. They are defined by $[\mathbf{I}]_{ij} = x_i \delta_{ij}$, $[\boldsymbol{\Gamma}]_{ij} = x_i \Gamma_i \delta_{ij}$, $[\tilde{\boldsymbol{\chi}}_0]_{ij} = \tilde{\chi}_{ij}(0)$, $[\mathbf{D}]_{ij} = x_i x_j D_{ij}$, and $[\mathbf{s}^{\rm eq}]_{ij} = x_i s_i^{\rm eq} \delta_{ij}$.

The matrices $\mathbf{P}$ and $\mathbf{M}$ are the *paramagnon* and *magnon* matrices, respectively. They are given by

$$\mathbf{P} = -i \left\{ \boldsymbol{\Gamma} + \mathbf{D} \cdot \mathbf{J} - 4k_B T \mathbf{D} \cdot \left[\mathbf{I} + 4\,(\mathbf{s}^{\rm eq})^2 \right] \right\}, \tag{6.3a}$$

$$\begin{aligned}\mathbf{M} &= -i \left\{ \boldsymbol{\Gamma} + \mathbf{D} \cdot \mathbf{J} - 4k_B T \mathbf{D} \cdot \left[\mathbf{I} + \frac{4}{3}\,(\mathbf{s}^{\rm eq})^2 \right] \right\} \\ &+ \tfrac{1}{\hbar} \left\{ \mathbf{H}^{\rm eq} - \mathbf{s}^{\rm eq} \cdot \left[\mathbf{J} - 4k_B T \left(\mathbf{I} + \frac{4}{3}\,(\mathbf{s}^{\rm eq})^2 \right) \right] \right\}, \end{aligned} \tag{6.3b}$$

where $[\mathbf{J}]_{ij} = x_i x_j J_{ij}$, and $[\mathbf{H}^{\rm eq}]_{ij} = H_i^{\rm eq} \delta_{ij}$.

The eigenvalues of $\mathbf{P}$ and $\mathbf{M}$ are paramagnon and magnon frequencies, respectively. While

paramagnons cause spin fluctuations along $\boldsymbol{s}_i^{\rm eq}$, the magnons cause fluctuations perpendicular to $\boldsymbol{s}_i^{\rm eq}$. In the paramagnetic phase ($T > T_c^{\rm mag}$) with zero external fields, $\mathbf{s}^{\rm eq} = \mathbf{H}^{\rm eq} = \mathbf{0}$ and the matrices $\mathbf{P}$ and $\mathbf{M}$ become identical, signaling the presence of isotropic spin fluctuations (paramagnons are three-fold degenerate). Our discussion will focus on the paramagnetic phase where $T > T_c^{\rm mag}$ and zero external magnetic field, where $\mathbf{P} = \mathbf{M}$. We thus look into the solution to Eq. (6.2a) and the spectrum of $\mathbf{P}$.

6.2.2 *Dynamical Susceptibilities*

Diagonalize $\mathbf{P}$ with a transformation $\mathbf{U}$ such that

$$\mathbf{U}^{-1} \cdot \mathbf{P} \cdot \mathbf{U} = \mathbf{P}_d = -i \sum_m \gamma_m \hat{\boldsymbol{e}}_m \otimes \hat{\boldsymbol{e}}_m^T, \tag{6.4}$$

where m labels the paramagnon mode with frequency $-i\gamma_m$, with $\hat{\boldsymbol{e}}_m$ unit column vectors, $\hat{\boldsymbol{e}}_m^T = (0, \ldots, 0, 1, 0, \ldots, 0)$, etc. All elements of $\mathbf{P}$ are pure complex, therefore the $\mathbf{U}$ and $\mathbf{U}^{-1}$ can be chosen to have real elements. Take the complex conjugate of Eq. (6.4) and use $\mathbf{P}^* = -\mathbf{P}$ to see that $\gamma_m^* = \gamma_m$.

Apply $\mathbf{U}^{-1}$ on both sides of Eq. (6.2a),

$$(\omega - \mathbf{P}_d) \cdot \mathbf{U}^{-1} \cdot \delta\tilde{\boldsymbol{s}}^z = i\mathbf{U}^{-1} \cdot (\boldsymbol{\Gamma} \cdot \tilde{\boldsymbol{\chi}}_0 - \mathbf{D}) \cdot \delta\tilde{\boldsymbol{h}}^z, \tag{6.5}$$

and invert the diagonal matrix to get an exact expression for the susceptibility:

$$(\delta\tilde{\boldsymbol{s}}^z) = i \sum_m \mathbf{U} \cdot \frac{\hat{\boldsymbol{e}}_m \otimes \hat{\boldsymbol{e}}_m^T}{\omega + i\gamma_m} \cdot \mathbf{U}^{-1} \cdot (\boldsymbol{\Gamma} \cdot \tilde{\boldsymbol{\chi}}_0 - \mathbf{D}) \cdot \delta\tilde{\boldsymbol{h}}^z. \tag{6.6}$$

Transformation (6.4) implies that column vector $\boldsymbol{v}_m = \mathbf{U} \cdot \hat{\boldsymbol{e}}_m$ is the right eigenvector of $\mathbf{P}$ associated to the eigenvalue $-i\gamma_m$. Similarly, the line vector $\boldsymbol{v}_m^{-1} = \hat{\boldsymbol{e}}_m^T \cdot \mathbf{U}^{-1}$ is the left eigenvector of $\mathbf{P}$ associated to the same eigenvalue. We have $\boldsymbol{v}_m^{-1} \cdot \boldsymbol{v}_{m'} = \delta_{mm'}$, but the set $\{\boldsymbol{v}_m\}$ is not mutually orthogonal because $[\mathbf{P}, \mathbf{P}^\dagger] \neq \mathbf{0}$ ($\mathbf{P}$ is not normal).

Using these results, Eqs. (6.2a) and (6.6) imply the following exact expression for the dynam-

ical susceptibility in the z direction:

$$\tilde{\boldsymbol{\chi}}^{zz}(\omega) = i\left(\omega\mathbf{I}-\mathbf{P}\right)^{-1}\cdot\left(\boldsymbol{\Gamma}\cdot\tilde{\boldsymbol{\chi}}_0-\mathbf{D}\right) \tag{6.7a}$$

$$= i\sum_m \frac{\boldsymbol{v}_m\otimes\left[\boldsymbol{v}_m^{-1}\cdot\left(\boldsymbol{\Gamma}\cdot\tilde{\boldsymbol{\chi}}_0-\mathbf{D}\right)\right]}{\omega+i\gamma_m}, \tag{6.7b}$$

The dynamical susceptibility has poles at the paramagnon frequencies $\omega=-i\gamma_m$, and these contribute to dissipation and noise. The paramagnons are said to be purely dissipative because γ_m is real, leading to $e^{-i\omega t}=e^{-\gamma_m t}$ for the decay of the spin excitations. For $T>T_c^{\rm mag}$ we have $\gamma_m\geq 0$ because the paramagnetic phase is stable.

Conservation of total spin follows from $\mathbf{1}^T\cdot\mathbf{D}=\mathbf{0}^T$, where $\mathbf{1}(\mathbf{0})$ is the column vector with all N components equal to $1(0)$. All contributions to the paramagnon matrix (6.3a) have $\mathbf{D}$ on the left, so it follows that the $m=0$ mode defined by $\hat{\boldsymbol{v}}_0^{-1}=\mathbf{1}^T/\sqrt{N}$ is a left eigenvector of $\mathbf{P}$ associated to $\gamma_0=0$. This is true for general J_{ij}. Because $\boldsymbol{v}_0^{-1}\cdot\mathbf{D}=\mathbf{0}^T$, $m=0$ does not contribute to the sum in the dynamical susceptibility Eq. (6.7b). This occurs as a direct consequence of the conservation law $\frac{d}{dt}(\mathbf{1}^T\cdot\delta\boldsymbol{s}^z)=\mathbf{0}$, so we say $m=0$ is the nondissipative Goldstone paramagnon.

At high frequency $\omega\gg \mathrm{Max}_m\{\gamma_m\}$, Eq. (6.7b) leads to

$$\tilde{\boldsymbol{\chi}}^{zz}(\omega)\approx\frac{i\left(\boldsymbol{\Gamma}\cdot\tilde{\boldsymbol{\chi}}_0-\mathbf{D}\right)}{\omega}, \tag{6.8}$$

because $\sum_m \boldsymbol{v}_m\otimes\boldsymbol{v}_m^{-1}=\mathbf{I}$. As Eq. (4.20) has an upper frequency cut-off Ω_c, Eq. (6.8) should be taken as an upper bound on the modulus of the susceptibility.

Now consider the opposite limit, $\omega\to 0$. Setting $\omega=0$ in Eq. (6.7a) leads to $(\mathbf{P}+i\boldsymbol{\Gamma})\cdot\tilde{\boldsymbol{\chi}}_0=i\mathbf{D}$, and using Eq. (6.3a) we get

$$\tilde{\boldsymbol{\chi}}^{zz}(\omega=0)=\left(4k_BT\mathbf{I}-\mathbf{J}\right)^{-1}. \tag{6.9}$$

This is the generalized Curie-Weiss susceptibility for a nonhomogeneous spin system.

6.2.3 *Flux Noise and Paramagnon Density*

The explicit expression for flux noise can be calculated using the susceptibility, Eq. (6.7b); the fluctuation-dissipation theorem, Eq. (4.5); and the definition of flux noise, Eq. (4.8). When $T>T_c^{mag}$ and external magnetic field $\boldsymbol{h}^{\rm eq}=0$, the flux noise due to interacting spins is given by

the simple expression

$$\tilde{S}_\Phi(\omega) = \frac{2\hbar\omega}{1 - e^{-\frac{\hbar\omega}{k_B T}}} \sum_{m,a} \frac{\boldsymbol{F}^{aT} \cdot \boldsymbol{v}_m \left[\boldsymbol{v}_m^{-1} \cdot (\boldsymbol{\Gamma} \cdot \tilde{\boldsymbol{\chi}}_0 - \mathbf{D}) \cdot \boldsymbol{F}^a\right]}{\omega^2 + \gamma_m^2}, \tag{6.10}$$

where $\boldsymbol{F}^{aT} = (F^a(\boldsymbol{R}_0), \ldots, F^a(\boldsymbol{R}_{N-1}))$ represents the a-component of the flux vector for all spins. A convenient way to interpret this expression is to write it in terms of a density of Lorentzian contributions

$$\tilde{S}_\Phi(\omega) = \frac{2\pi\hbar\omega}{1 - e^{-\frac{\hbar\omega}{k_B T}}} \int_{-\infty}^{\infty} d\gamma \frac{\gamma/\pi}{\omega^2 + \gamma^2} \rho_\Phi(\gamma), \tag{6.11}$$

where $\rho_\Phi(\gamma)$ is the *paramagnon flux density*, defined as

$$\rho_\Phi(\gamma) = \frac{1}{\gamma} \sum_{m,a} (\boldsymbol{F}^{aT} \cdot \boldsymbol{v}_m) \left[\boldsymbol{v}_m^{-1} \cdot (\boldsymbol{\Gamma} \cdot \tilde{\boldsymbol{\chi}}_0 - \mathbf{D}) \cdot \boldsymbol{F}^a\right] \delta(\gamma - \gamma_m), \tag{6.12}$$

where $\delta(x)$ is the Dirac delta function.

In the high frequency limit $\omega \gg \mathrm{Max}_m\{\gamma_m\}$ Eq. (6.10) implies

$$\tilde{S}_\Phi(\omega) = \frac{2\hbar}{1 - e^{-\frac{\hbar\omega}{k_B T}}} \frac{1}{\omega} \sum_a \boldsymbol{F}^{aT} \cdot (\boldsymbol{\Gamma} \cdot \tilde{\boldsymbol{\chi}}_0 - \mathbf{D}) \cdot \boldsymbol{F}^a. \tag{6.13}$$

Since Eq. (4.20) has an upper frequency cut-off Ω_c, the actual $\tilde{S}_\Phi(\omega)$ is expected to be less than Eq. (6.13) at $\omega > \Omega_c$. In this regime Eq. (6.13) provides an upper bound on flux noise.

6.3 Homogeneous Magnet in the Paramagnetic Phase

Before presenting numerical results in the general case, it is illustrative to spend some time discussing a relevant simple case. When the spin system is translation-invariant, our method yields exact analytic expressions for the spin noise for general D_{ij} using spatial Fourier transforms. This is the case when the system has periodic b.c., and the vacancies are organized in a regular sublattice of the full virtual lattice, we also assume the system is in the paramagnetic phase and is under no external magnetic field so $\boldsymbol{s}_i^{\mathrm{eq}} = 0$ everywhere. We may take spatial averages over parameters x_i, D_{ij}, J_{ij} and γ_1 in order to force its equation of motion to become exactly solvable.

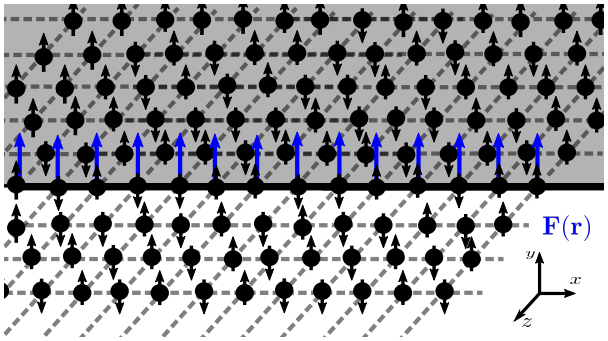

Figure 6.1: ***Infinite plane of spins.***
Homogeneous magnet with flux vector $\boldsymbol{F}$ *described by the single edge model. The upper infinite semi-plane represents the wire, while the lower semi-plane represents the surrounding materials.*

In this case the resulting analytic solution is called homogeneous approximation (HA).

6.3.1 Susceptibility and Spin Noise

In the paramagnetic phase ($T > T_c^{\mathrm{mag}}$), the equation of motion, Eq. (6.1), becomes

$$\begin{aligned} \frac{d}{dt}(\delta s_i^a) &= -\sum_j D_{ij} x_j \left[(\delta h_j^a) + \sum_k x_k J_{jk} (\delta s_k^a) - 4 k_B T (\delta s_j^a) \right] \\ &- \Gamma_i (\delta s_i^a) + \Gamma_i \sum_j \tilde{\chi}_{ij}(0) (\delta h_j^a), \end{aligned} \tag{6.14}$$

for $a = x, y, z$. Replace x_i, D_{ij}, Γ_i by their average values:

$$\bar{x} = \sigma = \frac{1}{N}\sum_i x_i, \tag{6.15a}$$

$$\bar{D}_{\boldsymbol{v}} = \frac{1}{N\sigma^2}\sum_i x_i x_{i+\boldsymbol{v}} D_{i,i+\boldsymbol{v}}, \tag{6.15b}$$

$$\bar{J}_{\boldsymbol{v}} = \frac{1}{N\sigma^2}\sum_i x_i x_{i+\boldsymbol{v}} J_{i,i+\boldsymbol{v}}, \tag{6.15c}$$

$$\bar{\Gamma} = \frac{1}{N\sigma}\sum_i x_i \Gamma_i, \tag{6.15d}$$

$$\bar{\chi}_{\boldsymbol{v}}(0) = \frac{1}{N\sigma^2}\sum_i \tilde{\chi}_{i,i+\boldsymbol{v}}(0). \tag{6.15e}$$

Equation (6.14) becomes

$$\begin{aligned}\frac{d}{dt}(\delta s_i^a) &= -\sum_{\boldsymbol{v}} \sigma \bar{D}_{\boldsymbol{v}} \left[(\delta h^a_{i+\boldsymbol{v}}) + \sum_{\boldsymbol{v}'} \sigma \bar{J}_{\boldsymbol{v}'}(\delta s^a_{i+\boldsymbol{v}+\boldsymbol{v}'}) - 4k_B T(\delta s^a_{i+\boldsymbol{v}})\right] \\ &- \bar{\Gamma}(\delta s_i^a) + \bar{\Gamma}\sum_{\boldsymbol{v}} \bar{\chi}_{\boldsymbol{v}}(0)(\delta h^a_{i+\boldsymbol{v}}).\end{aligned} \tag{6.16}$$

Take the Fourier transform of both sides to obtain the dynamical susceptibility,

$$\tilde{\chi}^{ab}(\boldsymbol{q},\omega) = \frac{\left[\bar{\Gamma}\tilde{\chi}(\boldsymbol{q},0) - \tilde{D}(\boldsymbol{q})\right]\delta_{ab}}{-i\omega + \left\{-\tilde{D}(\boldsymbol{q})\left[4k_BT - \tilde{J}(\boldsymbol{q})\right] + \bar{\Gamma}\right\}}, \tag{6.17}$$

where $\delta\tilde{s}^a_{\boldsymbol{q}}(\omega), \delta\tilde{h}^a_{\boldsymbol{q}}(\omega)$ are the Fourier transforms of $\delta s^a_j(t), \delta h^a_j(t)$ in frequency and reciprocal space with

$$\tilde{s}^a_{\boldsymbol{q}}(\omega) = \int_{-\infty}^{\infty} dt \sum_j e^{-i(\boldsymbol{q}\cdot\boldsymbol{R}_j - \omega t)} s^a_j(t), \tag{6.18a}$$

$$s^a_j(t) = \int_{-\infty}^{\infty} d\omega \sum_{\boldsymbol{q}} e^{i(\boldsymbol{q}\cdot\boldsymbol{R}_j - \omega t)} \tilde{s}^a_{\boldsymbol{q}}(\omega), \tag{6.18b}$$

and

$$\tilde{D}(\boldsymbol{q}) = \sigma \sum_{\boldsymbol{v}} \bar{D}_{\boldsymbol{v}} e^{-i\boldsymbol{q}\cdot\boldsymbol{v}}, \tag{6.19a}$$

$$\tilde{J}(\boldsymbol{q}) = \sigma \sum_{\boldsymbol{v}} \bar{J}_{\boldsymbol{v}} e^{-i\boldsymbol{q}\cdot\boldsymbol{v}}. \tag{6.19b}$$

This result implies the zero-frequency susceptibility,

$$\tilde{\chi}^{ab}(\boldsymbol{q}, \omega = 0) = \frac{1}{4k_B} \frac{\delta_{ab}}{T - T_{\mathrm{CW}}(\boldsymbol{q})}, \tag{6.20}$$

with Curie-Weiss temperature $T_{\mathrm{CW}}(\boldsymbol{q}) = \frac{1}{4k_B}\tilde{J}(\boldsymbol{q})$.

Using the fluctuation-dissipation theorem, Eq. (4.5), the spin noise in Fourier space becomes exactly equal to

$$\tilde{S}^{ab}(\boldsymbol{q}, \omega) = \frac{2\hbar\omega}{1 - e^{-\hbar\omega/k_B T}} \frac{\left[\bar{\Gamma}\tilde{\chi}(\boldsymbol{q}, 0) - \tilde{D}(\boldsymbol{q})\right] \delta_{ab}}{\omega^2 + \left\{-\tilde{D}(\boldsymbol{q})\left[4k_B T - \tilde{J}(\boldsymbol{q})\right] + \bar{\Gamma}\right\}^2}. \tag{6.21}$$

In the notation of Eq. (6.11), the paramagnon modes are labelled by $m = \boldsymbol{q} \in 1^{\mathrm{st}}$ Brillouin zone, each with frequency eigenvalue

$$\gamma_m = \gamma_{\boldsymbol{q}} = -\tilde{D}(\boldsymbol{q})\left[4k_B T - \tilde{J}(\boldsymbol{q})\right] + \bar{\Gamma}, \tag{6.22}$$

and right and left eigenvectors $\boldsymbol{v}_m = \boldsymbol{e}_{\boldsymbol{q}}$, $\boldsymbol{v}_m^{-1} = \boldsymbol{e}_{\boldsymbol{q}}^{\dagger}/N_s$, respectively, where $\boldsymbol{e}_{\boldsymbol{q}}^{\dagger} = \left(e^{-i\boldsymbol{q}\cdot\boldsymbol{R}_0}, \ldots, e^{-i\boldsymbol{q}\cdot\boldsymbol{R}_{N-1}}\right)$.

Note that we assumed the presence of N_s $\boldsymbol{R}_i$'s forming a translation-invariant lattice, so there are N_s $\boldsymbol{q}$'s in the 1^{st} Brillouin zone. As a consequence Eq. (6.21) does not have σ appearing explicitly in the numerator. For the NN Heisenberg model in the 2d square lattice we get

$$\tilde{D}(\boldsymbol{q}) = -\frac{d_0(T)}{\hbar}\left[\sin^2\left(\frac{q_z a_0}{2}\right) + \sin^2\left(\frac{q_x a_0}{2}\right)\right], \tag{6.23a}$$

$$\tilde{J}(\boldsymbol{q}) = 2\sigma J\left[\cos\left(q_z a_0\right) + \cos\left(q_x a_0\right)\right]. \tag{6.23b}$$

We remark that $\tilde{D}(\boldsymbol{q})$ does not depend on σ because from Eq. (4.25) $\bar{J}_i^c = 4\sigma|J|$, so that σ cancels

out in the definition of $\tilde{D}(\boldsymbol{q})$. Our results lead to the effective diffusion constant in the HA,

$$\begin{aligned} D_{\rm hom}(\boldsymbol{q}) &\equiv -\frac{\tilde{D}(\boldsymbol{q})\left[4k_BT-\tilde{J}(\boldsymbol{q})\right]}{q^2} \\ &= \frac{d_0(T)a_0^2}{\hbar}\left[k_BT-\sigma J\left(1-\frac{q^2a_0^2}{4}\right)\right]+\mathcal{O}(q^4). \end{aligned} \tag{6.24}$$

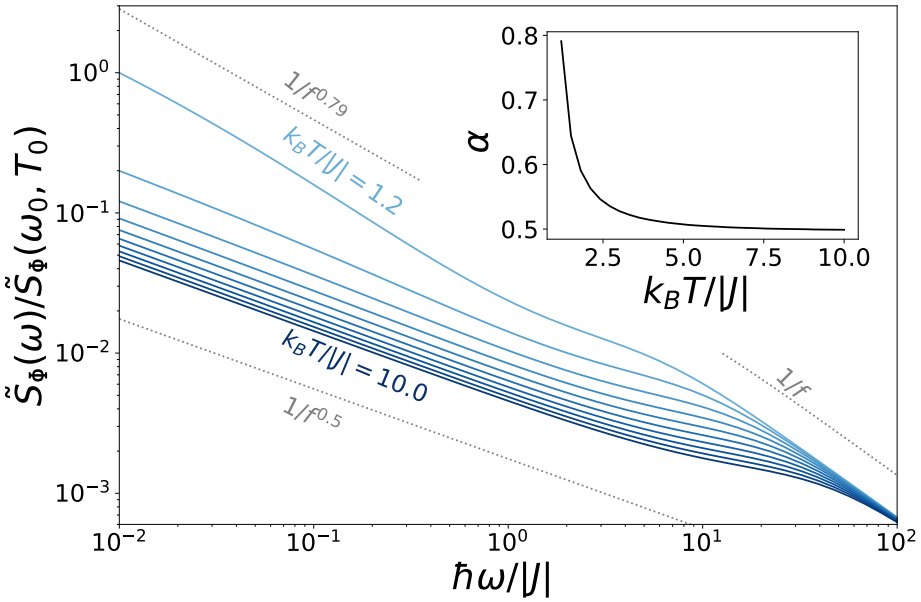

Figure 6.2: ***Frequency dependence of flux noise in an infinite ferromagnet in the paramagnetic phase.***
Calculations of flux noise in the HA approximation for NN interactions and $J > 0$ for $k_BT/|J| = 1.2 - 10$, $\bar{\Gamma} = 0$ and $\sigma = 1$, flux noise is normalized by its value at $\hbar\omega_0 = 10^{-2} \times |J|$ and $k_BT_0 = 1.2 \times |J|$. The inset shows the exponent α dependence on temperature, $\alpha = 0.8 - 0.5$ decreasing with temperature.

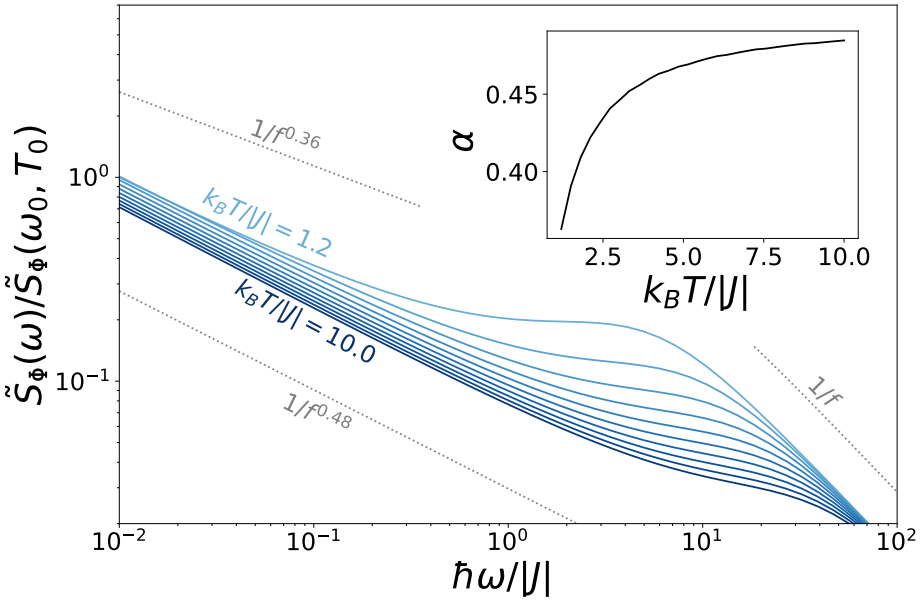

Figure 6.3: ***Frequency dependence of flux noise in an infinite antiferromagnet in the paramagnetic phase.***
Calculations of flux noise in the HA approximation for NN interactions and $J < 0$ for $k_BT/|J| = 1.2 - 10$, $\bar{\Gamma} = 0$ and $\sigma = 1$, flux noise is normalized by its value at $\hbar\omega_0 = 10^{-2} \times |J|$ and $k_BT_0 = 1.2 \times |J|$. The inset shows the exponent α dependence on temperature, $\alpha = 0.35 - 0.5$ increasing with temperature.

6.3.2 Flux Noise and Paramagnon Flux Density

From Eq. (4.8), the flux noise in the HA approximation can be written as

$$\begin{aligned}
\tilde{S}_\Phi(\omega) &= \sum_{i,j,a,b} F^a(\boldsymbol{R}_i)\tilde{S}^{ab}_{ij}(\omega)F^b(\boldsymbol{R}_j) \\
&= \sum_{i,j,a,b}\left[\frac{1}{N_s}\sum_{\boldsymbol{k}} e^{i\boldsymbol{k}\cdot\boldsymbol{R}_i}F^a(\boldsymbol{k})\right]\left[\frac{1}{N_s}\sum_{\boldsymbol{q}} e^{i\boldsymbol{q}\cdot(\boldsymbol{R}_j-\boldsymbol{R}_i)}\tilde{S}^{ab}(\boldsymbol{q},\omega)\right]\left[\frac{1}{N_s}\sum_{\boldsymbol{k'}} e^{i\boldsymbol{k'}\cdot\boldsymbol{R}_j j}F^a(\boldsymbol{k'})\right] \\
&= \frac{1}{N_s}\sum_{a,b,\boldsymbol{q}} \tilde{F}^a(\boldsymbol{q})\tilde{S}^{ab}(\boldsymbol{q},\omega)\tilde{F}^b(-\boldsymbol{q}),
\end{aligned} \tag{6.25}$$

where $\tilde{\boldsymbol{F}}(\boldsymbol{q})$ is the flux vector in Fourier space. Plugging in Eq. (6.21) into Eq. (6.25) and using Eq. (6.11) we find the paramagnon flux density:

$$\rho_\Phi(\gamma) = \frac{1}{N_s\gamma}\sum_{\boldsymbol{q}}\left|\tilde{\boldsymbol{F}}(\boldsymbol{q})\right|^2\left[\bar{\Gamma}\tilde{\chi}(\boldsymbol{q},0)-\tilde{D}(\boldsymbol{q})\right]\delta(\gamma-\gamma_{\boldsymbol{q}}). \tag{6.26}$$

6.3.3 *Long Wavelength Regime*

We assume that the flux vector is given by a simple "single edge model" $\boldsymbol{F}(\boldsymbol{r}) = F_0\delta_{z,0}\hat{\boldsymbol{y}}$ as in Fig. 6.1, this is based on the fact that the flux vector has its maximum value at the edge and it points perpendicular to the wire plane [51]. The flux vector in Fourier space is

$$\tilde{\boldsymbol{F}}(\boldsymbol{q}) = F_0\sum_{\boldsymbol{r}} e^{i\boldsymbol{q}\cdot\boldsymbol{r}}\delta_{z,0}\hat{\boldsymbol{y}} = N_{sx}F_0\delta_{q_x,0}\hat{\boldsymbol{y}}, \tag{6.27}$$

where $N_{sx(z)}$ is the number of sites in the $z(x)$ direction. From Eq. (6.26), the paramagnon flux density in the HA approximation with single edge flux vector is

$$\begin{aligned}\rho_\Phi(\gamma) &= \frac{F_0^2N_{sx}}{N_{sz}\gamma}\sum_q\left[\bar{\Gamma}\tilde{\chi}(q,0)-\tilde{D}(q)\right]\delta(\gamma-\gamma_q)\\ &= \frac{F_0^2a_0N_{sx}}{\pi\gamma}\int_0^{\pi/a}dq\left[\bar{\Gamma}\tilde{\chi}(q,0)-\tilde{D}(q)\right]\delta(\gamma-\gamma_q),\end{aligned} \tag{6.28}$$

with $\boldsymbol{q} = q\hat{\boldsymbol{z}}$ and $q = \frac{2\pi}{N_{sz}a_0}\left(n-\frac{N_{sz}}{2}\right)$ in the first line, with $n = 0,1,\ldots,N_{sz}-1$, and $N_s = N_{sz}N_{sx}$ is the number of occupied sites. The simplest case we can consider is to choose $\tilde{D}(\boldsymbol{q})$ in the long wavelength regime (small q), and assuming NN interactions. In this case

$$\tilde{D}(q) = -\frac{d_0(T)q^2a_0^2}{4\hbar}, \tag{6.29a}$$

$$\tilde{J}(q) = 4\sigma J, \tag{6.29b}$$

$$\gamma_q = \frac{d_0(T)q^2a_0^2}{\hbar}\left[k_BT-\sigma J\right]+\bar{\Gamma}. \tag{6.29c}$$

Plugging these expressions and Eq. (6.20) into Eq. (6.28):

$$\begin{aligned}
\rho_{\Phi}^{lw}(\gamma) &= \frac{F_0^2 a_0 N_{sx}}{4\pi\gamma}\frac{1}{k_BT-\sigma J}\int_0^{\pi/a_0}\gamma_q\,\delta(\gamma-\gamma_q)\,dq \\
&= \frac{F_0^2 a_0 N_{sx}}{4\pi\gamma}\frac{1}{k_BT-\sigma J}\int_{\gamma_{\min}}^{\gamma_{\max}}\left(\gamma_q/\left|\frac{d\gamma_q}{dq}\right|\right)\delta(\gamma-\gamma_q)d\gamma_q \\
&= \frac{F_0^2 a_0 N_{sx}}{8\pi\gamma\sqrt{d_0(T)/\hbar}}\frac{1}{(k_BT-\sigma J)^{3/2}}\int_{\gamma_{\min}}^{\gamma_{\max}}\frac{\gamma_q}{\sqrt{\gamma_q-\bar{\Gamma}}}\delta(\gamma-\gamma_q)d\gamma_q \\
&= \frac{F_0^2 N_{sx}/\pi}{8\sqrt{d_0(T)/\hbar}}\frac{1}{(k_BT-\sigma J)^{3/2}}\frac{\theta(\gamma_{\max}-\gamma)\theta(\gamma-\gamma_{\min})}{\sqrt{\gamma-\bar{\Gamma}}},
\end{aligned} \tag{6.30}$$

with $\theta(\omega)$ the Heaviside step function, $\gamma_{\min}=\bar{\Gamma}$ and $\gamma_{\max}=\gamma_{q=\pi/a_0}$. The flux noise in the long wavelength regime can be calculated from Eq. (6.11), taking $\bar{\Gamma}=0$:

$$\begin{aligned}
\tilde{S}_{\Phi}^{\rm lw}(\omega) &= \frac{F_0^2 N_{sx}}{\pi\sqrt{d_0(T)/\hbar}}\frac{1}{(k_BT-\sigma J)^{3/2}}\frac{\hbar\omega}{1-e^{-\hbar\omega/k_BT}}\int_0^{\gamma_{\max}}\frac{\sqrt{\gamma}}{\omega^2+\gamma^2}d\gamma \\
&= \frac{F_0^2 N_{sx}}{\pi\sqrt{d_0(T)/\hbar}}\frac{k_BT}{(k_BT-\sigma J)^{3/2}}\frac{1}{\sqrt{\omega}}\int_0^{\gamma_{\max}/\omega}\frac{\sqrt{x}}{1+x^2}dx \\
&= \frac{F_0^2 N_{sx}}{2\sqrt{d_0(T)/\hbar}}\frac{k_BT}{(k_BT-\sigma J)^{3/2}}\frac{1}{\sqrt{\omega}},
\end{aligned} \tag{6.31}$$

where in the second line we assumed $\hbar\omega \ll k_BT$ and in the third line we assumed $\omega \ll \gamma_{\max}$.

6.3.4 Phenomenological Flux Noise Model in a Homogeneous Magnet in the Paramagnetic Phase

Figs. 6.2 and 6.3 show numerical calculations of Eq. (6.25) in a wide frequency interval for the FM and AFM case, respectively. The calculations assume the NN Heisenberg model in a square lattice with $J_{ij}=J\sum_{\boldsymbol{v}}\delta_{i,j+\boldsymbol{v}}$ for $\boldsymbol{v}=\pm a_0\hat{\boldsymbol{x}},\pm a_0\hat{\boldsymbol{z}}$; so $\tilde{D}(\boldsymbol{q}),\tilde{J}(\boldsymbol{q})$ are given by Eq. (6.23), the flux vector is given by the "single edge model", $\bar{\Gamma}=0$ and $\sigma=1$. We fit $\tilde{S}_{\Phi}(\omega)$ to $A_{\Phi}^2/\omega^{\alpha}$ in different frequency intervals. In the FM case, the exponent α at low frequencies decreases with temperature from 0.8 to 0.5. The AFM case shows a qualitatively different behaviour, α increases

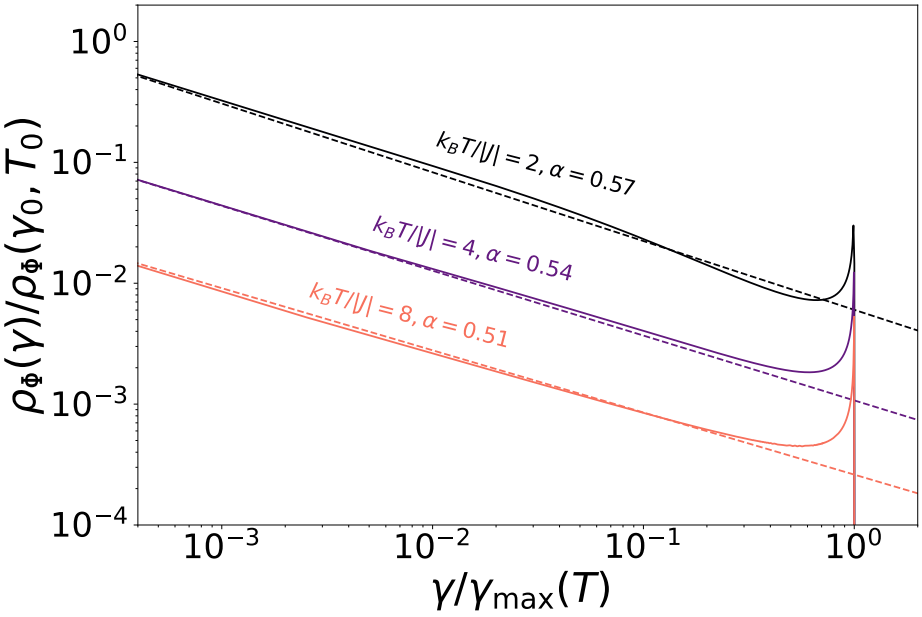

Figure 6.4: ***Frequency dependence of the paramagnon flux density in an infinite magnet.*** *Calculations of $\rho_\Phi(\gamma)$ (solid lines) in the HA approximation for NN interactions and $J > 0$ for $k_BT/|J| = 2$ - 8, $\bar{\Gamma} = 0$ and $\sigma = 1$, $\rho_\Phi(\gamma)$ is normalized by its value at $\hbar\omega_0 = 10^{-3} \times |J|$ and $k_BT_0 = 2 \times |J|$, the x axis is normalized by the value $\gamma_{\max}(T)$, here $\gamma_{\min} = 0$. Fits of the form C/γ^α are shown in dashed lines, α decreases with temperature.*

with temperature from 0.3 to 0.5 at low frequencies. Both cases show a $1/\omega$ dependence at high frequencies as expected from Eq. (6.25) for $\omega \gg \mathrm{Max}_q\{\gamma_q\}$. Note that the long wavelength approximation (Eq. (6.31)) predicts $\alpha = 0.5$, this is a good approximation at higher temperatures, however, when T is closer to T_c^{mag}, α shows a significant temperature dependence.

We can understand this difference in qualitative behaviour to the long wavelength approximation by noting that in this case, the flux noise depends on short wavelength contributions ($\boldsymbol{q}$ at the edges of the first Brillouin zone) as seen in Eq. (6.25). By accounting for larger wavevectors, the derivative $\frac{d\gamma_q}{dq}$ in the denominator of Eq. (6.30) has a complex dependence on T and J and is not directly proportional to $\sqrt{\gamma_q}$ as in the simple long wavelength case. In this regime, it is better described by a γ_q^α-dependence with an exponent α that depends on the interplay between T and J. This interplay is washed off at high temperatures as implied by Eq. (6.22).

Based on these flux noise calculations and the previous discussion, we propose the following

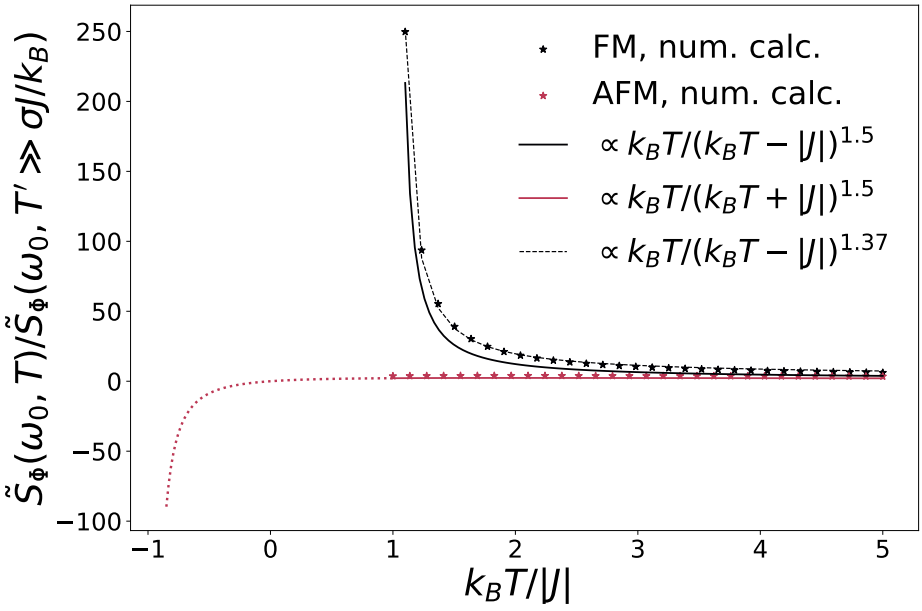

Figure 6.5: ***Temperature dependence of flux noise in an infinite magnet.*** *Calculations of flux noise in the HA approximation for NN interactions and $J>0$, $J<0$ normalized by its value at $k_BT'=100\times|J|\gg|J|$. $\hbar\omega_0=10^{-3}\times|J|$, $d_0=1$, $\bar{\Gamma}=0$ and $\sigma=1$.*

phenomenological expression for the paramagnon flux density:

$$\rho_\Phi(\gamma)=C(T)\frac{\theta(\gamma_{\max}-\gamma)\theta(\gamma-\gamma_{\min})}{\gamma^\alpha}, \tag{6.32}$$

to confirm this assumption, we calculate Eq. (6.26) for different temperatures and we fit the result to a function of the form (6.32) to find the exponent α. The calculations assume FM ($J>0$) NN interactions, single edge model flux vector, $\bar{\Gamma}=0$ and $\sigma=1$. The results are shown in Fig. (6.4), this confirms the proposed expression is a good approximation for $\gamma_{\min}<\gamma<\gamma_{\max}$. Using Eq. (6.32) in Eq. (6.11):

$$\begin{aligned}\tilde{S}_\Phi(\omega) &= \frac{2\hbar\omega}{1-e^{-\hbar\omega/k_BT}}C(T)\int_{\gamma_{\min}}^{\gamma_{\max}}\frac{\gamma^{1-\alpha}}{\omega^2+\gamma^2}d\gamma \\ &= \frac{2\hbar\omega}{1-e^{-\hbar\omega/k_BT}}\frac{C(T)}{\omega^\alpha}b_\alpha(\omega),\end{aligned} \tag{6.33}$$

with

$$b_\alpha(\omega) = \int_{\gamma_{\min}/\omega}^{\gamma_{\max}/\omega} \frac{x^{1-\alpha}}{1+x^2} dx, \tag{6.34}$$

$b_\alpha(\omega) \approx \pi/[2\sin(\pi\alpha/2)]$ when $\gamma_{\min} \ll \omega \ll \gamma_{\max}$. We can find the prefactor $C(T)$ from

$$\int d\gamma \rho_\Phi(\gamma) = C(T)\frac{\gamma_{\max}^{1-\alpha}}{1-\alpha} = C(T)\frac{(4d_0 k_B T/\hbar)^{1-\alpha}}{1-\alpha}, \tag{6.35}$$

for $\alpha < 1$, and from Eq. (6.26)

$$\begin{aligned}
\int d\gamma \rho_\Phi(\gamma) &= -\frac{1}{N_s}\sum_{\boldsymbol{q}} \left|\tilde{\boldsymbol{F}}(\boldsymbol{q})\right|^2 \frac{1}{\gamma_{\boldsymbol{q}}}\left[\tilde{D}(\boldsymbol{q})\right] \\
&= \frac{1}{N_s}\sum_{\boldsymbol{q}} \frac{\left|\tilde{\boldsymbol{F}}(\boldsymbol{q})\right|^2}{4k_B T - \tilde{J}(\boldsymbol{q})}, \\
&= \frac{\sigma\sum_i |\boldsymbol{F}_i|^2}{4\left(k_B T - \sigma J\right)},
\end{aligned} \tag{6.36}$$

where in the second line we used Eq. (6.22), and in the third line, we assumed the typical scale for variations in $\boldsymbol{F}(\boldsymbol{r})$ is much larger than the lattice spacing a_0, so that $\tilde{J}(\boldsymbol{q})$ can be approximated by $\tilde{J}(0) = 4\sigma J$, in this analysis we assume $\bar{\Gamma} = \gamma_{\min} = 0$. Calculating $C(T)$ from this equation and plugging it into Eq. (6.33) we get a phenomenological model of flux noise based on an analytic model and numerical corrections that describe its frequency and temperature dependence:

$$\begin{aligned}
\tilde{S}_\Phi(\omega) &= \frac{\hbar\omega}{1-e^{-\hbar\omega/k_B T}} \frac{\sigma(1-\alpha)\sum_i |\boldsymbol{F}_i|^2}{2(4d_0/\hbar)^{1-\alpha}\left(k_B T - \sigma J\right)^{2-\alpha}} \frac{1}{\omega^\alpha} b_\alpha(\omega) \\
&\equiv C' \frac{\hbar\omega}{1-e^{-\hbar\omega/k_B T}} \frac{1}{(d_0(T))^{1-\alpha}\left(k_B T - \sigma J\right)^{2-\alpha}} \frac{b_\alpha(\omega)}{\omega^\alpha}.
\end{aligned} \tag{6.37}$$

Note that for $\hbar\omega \ll k_B T$,

$$\frac{\tilde{S}_\Phi(\omega, T)}{\tilde{S}_\Phi(\omega, T \gg \sigma\bar{J}/k_B)} \propto \frac{1}{d_0(T)^{1-\alpha}} \frac{k_B T}{(k_B T - \sigma J)^{2-\alpha}}. \tag{6.38}$$

Fig. 6.5 shows numerical calculations of Eq. (6.25) for different temperatures for both FM and AFM for $\hbar\omega \ll k_B T$, $d_0 = 1$ and same assumptions as before. Both cases show a $k_B T/(k_B T - J)^{\delta}$ dependence with a $\delta \approx 1.4$, this shows that Eq. (6.38) accurately describes $\tilde{S}_{\Phi}(T)$.

6.4 Confined Magnet in the Paramagnetic Phase

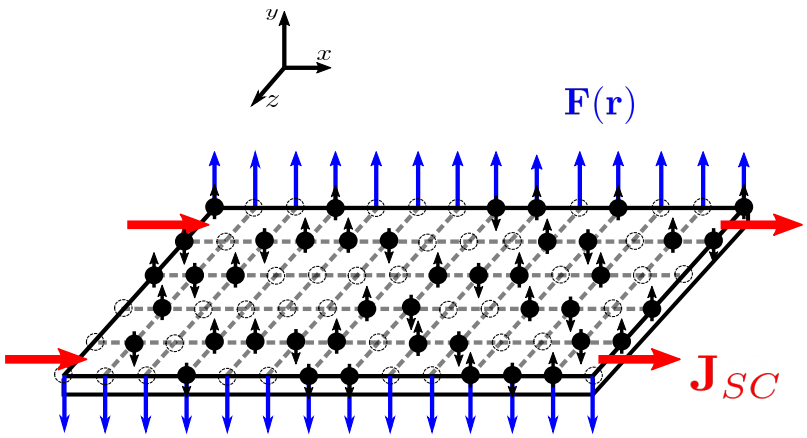

Figure 6.6: ***Section of a superconducting wire with spin impurities randomly distributed on its surface.***
The flux produced by each spin is given by $\hat{\Phi}_i = -\boldsymbol{F}(\boldsymbol{R}_i) \cdot \hat{\boldsymbol{s}}_i$, where $\hat{\boldsymbol{s}}_i$ is the spin operator of an impurity located at $\boldsymbol{r} = \boldsymbol{R}_i$. The "flux vector" $\boldsymbol{F}(\boldsymbol{r})$ points along the magnetic field produced by the current density $\boldsymbol{J}_{SC}$ shown in the figure, it is described here by a "double edge model".

6.4.1 Impact of Confinement

We now present numerical results for the general problem of a virtual lattice of spins with confinement and disorder where analytic results can not be derived. Figs. 6.7 and 6.8 show numerical calculations of Eq. (6.10) in a wide frequency interval for the FM ($J > 0$) and AFM ($J < 0$) case, respectively. For these calculations, we consider a 3×50 ($N = 150$) "virtual" lattice with all sites occupied ($\sigma = 1$) and no spin-lattice relaxation, $\Gamma_i = 0$. All calculations are done with open b.c. along $\hat{z}$, and periodic b.c. along $\hat{x}$, describing spins confined (along $\hat{z}$) within

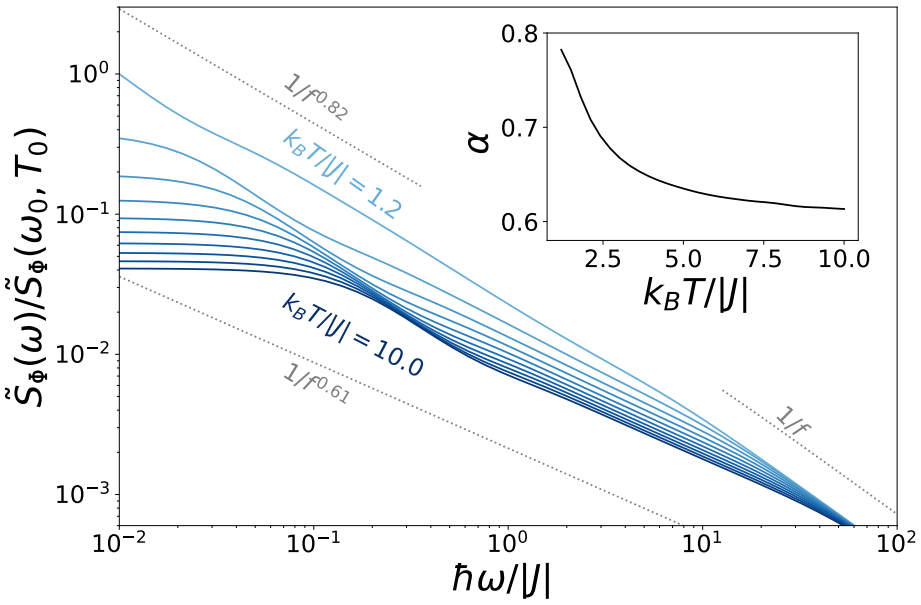

Figure 6.7: ***Frequency dependence of flux noise in a confined ferromagnet in the paramagnetic phase.***
Calculations of flux noise in a confined wire and $J > 0$ for $k_BT/|J| = 1.2 - 10$, $\Gamma_i = 0$ and $\sigma = 1$, flux noise is normalized by its value at $\hbar\omega_0 = 10^{-2} \times |J|$ and $k_BT_0 = 1.2 \times |J|$. The inset shows the exponent α dependence on temperature, $\alpha = 0.8 - 0.6$ decreasing with temperature.

the region of an infinite (along $\hat{x}$) SC wire, this is why it is enough to take 3 sites along the $\hat{x}$ direction. The flux vector is described by the "double edge model" shown in Fig. 6.6:

$$\boldsymbol{F}(\boldsymbol{r}) = F_0(\delta_{z,-W/2} - \delta_{z,W/2})\hat{\boldsymbol{y}}, \tag{6.39}$$

where W is the wire width and $\delta_{z,\pm W/2}$ are Kronecker delta functions. Equation (6.39) gives a good description of thin-film wires where it is shown that $\boldsymbol{F}_i$ is sharply peaked at the wire edges [51]. Note that in this case, the "single edge model" used in the HA is not adequate since we assume there are no spins outside the wire, this makes evident the impact of edges (confinement). All calculations assume the NN Heisenberg model in a 2-d lattice.

We fit $\tilde{S}_\Phi(\omega)$ to A_Φ^2/ω^α in different frequency intervals as seen in the figures. In the FM case, the exponent α at low frequencies decreases with temperature from 0.8 to 0.6. The AFM

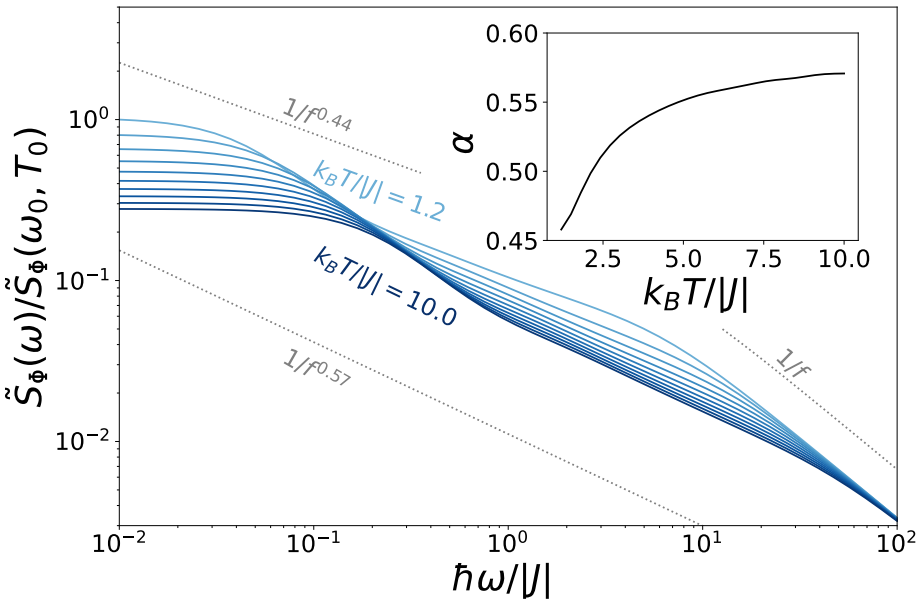

Figure 6.8: ***Frequency dependence of flux noise in a confined antiferromagnet in the paramagnetic phase.***
Calculations of flux noise in a confined wire and $J < 0$ for $k_BT/|J| = 1.2 - 10$, $\Gamma_i = 0$ and $\sigma = 1$, flux noise is normalized by its value at $\hbar\omega_0 = 10^{-2} \times |J|$ and $k_BT_0 = 1.2 \times |J|$. The inset shows the exponent α dependence on temperature, $\alpha = 0.45 - 0.6$ increasing with temperature.

case shows a qualitatively different behaviour, α increases with temperature from 0.45 to 0.6 at low frequencies. Both cases show a $1/\omega$ dependence at high frequencies. Interestingly, several experiments with niobium devices measure α within this range [74, 75].

Note that the apparent transition to lorentzian noise at low frequencies is an artifact of the numeric calculations: when $\omega < \mathrm{Min}\{\gamma_\mathrm{m}\}$, the noise is described by the contribution with the lowest γ_m, in the limit where the lattice sites in the $\hat{z}$ direction go to infinity, $\mathrm{Min}_m\{\gamma_m\} \to 0$. The coefficient α is thus modified by edge effects compared to the HA where these effects don't exist, the qualitative behaviour remains the same but $\alpha \to 0.6$ as temperature increases as opposed to the HA where $\alpha \to 0.5$, this demonstrates the importance of confinement.

Additionally, Fig. 6.9 shows numerical calculations of the temperature dependence of Eq. (6.10) for different temperatures for both FM and AFM for $\hbar\omega \ll k_BT$, $d_0 = 1$ and same assumptions as before. Both cases show a $k_BT/(k_BT - J)^\delta$ dependence with a $\delta \approx 1.4$ similar to Fig.

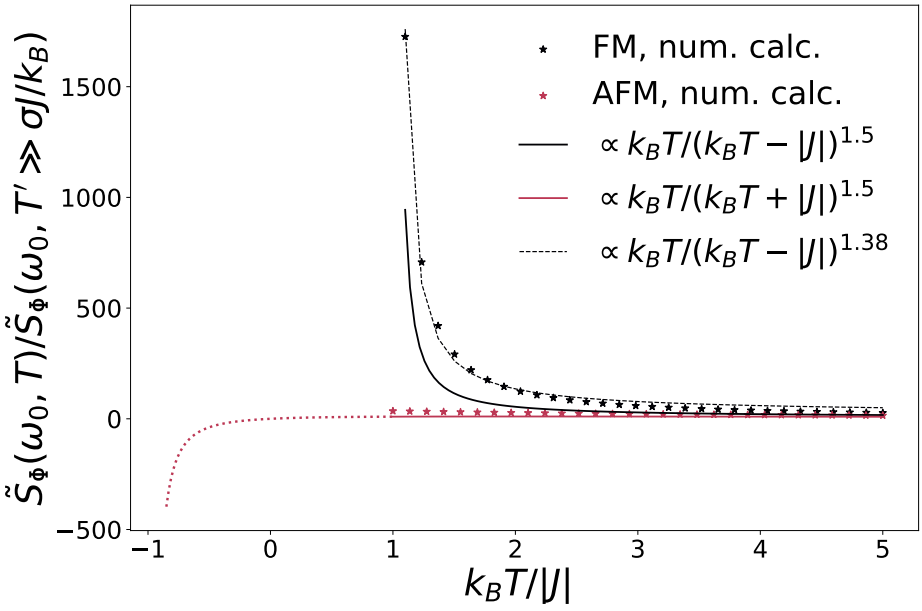

Figure 6.9: ***Temperature dependence of flux noise in a confined magnet.*** *Calculations of flux noise in a confined wire for NN interactions and $J>0$, $J<0$ normalized by its value at $k_BT'=100\times|J|\gg|J|$. $\hbar\omega_0=10^{-3}\times|J|$, $d_0=1$, $\Gamma_i=0$ and $\sigma=1$.*

6.5. This shows that phenomenological expression in Eq. (6.38) describes $\tilde{S}_\Phi(T)$ correctly even in confined systems for a suitable α.

6.4.2 Impact of Disorder due to Vacancies

Figure 6.10 shows explicit calculations of the frequency exponent α from the fits $\tilde{S}_\Phi(\omega)\propto A_\Phi^2/\omega^\alpha$ as a function of T and spin density $\sigma=0.5,0.75,1$. In this case we consider a 20×20 (N = 400) "virtual" square lattice. We randomly populate $N_s\leq N$ sites with spins, yielding spin density $\sigma=N_s/N$, the empty sites are called *vacancies*. All calculations below are done with open b.c. along $\hat{z}$, and periodic b.c. along $\hat{x}$ and NN interactions, as before. The results were averaged over 512 instances for the cases with $\sigma<1$. α *decreases* with T for the FM model, and has the opposite behavior for the AFM model. As σ decreases from 1, α further deviates from its infinite/homogeneous value of $1/2$. This demonstrates the impact of disorder. Note how the dependence of α on σ is nonmonotonic.

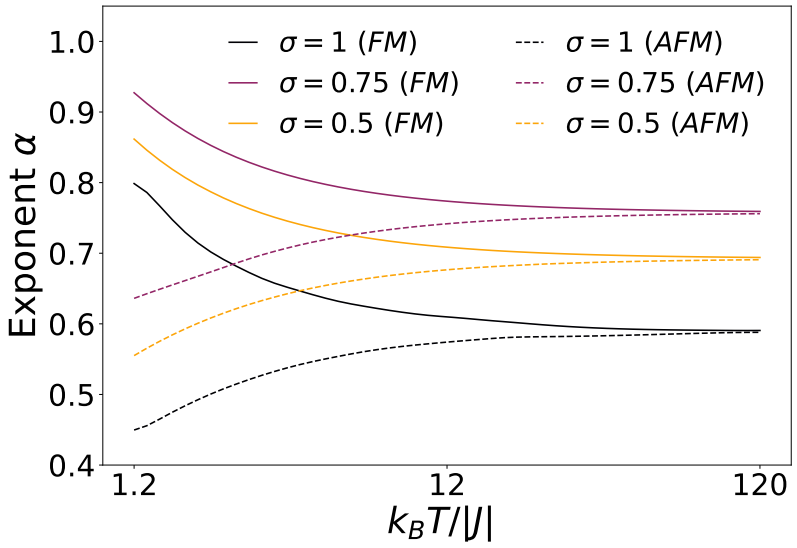

Figure 6.10: ***Spin density dependence of exponent α***
Explicit calculations of flux noise frequency exponent α as a function of temperature in the NN Heisenberg model with confinement and disorder due to vacancies in a 20x20 square lattice and $\Gamma_i = 0$. Note how α decreases (increases) with T for the FM (AFM) cases. In all cases $\alpha > 1/2$ demonstrating the relevance of confinement and disorder. The dependence of α on σ is nonmonotonic.

6.4.3 Impact of Disorder due to a Wide Distribution of Relaxation Rates

Now consider the impact of nonzero spin-lattice relaxation Γ_i in co-existance with spin-spin interaction. Figure 6.11 shows numerical calculations using the second-principles theory, for $\sigma = 1$ and other parameters as in Fig. 6.10 with the addition of a wide distribution of relaxation rates Γ_i given by the cross-relaxation model from Eq. (5.18). The results are presented in terms of different choices of $\Gamma_c' = \hbar\Gamma_c/(d_0(T)|J|)$. $\lambda_{\max} = 20$ in all calculations.

The results show that the addition of a wide distribution of Γ_i to the interacting spin system increases α in the low to intermediate T range. At high T, the impact of Γ_i is washed out, this is expected from Eq. (6.3a), at high temperatures the impact of spin-spin interactions dominate over the temperature independent relaxation rates.

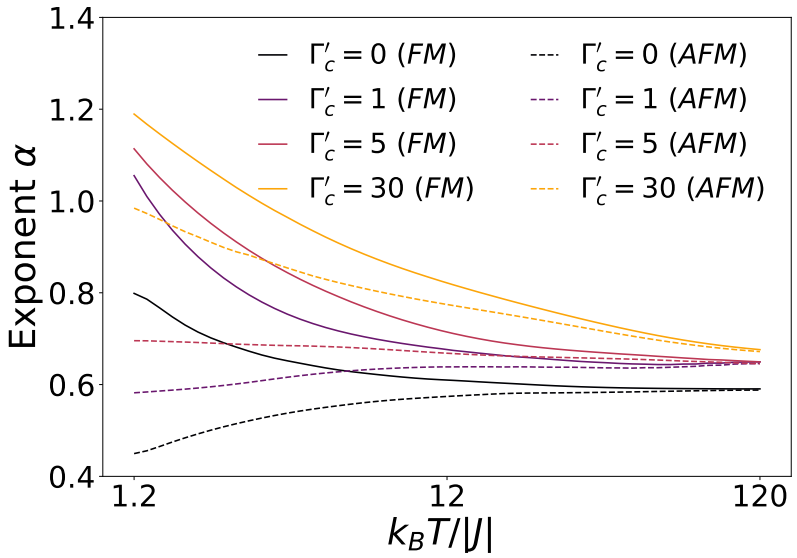

Figure 6.11: ***Impact of spin-lattice relaxation in exponent α***
Explicit calculations of flux noise frequency exponent α as a function of temperature in the NN Heisenberg model with confinement and disorder due to a wide distribution of relaxation rates in co-existance with spin-spin interactions in a 20x20 square lattice. α decreases (increases) with T for the FM (AFM) cases and increases as Γ'_c increase compared to its value at $\Gamma_c = 0$.

6.5 Conclusions

This chapter presented results of flux noise from different spin scenarios using the theoretical framework described in chapter 4. We showed that choosing D_{ij} consistent with $D\nabla^2$ (third-principles theory) and assuming an infinite, translation-invariant spin system leads to temperature-independent noise exponent $\alpha = 1/2$, in contradiction to experiments. In contrast, numerical calculations with the "second principles" prescription for D_{ij} even in an infinite magnet predict a temperature-dependent exponent α. Based on these results we propose a phenomenological expression, Eq. 6.37, that describes accurately the frequency and temperature dependence of flux noise and agrees with experimental observations. Furthermore, we show how confinement and disorder due to vacancies and a wide distribution of relaxation rates have an impact in the numerical value of α. The calculated values of this exponent are within the range observed in experiments performed in Nb devices as seen in Fig. 3.5.

CHAPTER 7

Charge and Flux Noise from Wire-Resident Superconducting Quasiparticles

This chapter is an expanded version of publication [3].

7.1 Introduction

The presence of QPs in superconductors is known to give rise to surface resistance and Ohmic loss [76]. Their impact on SC qubits is believed to be the greatest when they tunnel across a Josephson junction, leading to energy relaxation and dephasing, thereby limiting qubit performance [11–13, 61].

Several experiments show that a large population of QPs remains even at low temperatures ($k_B T \ll \Delta$), in spite of the thermal QP density being exponentially small ($\propto e^{-\Delta/k_B T}$, where Δ is the SC energy gap) [77, 78]. These non-equilibrium QP densities arise from external perturbations, such as stray infrared photons or ionizing radiation [79–81], posing a great challenge to qubit coherence (see Fig. 7.1).

An additional puzzle is the energy distribution of this excess of QPs. Recent experiments provided evidence of *quasiequilibrium*, where Fermi gas of QPs is in thermal equilibrium with the surrounding phonon bath despite the out-of-equilibrium QP density [82]. Current designs of SC circuits engineer junction asymmetries in order to prevent QP tunneling across the circuit's Josephson junctions, greatly reducing the impact of the QP tunneling mechanism [82, 83]. Furthermore, QPs are also known to hinder the performance of SC resonators, having an impact on their quality factor [84, 85].

Here we show that the Ohmic loss induced by QPs within the SC wires themselves gives rise to charge and flux noise even when the QPs are far from the junctions. Our explicit numerical calculations show that the associated charge noise can be larger than the contribution arising from TLSs. The resulting charge noise can also be interpreted as current/flux fluctuations, showing that Ohmic loss gives rise to a flux noise background that is logarithmic in frequency. The magnitude of the predicted "nearly white flux noise background" is found to be comparable to values observed in flux-tunable qubits [48, 86].

The rest of this chapter is organized as follows. Section 7.2 contains a discussion on the complex SC conductivity and Mattis-Bardeen theory. Section 7.3 presents the results of charge and flux noise due to a quasithermal QP distribution in the SC wire. Finally, section 7.4 presents the conclusions.

7.2 Conductivity of a Superconductor in Mattis-Bardeen Theory

In normal metals, the conductivity is dominated by the scattering of electrons. In superconductors, the conductivity is inherently complex, including both dissipative and reactive components that describe the material's response to electromagnetic fields. This complex conductivity, $\sigma(\omega) = \sigma_1(\omega) + i\sigma_2(\omega)$, provides a profound insight into the unique electromagnetic behaviors of superconductors. The frequency-dependent conductivities of a Bardeen-Cooper-Schrieffer (BCS) superconductor are straightforward to calculate when the QP distributions $n(E)$ differ from the equilibrium Fermi-Dirac functions $f(E)$. Here $E \equiv E_k = \sqrt{\xi_k^2 + \Delta^2}$ is the BCS QP energy, with $\xi_k = \epsilon_k - \epsilon_F$ the free electron energy measured from the Fermi level ϵ_F. A slight generalization of Mattis-Bardeen theory [76] leads to

$$\begin{aligned} \frac{\sigma_1}{\sigma_N} &= \frac{2}{\hbar\omega}\int_{\Delta}^{\infty} dE \frac{E(E+\hbar\omega)+\Delta^2}{\sqrt{E^2-\Delta^2}\sqrt{(E+\hbar\omega)^2-\Delta^2}} \\ &\times \left[n(E) - n(E+\hbar\omega)\right], \end{aligned} \tag{7.1}$$

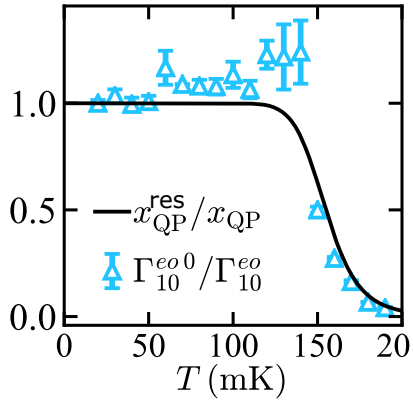

(a)

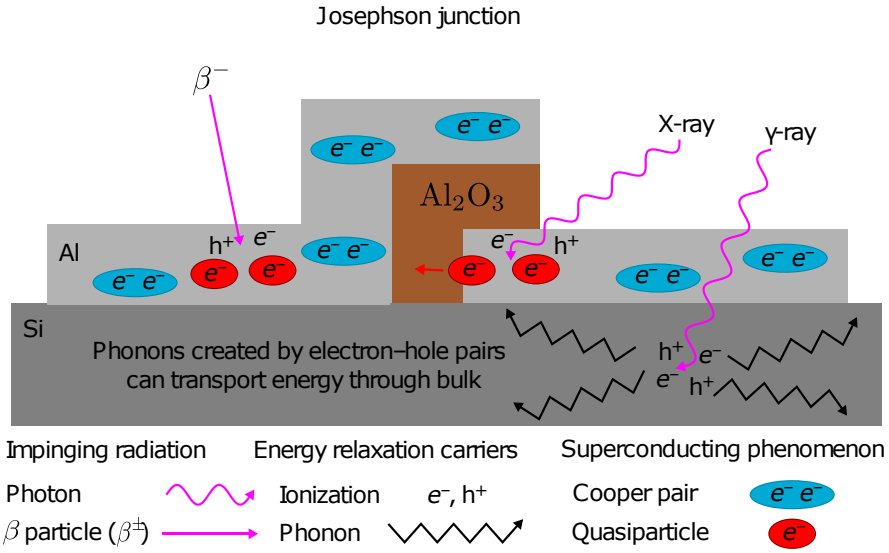

(b)

Figure 7.1: ***Origin of non-equilibrium quasiparticle densities at low temperatures.*** *Presence of a non-equilibrium density of QPs at low temperatures, this population is due to external perturbations like stray photons and ionizing radiation.* ***(a)*** $1/\Gamma_{10}^{eo}$ *normalized by its base temperature value* $1/\Gamma_{10}^{eo0}$*, as a function of temperature measured in [78].* Γ_{10}^{eo} *is the transmon relaxation rate due to charge-parity switching only (QP tunneling across a Josephson junction). The solid black line is a fit to the thermal dependence of* $x_{QP}^{\mathrm{res}}/x_{QP}$ *where* x_{QP}^{res} *is the number of resident QPs (due to a non-equilibrium QP density) normalized by the number of electrons bound as Cooper pairs. This shows the dominant presence of resident QPs at low temperatures. Here,* $x_{QP}^{\mathrm{res}} = 1 \times 10^{-7}$ *[87].* ***(b)*** *Ionizing radiation impacting with the Al qubit and Si substrate. As a result, Cooper pairs are broken [81, 88].*

$$\begin{aligned}\frac{\sigma_2}{\sigma_N} &= \frac{1}{\hbar\omega}\int_{\Delta-\hbar\omega}^{\Delta} dE \frac{E(E+\hbar\omega)+\Delta^2}{\sqrt{\Delta^2-E^2}\sqrt{(E+\hbar\omega)^2-\Delta^2}} \\ &\times \left[1-2n(E+\hbar\omega)\right]. \end{aligned} \tag{7.2}$$

which is exact at subgap frequencies, $\hbar\omega < 2\Delta$. Here σ_N is the non-SC (normal state) conductivity.

In order to connect to experiments, it is fruitful to express σ_1 in terms of the number of QPs divided by the number of electrons bound as Cooper pairs [12, 13, 82],

$$x_{\rm QP} = \frac{N_{QP}}{2\rho\Delta} = \frac{1}{\Delta}\int_{-\infty}^{\infty} d\xi\; n(\sqrt{\xi^2+\Delta^2}), \tag{7.3}$$

where ρ is the electron energy density near ϵ_F. We assume that the QP distribution follows a "quasithermal" law $n(E) \approx n_0 e^{-E/k_BT}$; this is justified by recent experimental observations where it was concluded that despite their non-equilibrium density, the Fermi gas of QPs is still in equilibrium with the phonon bath [82]. Here n_0 does not depend on QP energy E or frequency ω, but it may depend on other parameters such as temperature T and gap Δ. For thermal equilibrium we get $n_0 = 1$, as can be seen from $n(E) = f(E) = 1/(e^{E/k_BT}+1) \approx e^{-E/k_BT}$ for $E \gg k_BT$. When the quasithermal law is followed and $k_BT \ll \Delta$, the QP density of states can be expanded around its singularity at $E = \Delta$: $E/\sqrt{E^2-\Delta^2} \approx \sqrt{\Delta/[2(E-\Delta)]}$. Under this

approximation we get

$$\begin{aligned} x_{QP} &= \frac{2}{\Delta}\int_0^\infty dE \frac{d\xi}{dE}\, n(E) \\ &= \frac{2}{\Delta}\int_\Delta^\infty dE \frac{E}{\sqrt{E^2-\Delta^2}}\, n(E) \\ &= 2\int_0^\infty dx \frac{x+1}{\sqrt{x+2}\sqrt{x}}\, n\left((1+x)\Delta\right) \\ &\approx \sqrt{2}\int_0^\infty dx \frac{1}{\sqrt{x}}\, n\left((1+x)\Delta\right) \\ &= \sqrt{2}n_0 e^{-\Delta/k_BT}\int_0^\infty dx \frac{e^{-x\Delta/k_BT}}{\sqrt{x}} \\ &= n_0\sqrt{\frac{2\pi k_BT}{\Delta}}e^{-\Delta/k_BT}, \end{aligned} \tag{7.4}$$

where in the third line we defined $x = (E-\Delta)/\Delta$ and in the fifth line the assumed $n(E)$ follows the quasithermal law.

When both $\hbar\omega$ and k_BT are much smaller than Δ, the conductivity is also dominated by the singularity in the QP density of states; as a result, the same approximation as in Eq. (7.4) leads

to the following analytic approximation for the real conductivity:

$$\begin{aligned}
\frac{\sigma_1}{\sigma_N} &\approx \frac{2\Delta}{\hbar\omega}\int_{\Delta}^{\infty} dE \frac{1}{\sqrt{(E-\Delta)(E+\hbar\omega-\Delta)}}\left[n(E)-n(E+\hbar\omega)\right] \\
&= \frac{2\Delta}{\hbar\omega}\int_{0}^{\infty} dx \frac{1}{\sqrt{x(x+\hbar\omega/\Delta)}}\left[n\left((1+x)\Delta\right)-n\left((1+x+\hbar\omega/\Delta)\Delta\right)\right] \\
&= \frac{2\Delta}{\hbar\omega}\left(1-e^{-\hbar\omega/k_BT}\right)\int_{0}^{\infty} dx \frac{n\left((1+x)\Delta\right)}{\sqrt{x(x+\hbar\omega/\Delta)}} \\
&= \frac{2\Delta}{\hbar\omega}\left(1-e^{-\hbar\omega/k_BT}\right)\int_{0}^{\infty} dx \frac{n\left((1+x)\Delta\right)}{\sqrt{x(x+\hbar\omega/\Delta)}} \\
&= \frac{2\Delta}{\hbar\omega}\left(1-e^{-\hbar\omega/k_BT}\right) n_0 e^{-\Delta/k_BT}\int_{0}^{\infty} dx \frac{e^{-x\Delta/k_BT}}{\sqrt{x(x+\hbar\omega/\Delta)}} \\
&= \frac{4\Delta}{\hbar\omega} n_0 e^{-\Delta/k_BT}\sinh\left(\frac{\hbar\omega}{2k_BT}\right)K_0\left(\frac{\hbar\omega}{2k_BT}\right) \\
&= x_{\mathrm{QP}}\left(\frac{2\Delta}{k_BT}\right)^{3/2}\frac{1}{\sqrt{\pi}}\left(\frac{k_BT}{\hbar\omega}\right)\sinh\left(\frac{\hbar\omega}{2k_BT}\right)K_0\left(\frac{\hbar\omega}{2k_BT}\right), \qquad (7.5)
\end{aligned}$$

where $K_0(y)$ is the modified Bessel function of the second kind. Figure 7.2 compares Eq. (7.5) to exact numerical integration of both Eqs. (7.1) and (7.3) in thermal equilibrium with $k_BT/\Delta = 0.1$. We find that Eq. (7.5) approximates the exact result quite well provided that $\hbar\omega, k_BT \lesssim 0.1\Delta$.

Note that

$$K_0(y) = \begin{cases} \ln(2/y) - \gamma_E & \text{when } y \ll 1 \\ e^{-y}\sqrt{\pi/(2y)} & \text{when } y \gg 1. \end{cases} \qquad (7.6)$$

where $\gamma_E = 0.5772\ldots$ is the Euler-Mascheroni constant. Thus, the behaviour of σ_1 depends critically on the value of frequency relative to the thermal frequency $k_BT/\hbar$. In the low frequency regime of $\hbar\omega \ll k_BT$, σ_1 is logarithmic in frequency as

$$\frac{\sigma_1}{\sigma_N} \approx \frac{1}{2\sqrt{\pi}} x_{\mathrm{QP}}\left(\frac{2\Delta}{k_BT}\right)^{3/2}\left[\ln\left(\frac{4k_BT}{\hbar\omega}\right)-\gamma_E\right], \qquad (7.7)$$

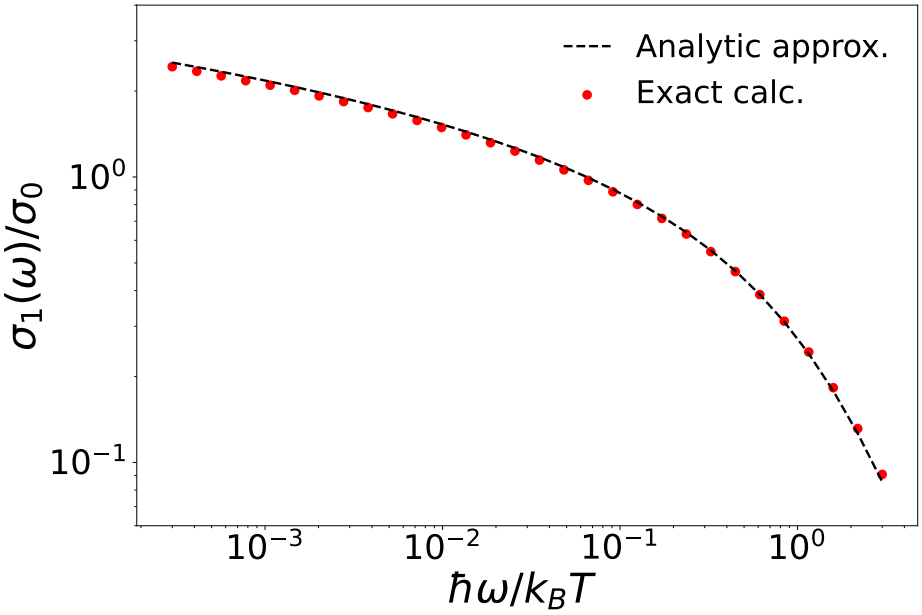

Figure 7.2: ***Numerical calculation of $\sigma_1(\omega)$.***
The calculation assumes the QP distribution is given by the quasithermal, $n(E) \propto e^{-E/k_BT}$ (here $n_0 = 1$). The plot is normalized by $\sigma_0 = \sigma_N x_{\rm QP} (2\Delta/k_BT)^{3/2}$. In the low frequency range $\hbar\omega \lesssim k_BT$, σ_1 decreases logarithmically with increasing ω; in the high frequency range it decreases as a power law. When $k_BT \lesssim 0.1\Delta$, the exact numerical result (red points) is well approximated by the analytical expression Eq. (7.5) (shown as a dashed line for comparison).

In the opposite high-frequency regime of $\hbar\omega \gg k_BT$, σ_1 is instead a power law,

$$\frac{\sigma_1}{\sigma_N} \approx \frac{1}{2} x_{\rm QP} \left(\frac{2\Delta}{\hbar\omega}\right)^{3/2}. \tag{7.8}$$

7.3 Effective Impedance Model of Quasiparticles

7.3.1 Dynamical Susceptibility

The linear response in a general circuit due to a small perturbation in voltage V is $V = Z\langle\delta I\rangle = -i\omega Z\langle\delta Q\rangle$, where $Z = Z' + iZ''$ is a complex impedance with Z', Z'' its real and imaginary

parts, respectively. The charge susceptibility in a wire is thus given by $\tilde{\chi}_Q(\omega) = \frac{\langle \delta Q \rangle}{V} = -\frac{1}{i\omega Z}$. The impact of SC QPs in a wire can be modeled as an effective frequency-dependent impedance $Z_{\mathrm{QP}}(\omega) = \frac{\ell}{A\sigma(\omega)}$, where $\sigma(\omega)$ is the superconductor's complex conductivity, and ℓ, A are the wire's length and cross-sectional area, respectively. The charge susceptibility due to the presence of QPs in a wire is then $\tilde{\chi}_Q(\omega) = \frac{iA\sigma(\omega)}{\omega\ell}$ and its imaginary part is

$$\mathrm{Im}\left\{\tilde{\chi}_Q(\omega)\right\} = \frac{A\sigma_1(\omega)}{\ell\omega}, \tag{7.9}$$

$\sigma_1(\omega)$ given by Eq. (7.1).

7.3.2 *Quasithermal Energy Distribution*

As mentioned above, we assume the QP distribution is well described by a quasithermal law $n(E) = n_0 e^{-E/k_B T}$. We can write n_0 as a function of x_{QP} from Eq. (7.4), the distribution is thus

$$n(E) = x_{\mathrm{QP}} \sqrt{\frac{\Delta}{2\pi k_B T}} e^{-\frac{E-\Delta}{k_B T}}, \tag{7.10}$$

where x_{QP} is modeled as

$$x_{\mathrm{QP}} = x_{\mathrm{QP}}^{\mathrm{res}} + \sqrt{2\pi k_B T/\Delta} e^{-\Delta/k_B T}. \tag{7.11}$$

The first and second terms are due to non-equilibrium QP distributions (resident QPs) and thermal QP distributions (thermal QPs), respectively. At high temperatures $k_B T \geq 100$ mK, thermal QPs will dominate x_{QP}: for $x_{\mathrm{QP}} \approx \sqrt{2\pi k_B T/\Delta} e^{-\Delta/k_B T}$, $n(E) \approx e^{-\frac{E}{k_B T}}$, recovering the thermal distribution. On the contrary, at lower temperatures, resident QPs with temperature-independent density dominate. Since proper functionality of SC qubits requires low temperatures, we will focus on the latter.

7.3.3 *Charge Noise*

Using the fluctuation-dissipation theorem (it can be shown it remains valid for quasithermal distributions, see Apprendix A), the quasithermal distribution, Eq. (7.10), and Eq. (7.9), we can calculate the power spectral density of charge fluctuations (charge noise) contribution due to

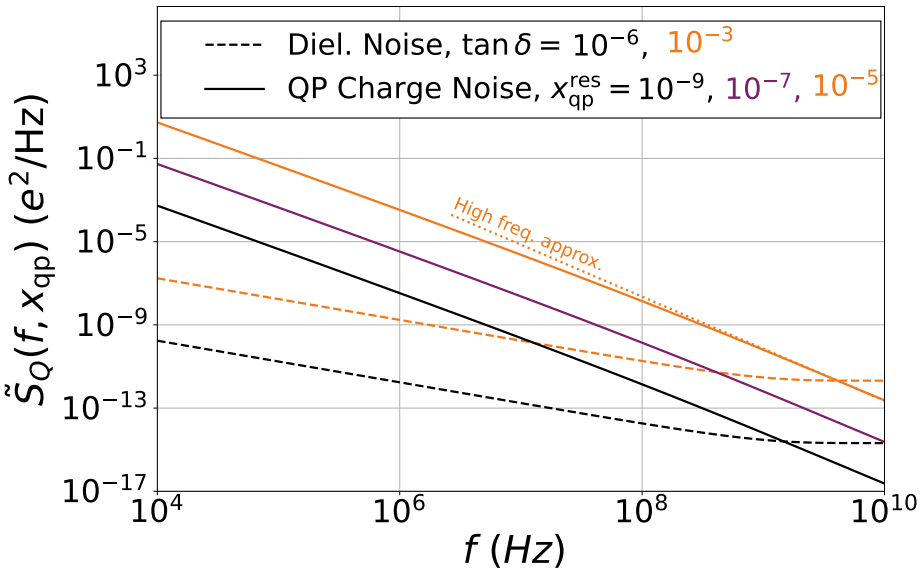

Figure 7.3: ***Charge noise from wire-resident QPs compared to capacitive dielectric loss, ℓ = 1.5 mm.***
Charge noise due to a quasithermal QP distribution (solid lines) in Al devices for 3 values of $x_{\rm qp}^{\rm res}$ from $= 1 \times 10^{-9}$ (black) to 1×10^{-5} (orange) in increments of $\times 10$ compared to dielectric loss (dashed lines) for $\tan\delta = 1 \times 10^{-6}$ (black), 1×10^{-3} (orange). The QP high frequency approximation for $x_{\rm qp}^{\rm res} = 1 \times 10^{-5}$ (dotted line) is shown for comparison. Values used in the calculation: T=40 mK, $\mathcal{C} = 168$ pF/m, ℓ=1.5 mm, A=Wb (flat wire) with W= 6 μm and b= 100 nm the wire's width and thickness.

QPs residing in a SC wire:

$$\tilde{S}_Q(\omega) = \frac{2\hbar A \sigma_1(\omega)}{\ell\omega}\left[n_B(\omega) + 1\right], \tag{7.12}$$

with $n_B(\omega) = 1/(e^{\hbar\omega/(k_BT)} - 1)$ is the Bose-Einstein distribution. At thermal equilibrium ($x_{\rm qp}^{\rm res} = 0$), this contribution is exponentially small at low temperatures, less than $10^{-20}\ e^2/\text{Hz}$ above 1 MHz for T= 40 mK for a coplanar waveguide (CPW) with typical dimensions. However, considering resident QP densities on the order of measured values ($x_{\rm qp}^{\rm res} = 1 \times 10^{-9} - 1 \times 10^{-5}$) [78, 82], the QP charge noise is several orders of magnitude higher: over 15 orders of magnitude larger for $x_{\rm qp}^{\rm res} = 1 \times 10^{-8}$ compared to thermal QPs at 40 mK. $\tilde{S}_Q(\omega) \propto 1/f^2$ for $\hbar\omega \lesssim k_BT$ and $\propto 1/f^{2.5}$ at higher frequencies and is always inversely proportional to the wire length ℓ, this geometric

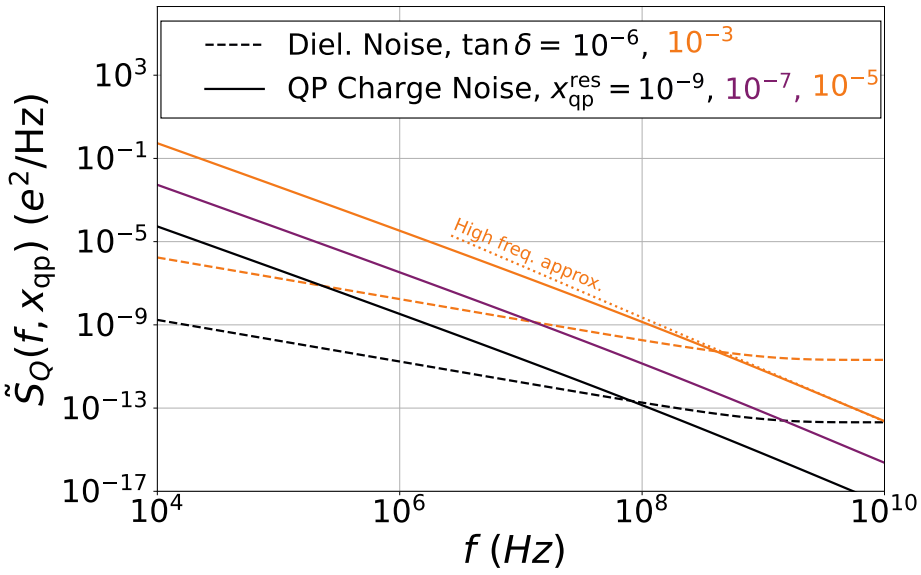

Figure 7.4: ***Charge noise from wire-resident QPs compared to capacitive dielectric loss, ℓ = 15 mm.***
Charge noise due to a quasithermal QP distribution (solid lines) in Al devices for 3 values of $x_{\rm qp}^{\rm res}$ from $= 1 \times 10^{-9}$ (black) to 1×10^{-5} (orange) in increments of $\times 10$ compared to dielectric loss (dashed lines) for $\tan\delta = 1 \times 10^{-6}$ (black), 1×10^{-3} (orange). The QP high frequency approximation for $x_{\rm qp}^{\rm res} = 1 \times 10^{-5}$ (dotted line) is shown for comparison. Values used in the calculation: T=40 mK, $\mathcal{C} = 168$ pF/m, ℓ=15 mm, A=Wb (flat wire) with W= 6 μm and b= 100 nm the wire's width and thickness.

dependence originates from the charge susceptibility being inversely proportional to the wire's impedance.

In order to quantify the impact of this mechanism, it is illustrative to compare it to capacitive dielectric loss, one of the main sources of charge noise in SC circuits. In a capacitor, the charge susceptibility is simply $\tilde{\chi}_Q^{\rm cap}(\omega) = \frac{\langle \delta Q \rangle}{V} = \tilde{C}$, with complex capacitance $\tilde{C} = C + iC\tan\delta$ where C is the real capacitance and the loss tangent $\tan\delta$ is assumed to be due to bulk or surface TLSs in the dielectric material. Following this result and the fluctuation-dissipation theorem, Eq. (A.3), the charge noise is

$$\tilde{S}_Q^{\rm cap}(\omega) = 2\hbar C \tan\delta \left[n_B(\omega) + 1 \right]. \tag{7.13}$$

A possible interpretation of wire-resident QP charge noise is thus dielectric loss with loss tangent

$\tan\delta = \frac{A\sigma_1}{C\ell\omega}$, this interpretation is useful for comparison. Note, however, that the microscopic origin of both mechanisms is fundamentally different: dielectric loss is due to energy absorption by TLSs in the dielectric material; charge noise from wire-resident QPs is due to ohmic loss where electrical energy is turned into heat from the scattering of charge carriers in the SC wire.

We compare both contributions in a typical Al SC CPW. For dielectric loss, we assume a frequency-independent loss tangent and consider two typical values $\tan\delta = 1\times10^{-6}, 1\times10^{-3}$ due to bulk and surface TLSs. We assume the capacitance can be approximated by a zero thickness model [89]. We fix the ratio between the CPW center-strip width to the width of the gap to 1.7 and consider a silicon substrate. The resulting capacitance per unit length is $\mathcal{C} \equiv C/\ell = 168\ \mathrm{pF/m}$. For wire-resident QP charge noise, we take $x_{\mathrm{qp}}^{\mathrm{res}} = 1\times10^{-9} - 1\times10^{-5}$. These results are shown in Fig. 7.3 for a SC CPW of length ℓ = 1.5 mm, in the calculations, we used Eq. (7.1) to numerically calculate charge noise from resident QPs assuming a quasithermal distribution. QP charge noise dominates at low frequencies ($f \lesssim 1$ GHz for $x_{\mathrm{qp}}^{\mathrm{res}} = 1\times10^{-7}$). For comparison, we also show the high-frequency approximation where we took Eq. (7.8) for calculating $\sigma_1(\omega)$. Fig. 7.4 shows the same results for a wire 10 times longer, showing the wire length dependence on charge noise. QP noise (dielectric loss) decreases (increases) linearly with wire length for a constant capacitance per unit length $\mathcal{C}$.

7.3.4 Flux Noise

We can also estimate the flux noise contribution due to this mechanism noting that it is related to charge noise by $\tilde{S}_\Phi(\omega) = (L\omega)^2\tilde{S}_Q(\omega)$ where L is the wire's inductance, this flux noise can be understood as flux fluctuations generated by the current fluctuations from the presence of QPs in the wire. The flux noise due to wire-resident QPs is thus

$$\tilde{S}_\Phi(\omega) = 2\hbar\omega\mathcal{L}^2 A\ell\sigma_1\left[n_B(\omega)+1\right], \tag{7.14}$$

with $\mathcal{L} \equiv L/\ell$ the wire's inductance per unit length, note that $\tilde{S}_\Phi(\omega) \propto \ell$, showing an inverse geometric dependence with respect to charge noise.

Considering a quasithermal QP distribution, $\tilde{S}_\Phi(\omega)$ is logarithmic at low frequencies and $\propto 1/\sqrt{f}$ at higher frequencies, this follows from Eqs. (7.7), (7.8). This logarithmic flux noise at low frequencies can be interpreted as "nearly white noise" in narrow frequency intervals. Luthi

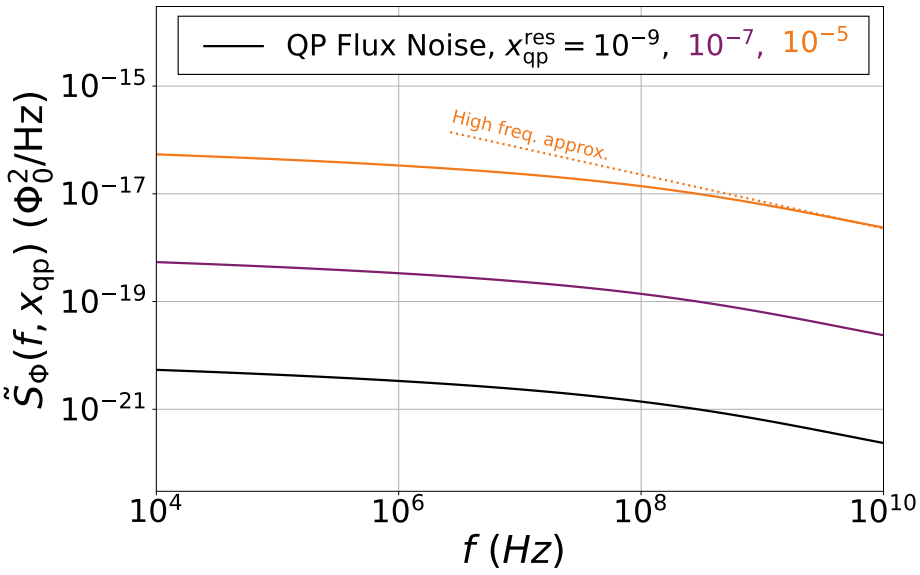

Figure 7.5: ***Flux noise from wire-resident QPs, ℓ = 1.5 mm.***
Flux noise due to quasithermal QPs (solid lines) in Al devices for 3 values of x_{qp}^{res} from $= 1 \times 10^{-9}$ (black) to 1×10^{-5} (orange) in increments of $\times 10$. The QP high frequency approximation for $x_{qp}^{res} = 1 \times 10^{-5}$ (dotted line) is shown for comparison. Values used in the calculation: T=40 mK, $\mathcal{L} = 420$ nH/m, ℓ=1.5 mm, A=Wb (flat wire) with W= 6 μm and b= 100 nm the wire's width and thickness.

et al. (Ref. [86]) observed a white flux noise background of $3.6 \times 10^{-15}\ \Phi_0^2/\mathrm{Hz}$ of unknown origin in a NbTiN SQUID loop of about $\ell \approx 100\ \mu\mathrm{m}$, a background of this amplitude can be explained by flux noise produced by a normalized quasithermal QP density of $x_{qp}^{res} \approx 1 \times 10^{-6}$. Therefore, this mechanism suggests a possible explanation of white flux noise observed in experiments. Numerical calculations show a flux noise contribution of $1 \times 10^{-21} - 1 \times 10^{-16}\ \Phi_0^2/\mathrm{Hz}$ for $x_{qp}^{res} = 1 \times 10^{-9} - 1 \times 10^{-5}$ in an Al CPW of $\ell = 1.5$ mm with an inductance per unit length $\mathcal{L} = 420\ \mathrm{nH/m}$ (same device as in Fig. 7.3), results shown in Fig. 7.5. Quintana et al. (Ref. [48]) measured a $1/f$ to ohmic flux noise dependence of comparable amplitudes in frequencies 10 MHz - 1GHz in a device of similar dimensions, although the qualitative behavior isn't explained by this mechanism, it demonstrates that a flux noise background produced by a quasithermal QP distribution can be a relevant limiting factor in these devices.

7.4 Conclusions

This chapter presents a theory of noise produced by non-equilibrium densities of wire-resident QPs in SC devices. The mechanism of wire-resident QPs differs fundamentally from the traditional QP tunneling mechanism typically considered in SC qubits. QP tunneling involves QPs crossing Josephson junctions, which leads to decoherence and energy dissipation in the qubit. This process is well-studied and often linked to the quality and design of the Josephson junctions themselves.

In contrast, wire-resident QPs are confined within the SC wires and do not involve tunneling through junctions. Instead, these QPs can contribute to noise through their interactions with the SC condensate and other QPs within the wire. This distinction is significant because it highlights a different source of noise that can affect the qubit performance, independent of the Josephson junctions.

By assuming a quasithermal QP distribution, our theoretical model indicates that wire-resident QPs can significantly impact charge noise levels, particularly at intermediate frequencies, and provide a nearly white flux noise background. These findings are consistent with experimental observations and suggest that this mechanism is relevant in understanding noise in SC devices.

CHAPTER 8

Conclusions

Superconducting (SC) qubits represent a promising pathway toward scalable quantum computing, leveraging the coherence of macroscopic quantum states [4]. A pivotal factor in their operational efficacy is maintaining quantum coherence, a challenge compounded by various decoherence mechanisms such as flux noise, dielectric loss, and SC quasiparticles (QPs). The theoretical work presented in this dissertation aims to elucidate the properties of known mechanisms responsible for flux and charge noise in SC devices. The research includes an extensive theory of flux noise due to a general model of spin dissipation (diffusion plus relaxation) and a theory of charge and flux noise due to the presence of non-equilibrium densities of wire-resident SC QPs.

Several experiments in SQUID-based devices [8, 48, 55, 74, 75, 90] have concluded that flux noise follows the empirical law

$$\tilde{S}_\Phi(\omega) = \frac{A_\Phi^2}{\omega^\alpha}, \tag{8.1}$$

where amplitude A_Φ and exponent $\alpha \leq 1$ are both temperature-dependent.

Chapter 4 presents a general theory of flux noise due to spin dissipation that is able to calculate A_Φ and α for a realistic model of impurity spins with disorder due to vacancies and wide distributions of spin relaxation rates, and for spins confined in bounded regions such as SC wires. To achieve this we developed a method that does not rely on the "third-principles" diffusion operator $D\nabla^2$. Our "second-principles" method instead assumes lattice sites are coupled by a dissipation matrix D_{ij}. We showed that this choice obeys fundamental principles such as total spin conservation and the second law of thermodynamics. Our prescription for D_{ij} depends on spin Hamiltonian parameters such as exchange interaction, establishing a direct connection be-

tween flux noise and model spin Hamiltonians. This framework also allows for energy exchange between the spins and other degrees of freedom like phonons and amorphous TLSs modeled as relaxation terms Γ_is.

Chapter 5 presents results focused on a spin-lattice relaxation model. The model is based on the assumption that the interaction between each impurity spin and the vibrational modes of the lattice, formed by amorphous TLSs and phonons, dominate finite frequency fluctuations. An analytical expression for the flux noise in the presence of an external magnetic field B is obtained, revealing a transition from $1/\omega$ flux noise at B=0 to Lorentzian flux noise at $B > 0$ in the frequency range where direct spin relaxation by phonon emission is stronger than cross relaxation due to amorphous TLSs. Fitting the current theory to experimental data will yield the characteristic exponent n for direct phonon emission (spin-lattice relaxation $\Gamma_i \propto B^n$), elucidating whether the mechanism is mediated by spin-orbit coupling or hyperfine interaction. This will in turn yield valuable information on the identity of the spins causing flux noise.

The model predicts that application of a B field reduces low frequency noise arising from $\boldsymbol{F}_j \parallel \boldsymbol{B}$ ($\boldsymbol{F}_j \perp \boldsymbol{B}$) by a factor of $1/\cosh^2(g\mu_B B/2k_B T)$ ($\tanh(g\mu_B B/2k_B T)/(2g\mu_B B)$). It also shifts the contribution of $\boldsymbol{F}_j \perp \boldsymbol{B}$ out of the low frequency range, transferring noise to spin precession peaks centered at $\omega = \pm g\mu_B B/\hbar$. For $T = 10$ mK and $B = 100$ G, $1/\cosh^2(g\mu_B B/2k_B T) \approx 2/3$, and approximately one half of the total noise power will be transferred to a higher frequency band. Therefore, a total reduction of $\approx 1/3$ is made to the noise power in the low frequency band. Further reduction can be achieved for $B > 100$ G. These results show that an external magnetic field can be used to reduce the impact of flux noise in qubits.

Chapter 6 shows numerical results for the developed theory, including spin-lattice relaxation and spin-spin interactions. We showed that choosing D_{ij} consistent with $D\nabla^2$ (third-principles theory) and assuming an infinite, translation-invariant spin system leads to temperature-independent noise exponent $\alpha = 1/2$, in contradiction to experiments. In contrast, numerical calculations with the "second principles" prescription for D_{ij} even in an infinite magnet predict a temperature-dependent exponent α. Based on these results we propose a phenomenological expression, Eq. 6.37, that describes accurately the frequency and temperature dependence of numerical calculations of flux noise and agrees with experimental observations. Furthermore, we show how confinement and disorder due to vacancies and a wide distribution of relaxation rates have an impact in the numerical value of α. More experimental data will confirm if this

model correctly describes the temperature dependence of flux noise in SC devices.

A central concept of the theory is the interpretation of flux noise in terms of (para)magnon excitations. Flux noise is directly related to the density of edge (para)magnons, which leads to fluctuations at the SC wire edges, where spin flips cause the largest flux changes to the device. While D_{ij} accounts for the interactions between (para)magnons, the rates Γ_i describe interactions between spins and other degrees of freedom, such as phonons, electron gas excitations, and TLS defects.

In addition to low-frequency flux noise, experiments also measure Ohmic ($\propto \omega$) [91] or super-Ohmic ($\propto \omega^3$) [48, 90] flux noise in the GHz range. We argue that this behaviour can not arise from spin dissipation alone. Our theory is fundamentally based on the assumption of "hydrodynamics", i.e. that spin degrees of freedom can be described by the classical equation of motion (4.20) [92]. As a result, it overestimates the noise for $\omega > \Omega_c$, where Ω_c is a high-frequency cut-off. The cut-off Ω_c can be estimated from exact calculations of the moments of the noise spectrum at $T \to \infty$. Calculations for the 3d Heisenberg model [64] suggests $\hbar\Omega_c \sim 10J/\hbar$ for our 2d case. When $\omega > \Omega_c$, $\tilde{S}_{ij}(\omega)$ drops off faster than $1/\omega^2$, so that our Eq. (6.10) becomes an upper bound for flux noise. In Eq. (6.13), this upper bound was shown to be $\propto 1/\omega$ when quantum noise is included. As the $1/\omega$ upper bound holds for all interacting spin models, this allows us to conclude that the high-frequency Ohmic [91], or super-Ohmic [48, 90] flux noise observed in SQUIDs *can not originate from a model of impurity spin dissipation*.

We can separate experiments into two groups: experiments performed in niobium (Nb) and aluminum (Al) devices. Measurements in Nb devices show both amplitude $A_\Phi(T)$ and exponent α decreasing with increasing T as shown in Fig. 3.5. According to our theory, this $A_\Phi(T)$ requires a FM model ($J > 0$). The calculated $\alpha(T)$ for $\Gamma_i = 0$ ranges from 0.8 at low T to 0.6 at high T for a confined system (spins only on top of the wire) with a small number of vacancies ($\sigma \lesssim 1$), but the exponent can approach 0.5 when the spin system extends beyond the wire as in the homogeneous approximation (HA). In comparison, experimental measurement shows $\alpha(T)$ going from 0.8 to 0.4 with increasing T [55]. Therefore, a nearest-neighbour (NN) Heisenberg model with $J > 0$ and $\sigma \lesssim 1$ and low $\Gamma_i \ll J/\hbar$ provides a reasonable model.

Experiments in Al devices show that $A_\Phi(T)$ and $\alpha(T)$ are qualitatively different from niobium. In Fig. 3.3, $A(T)$ is shown to increase with T, based on our theory, an AFM model ($J < 0$) is required. The authors reached the same conclusion by measuring asymmetric noise

$\tilde{S}_{\Phi}^{-}(\omega)$ and extrapolating to $T < 0$ to get $T_{\mathrm{CW}} = -10$ mK. According to our interpretation this implies $\sigma J/k_B = -10$ mK. The measured exponent $\alpha = 0.96 - 1.05$ can not be explained by our theory with $\Gamma_i = 0$. However, by introducing a wide distribution of Γ_i's makes $\alpha \approx 1$ at low temperatures. A recent experiment also observed a $1/f$ to lorentzian flux noise with increasing magnetic field [53], this behaviour is consistent qualitatively with our spin-lattice model with the inclusion of field-dependent direct relaxation. Although the transition from $1/f$ to lorentzian flux noise is predicted by our model, the apparent increase in amplitude with magnetic field at low frequencies is not (Fig. 3.4a), this behaviour remains an open question and could be due to other mechanisms like a B field-dependent dielectric loss [93]. On the other hand, the decrease in amplitude with magnetic field at higher frequencies is consistent with our model (Fig. 3.4b). This indicates that a model based on independent spins with spin relaxation Γ_i is more suitable for describing flux noise in Al devices. This is true even though the impact of spin-spin interactions such as dipolar and exchange can still be observed as a Curie-Weiss temperature T_{CW} in the zero-frequency susceptibility because decay rates Γ_1, Γ_2 do not impact $\tilde{\chi}_{zz}(0)$. Thus one can use $\tilde{\chi}_{zz}(0) = 1/[4k_B(T - T_{\mathrm{CW}})\cosh^2(g\mu_B B/2k_B T)]$ in Eq. (5.24) to model spin-spin interactions. Measurements of $\alpha(T)$ over a wide temperature range in Al devices are not yet available to confirm the extension and validity of this model.

Chapter 7 presents a theory of charge and flux noise due to non-equilibrium densities of wire-resident QPs. The mechanism of wire-resident QPs differs fundamentally from the traditional QP tunneling mechanism typically considered in SC qubits. QP tunneling involves QPs crossing Josephson junctions, which leads to decoherence and energy dissipation in the qubit. In contrast, wire-resident QPs are confined within the SC wires and do not involve tunneling through junctions. Instead, these QPs can contribute to noise through their interactions with the SC condensate and other QPs within the wire.

It's shown that resident QPs in a SC wire can notably contribute to charge noise at intermediate frequencies when compared to dielectric loss stemming from TLSs. This contribution could become more relevant as losses from surface TLSs continue to be reduced by better materials and circuit designs [94, 95]. This mechanism is predicted to be particularly important in shorter wires due to its geometric dependence. Our model shows that wire-resident QPs can explain the origin of the white flux noise background observed in experiments [86]. The magnitudes of flux noise predicted by our model are found to be comparable to those empirically measured in

certain devices [48].

In conclusion, we developed a "second principles" theory of flux noise due to spin dissipation that is able to account for the confinement and disorder present in realistic impurity spin systems on SC devices. The theoretical framework allows explicit prediction of the amplitude and exponent of flux noise due to different wire geometries and spin disorder scenarios, such as random vacancies and wide distributions of spin-flip rates due to interactions with amorphous TLSs and phonons. Comparing numerical results to experiments allowed us to specify different spin Hamiltonians for Nb and Al devices. While the underlying reasons for this difference are not understood, the empirical success of each model in describing its respective material suggests that the impurity species contributing to flux noise are qualitatively different in these two materials, warranting further investigation into their identity.

We have also extended the theory for the impact of QPs in SC devices beyond the widely examined case of QP tunneling through Josephson junctions to address the often-overlooked dynamics of QPs within SC wires. This proposed mechanism predicts a significant contribution to both charge and flux noise in SC devices, which can be particularly relevant for SC devices without junctions, such as resonators and transmission lines.

Future research should focus on further experimental validation of the proposed models. Measuring the temperature dependence and spin-density dependence of flux noise exponent α in Al devices could shed light on the underlying reasons for the observed discrepancies between Al and Nb devices. Similarly, more experiments investigating the impact of magnetic fields on the coherence of SC qubits could provide insights into the nature and identity of the magnetic impurities affecting these devices, more theoretical work is also needed in this area, as current models are insufficient to describe the impact of magnetic fields on noise in these systems. Furthermore, quantifying the frequency dependence of loss in QP-poisoned SC wires could confirm the impact of wire-resident QPs in these devices.

Bibliography

[1] José Alberto Nava Aquino and Rogério de Sousa. Flux noise in disordered spin systems. *Phys. Rev. B.*, 106:144506, October 2022. URL https://doi.org/10.1103/PhysRevB.106.144506.

[2] José Alberto Nava Aquino and Rogério de Sousa. Model for 1/f flux noise in superconducting aluminum devices: Impact of external magnetic fields. *Applied Physics Letters*, 122 (22):224003, 06 2023. URL https://doi.org/10.1063/5.0147500.

[3] José Alberto Nava Aquino and Rogério de Sousa. Charge and flux noise from nonequilibrium quasiparticle energy distributions in superconducting wires, 2024. URL https://doi.org/10.48550/arXiv.2407.21177.

[4] J. Clarke and F. Wilhelm. Superconducting quantum bits. *Nature*, 453:1031, 2008. URL https://doi.org/10.1038/nature07128.

[5] R. H. Koch, D. P. DiVincenzo, and J. Clarke. Model for $1/f$ flux noise in squids and qubits. *Phys. Rev. Lett.*, 98:267003, 2007. URL https://doi.org/10.1103/PhysRevLett.98.267003.

[6] R. de Sousa. Dangling-bond spin relaxation and magnetic $1/f$ noise from the amorphous-semiconductor/oxide interface: Theory. *Phys. Rev. B*, 76:245306, 2007. URL http://doi.org/10.1103/PhysRevB.76.245306.

[7] S. Sendelbach, D. Hover, A. Kittel, M. Mück, J. M. Martinis, and R. McDermott. Magnetism in SQUIDs at Millikelvin Temperatures. *Phys. Rev. Lett.*, 100:227006, 2008. URL https://doi.org/10.1103/PhysRevLett.100.227006.

[8] T. Lanting, M. H. Amin, A. J. Berkley, C. Rich, S.-F. Chen, S. LaForest, and R. de Sousa. Evidence for temperature-dependent spin diffusion as a mechanism of intrinsic flux noise

in SQUIDs. *Phys. Rev. B*, 89:014503, 2014. URL http://doi.org/10.1103/PhysRevB.89.014503.

[9] J. M. Martinis et al. Decoherence in josephson qubits from dielectric loss. *Phys. Rev. Lett.*, 95:210503, 2005. URL https://doi.org/10.1103/PhysRevLett.95.210503.

[10] J. Gao et al. A semiempirical model for two-level system noise in superconducting microresonators. *Appl. Phys. Lett.*, 92:212504, 2008. URL https://doi.org/10.1063/1.2937855.

[11] R. M. Lutchyn, L. I. Glazman, and A. I. Larkin. Kinetics of the superconducting charge qubit in the presence of a quasiparticle. *Phys. Rev. B*, 74:064515, Aug 2006. doi: 10.1103/PhysRevB.74.064515. URL https://link.aps.org/doi/10.1103/PhysRevB.74.064515.

[12] John M. Martinis, M. Ansmann, and J. Aumentado. Energy decay in superconducting josephson-junction qubits from nonequilibrium quasiparticle excitations. *Phys. Rev. Lett.*, 103:097002, Aug 2009. doi: 10.1103/PhysRevLett.103.097002. URL https://link.aps.org/doi/10.1103/PhysRevLett.103.097002.

[13] G. Catelani, R. J. Schoelkopf, M. H. Devoret, and L. I. Glazman. Relaxation and frequency shifts induced by quasiparticles in superconducting qubits. *Phys. Rev. B*, 84:064517, Aug 2011. doi: 10.1103/PhysRevB.84.064517. URL https://link.aps.org/doi/10.1103/PhysRevB.84.064517.

[14] M. Tinkham. *Introduction to Superconductivity*. Dover Publications, Garden City, New York, 1996. ISBN 0486435032.

[15] Pierre-Gilles de Gennes and Paul A. Pincus. *Superconductivity of Metals and Alloys*. Westview Press, Boulder, CO, 1st edition, 1999. ISBN 978-0201416259.

[16] Charles Kittel. *Introduction to Solid State Physics*. Wiley, 2005.

[17] Alexandre Blais, Arne L. Grimsmo, S. M. Girvin, and Andreas Wallraff. Circuit quantum electrodynamics. *Rev. Mod. Phys.*, 93:025005, May 2021. doi: 10.1103/RevModPhys.93.025005. URL https://link.aps.org/doi/10.1103/RevModPhys.93.025005.

[18] P. Krantz, M. Kjaergaard, F. Yan, T. P. Orlando, S. Gustavsson, and W. D. Oliver. A quantum engineer's guide to superconducting qubits. *Appl. Phys. Rev*, 6:021318, 2019. URL https://doi.org/10.1063/1.5089550.

[19] M. H. Devoret, A. Wallraff, and J. M. Martinis. Superconducting Qubits: A Short Review. *arXiv e-prints*, art. cond-mat/0411174, November 2004. doi: 10.48550/arXiv.cond-mat/0411174. URL https://doi.org/10.48550/arXiv.cond-mat/0411174.

[20] Yuriy Makhlin, Gerd Schön, and Alexander Shnirman. Quantum-state engineering with josephson-junction devices. *Rev. Mod. Phys.*, 73:357–400, May 2001. doi: 10.1103/RevModPhys.73.357. URL https://link.aps.org/doi/10.1103/RevModPhys.73.357.

[21] K. Onnes. *Leiden Comm.*, 120b, 122b, 124c, 1911.

[22] J. Bardeen, L. N. Cooper, and J. R. Schrieffer. Theory of Superconductivity. *Phys. Rev.*, 108: 1175, 1957. URL https://doi.org/10.1103/PhysRev.108.1175.

[23] Meissner effect. Meissner effect. https://en.wikipedia.org/wiki/Meissner_effect, April 30 2024. Accessed: 2024-06-16.

[24] F. London and H. London. The electromagnetic equations of the supraconductor. *Proc. Roy. Soc.*, A149:71, 1935. URL https://doi.org/10.1098/rspa.1935.0048.

[25] V. L. Ginzburg and L. D. Landau. *Zh. Eksperim. i Teor. Fiz*, 20:1064, 1950.

[26] B. D. Josephson. Possible new effects in superconductive tunnelling. *Phys. Lett.*, 1:251, 1962. URL https://doi.org/10.1016/0031-9163(62)91369-0.

[27] Josephson effect. Josephson effect. https://en.wikipedia.org/wiki/Josephson_effect, May 1 2024. Accessed: 2024-06-16.

[28] R. Blatt and C Roos. Quantum simulations with trapped ions. *Nature Phys*, 8:277, 2012. URL https://doi.org/10.1038/nphys2252.

[29] T. B. Pittman, M. J. Fitch, B. C Jacobs, and J. D. Franson. Experimental controlled-not logic gate for single photons in the coincidence basis. *Phys. Rev. A*, 68:032316, 2003. URL https://doi.org/10.1103/PhysRevA.68.032316.

[30] R. de Sousa, J. D. Delgado, and S. Das Sarma. Silicon quantum computation based on magnetic dipolar coupling. *Phys. Rev. A*, 70:052304, 2004. URL https://doi.org/10.1103/PhysRevA.70.052304.

[31] A. Imamoglu, D. D. Awschalom, G. Burkard, D. P. DiVincenzo, D. Loss, M. Sherwin, and A. Small. Quantum information processing using quantum dot spins and cavity qed. *Phys. Rev. Lett.*, 83:4204, 1999. URL https://doi.org/10.1103/PhysRevLett.83.4204.

[32] Reprinted figure with permission from Alexandre Blais, Arne L. Grimsmo, S. M. Girvin, and Andreas Wallraff. Circuit quantum electrodynamics. *Rev. Mod. Phys.*, 93:025005, May 2021. doi: 10.1103/RevModPhys.93.025005. URL https://link.aps.org/doi/10.1103/RevModPhys.93.025005 , Copyright 2024 by the American Physical Society.

[33] Jens Koch, Terri M. Yu, Jay Gambetta, A. A. Houck, D. I. Schuster, J. Majer, Alexandre Blais, M. H. Devoret, S. M. Girvin, and R. J. Schoelkopf. Charge-insensitive qubit design derived from the cooper pair box. *Phys. Rev. A*, 76:042319, Oct 2007. doi: 10.1103/PhysRevA.76.042319. URL https://link.aps.org/doi/10.1103/PhysRevA.76.042319.

[34] M. D. Hutchings, J. B. Hertzberg, Y. Liu, N. T. Bronn, G. A. Keefe, Markus Brink, Jerry M. Chow, and B. L. T. Plourde. Tunable superconducting qubits with flux-independent coherence. *Phys. Rev. Appl.*, 8:044003, Oct 2017. doi: 10.1103/PhysRevApplied.8.044003. URL https://link.aps.org/doi/10.1103/PhysRevApplied.8.044003.

[35] José M. Chávez-Garcia, Firat Solgun, Jared B. Hertzberg, Oblesh Jinka, Markus Brink, and Baleegh Abdo. Weakly flux-tunable superconducting qubit. *Phys. Rev. Appl.*, 18:034057, Sep 2022. doi: 10.1103/PhysRevApplied.18.034057. URL https://link.aps.org/doi/10.1103/PhysRevApplied.18.034057.

[36] T. P. Orlando, J. E. Mooij, L. Tian, C. H. van der Wal, L. S. Levitov, S. Lloyd, and J. J. Mazo. Superconducting persistent-current qubit. *Physical Review B*, 60:15398–15413, 1999. URL https://doi.org/10.1103/PhysRevB.60.15398.

[37] J. E. Mooij, T. P. Orlando, L. Levitov, L. Tian, C. H. van der Wal, and S. Lloyd. Josephson persistent-current qubit. *Science*, 285(5430):1036–1039, 1999. doi: 10.1126/science.285.5430.1036. URL https://www.science.org/doi/10.1126/science.285.5430.1036.

[38] Reprinted from J. Clarke and F. Wilhelm. Superconducting quantum bits. *Nature*, 453:1031, 2008. URL https://doi.org/10.1038/nature07128 , with the permission of Springer Nature Publishing.

[39] Vladimir E. Manucharyan, Jens Koch, Leonid I. Glazman, and Michel H. Devoret. Fluxonium: Single cooper-pair circuit free of charge offsets. *Science*, 326(5949):113–116, 2009. URL https://www.science.org/doi/abs/10.1126/science.1175552.

[40] Yen-Hsiang Lin, Long B. Nguyen, Nicholas Grabon, Jonathan San Miguel, Natalia Pankratova, and Vladimir E. Manucharyan. Demonstration of protection of a superconducting qubit from energy decay. *Phys. Rev. Lett.*, 120:150503, 2018. URL https://link.aps.org/doi/10.1103/PhysRevLett.120.150503.

[41] Reprinted from P. Krantz, M. Kjaergaard, F. Yan, T. P. Orlando, S. Gustavsson, and W. D. Oliver. A quantum engineer's guide to superconducting qubits. *Appl. Phys. Rev*, 6:021318, 2019. URL https://doi.org/10.1063/1.5089550 , with the permission of AIP Publishing.

[42] Rogerio de Sousa. *Electron Spin as a Spectrometer of Nuclear-Spin Noise and Other Fluctuations*, pages 183–220. Springer Berlin Heidelberg, Berlin, Heidelberg, 2009. ISBN 978-3-540-79365-6. doi: 10.1007/978-3-540-79365-6_10. URL https://doi.org/10.1007/978-3-540-79365-6_10.

[43] C. P. Slichter. *Principles of Magnetic Resonance*. Springer Berlin, Heidelberg, 1963. ISBN 978-3-662-09441-9. URL https://doi.org/10.1007/978-3-662-09441-9.

[44] John M. Martinis, S. Nam, J. Aumentado, K. M. Lang, and C. Urbina. Decoherence of a superconducting qubit due to bias noise. *Phys. Rev. B*, 67:094510, Mar 2003. doi: 10.1103/PhysRevB.67.094510. URL https://link.aps.org/doi/10.1103/PhysRevB.67.094510.

[45] L. Faoro and L. B. Ioffe. Microscopic origin of low-frequency flux noise in Josephson circuits. *Phys. Rev. Lett.*, 100:227005, 2008. URL http://doi.org/10.1103/PhysRevLett.100.227005.

[46] P. Kumar, S. Sendelbach, M. A. Beck, J. W. Freeland, Z. Wang, H. Wang, C. C. Yu, R. Q. Wu, D. P. Pappas, and R. McDermott. Origin and Reduction of $1/f$ Magnetic Flux Noise in

Superconducting Devices. *Phys. Rev. Appl.*, 6:041001(R), 2016. URL https://doi.org/10.1103/PhysRevApplied.6.041001.

[47] S. E. de Graaf, A. A. Adamyan, T. Lindström, D. Erts, S. E. Kubatkin, A. Ya Tzalenchuk, and A. V. Danilov. Direct Identification of Dilute Surface Spins on Al_2O_3: Origin of Flux Noise in Quantum Circuits. *Phys. Rev. Lett.*, 118:057703, 2017. URL http://doi.org/10.1103/PhysRevLett.118.057703.

[48] C. M. Quintana, Y. Chen, D. Sank, A. G. Petukhov, T. C. White, D. Kafri, B. Chiaro, A. Megrant, R. Barends, B. Campbell, Z. Chen, A. Dunsworth, A. G. Fowler, R. Graff, E. Jeffrey, J. Kelly, E. Lucero, J. Y. Mutus, M. Neeley, C. Neill, P. J. J. O'Malley, P. Roushan, A. Shabani, V. N. Smelyanskiy, A. Vainsencher, J. Wenner, H. Neven, and J. M. Martinis. Observation of Classical-Quantum Crossover of $1/f$ Flux Noise and Its Paramagnetic Temperature Dependence. *Phys. Rev. Lett.*, 118:057702, 2017. URL http://doi.org/10.1103/PhysRevLett.118.057702.

[49] T. Lanting, M. H. Amin, C. Baron, M. Babcock, J. Boschee, S. Boixo, V. N. Smelyanskiy, M. Foygel, and A. G. Petukhov. Probing Environmental Spin Polarization with Superconducting Flux Qubits. URL https://arxiv.org/abs/2003.14244.

[50] S. Choi, Lee D. H., Louie S. G., and Clarke J. Localization of Metal-Induced Gap States at the Metal-Insulator Interface: Origin of Flux Noise in SQUIDs and Superconducting Qubits. *Phys. Rev. Lett.*, 103:197001, 2009. URL http://doi.org/10.1103/PhysRevLett.103.197001.

[51] S. LaForest and R. de Sousa. Flux-vector model of spin noise in superconducting circuits: Electron versus nuclear spins and role of phase transition. *Phys. Rev. B*, 92(5):054502, 2015. URL http://doi.org/10.1103/PhysRevB.92.054502.

[52] Reprinted figure with permission from C. M. Quintana, Y. Chen, D. Sank, A. G. Petukhov, T. C. White, D. Kafri, B. Chiaro, A. Megrant, R. Barends, B. Campbell, Z. Chen, A. Dunsworth, A. G. Fowler, R. Graff, E. Jeffrey, J. Kelly, E. Lucero, J. Y. Mutus, M. Neeley, C. Neill, P. J. J. O'Malley, P. Roushan, A. Shabani, V. N. Smelyanskiy, A. Vainsencher, J. Wenner, H. Neven, and J. M. Martinis. Observation of Classical-Quantum Crossover of $1/f$ Flux

Noise and Its Paramagnetic Temperature Dependence. *Phys. Rev. Lett.*, 118:057702, 2017. URL http://doi.org/10.1103/PhysRevLett.118.057702 , Copyright 2024 by the American Physical Society.

[53] D. A. Rower, L. Ateshian, L. H. Li, M. Hays, D. Bluvstein, L. Ding, B. Kannan, A. Almanakly, J. Braumüller, D. K. Kim, A. Melville, B. M. Niedzielski, M. E. Schwartz, J. L. Yoder, T. P. Orlando, J. I. Wang, S. Gustavsson, J. A. Grover, R. Serniak, K. Comin, and W. D. Oliver. Evolution of $1/f$ Flux Noise in Superconducting Qubits with Weak Magnetic Fields. *Phys. Rev. Lett.*, 130:220602, May 2023. URL https://doi.org/10.1103/PhysRevLett.130.220602.

[54] Reprinted figure with permission from D. A. Rower, L. Ateshian, L. H. Li, M. Hays, D. Bluvstein, L. Ding, B. Kannan, A. Almanakly, J. Braumüller, D. K. Kim, A. Melville, B. M. Niedzielski, M. E. Schwartz, J. L. Yoder, T. P. Orlando, J. I. Wang, S. Gustavsson, J. A. Grover, R. Serniak, K. Comin, and W. D. Oliver. Evolution of $1/f$ Flux Noise in Superconducting Qubits with Weak Magnetic Fields. *Phys. Rev. Lett.*, 130:220602, May 2023. URL https://doi.org/10.1103/PhysRevLett.130.220602 , Copyright 2024 by the American Physical Society.

[55] S. M. Anton, J. S. Birenbaum, S. R. O'Kelley, V. Bolkhovsky, D. A. Braje, G. Fitch, M. Neeley, G. C. Hilton, H.-M. Cho, K. D. Irwin, F. C. Wellstood, W. D. Oliver, A. Shnirman, and John Clarke. Magnetic flux noise in dc squids: Temperature and geometry dependence. *Phys. Rev. Lett.*, 110:147002, Apr 2013. doi: 10.1103/PhysRevLett.110.147002. URL https://link.aps.org/doi/10.1103/PhysRevLett.110.147002.

[56] Reprinted figure with permission from S. M. Anton, J. S. Birenbaum, S. R. O'Kelley, V. Bolkhovsky, D. A. Braje, G. Fitch, M. Neeley, G. C. Hilton, H.-M. Cho, K. D. Irwin, F. C. Wellstood, W. D. Oliver, A. Shnirman, and John Clarke. Magnetic flux noise in dc squids: Temperature and geometry dependence. *Phys. Rev. Lett.*, 110:147002, Apr 2013. doi: 10.1103/PhysRevLett.110.147002. URL https://link.aps.org/doi/10.1103/PhysRevLett.110.147002 , Copyright 2024 by the American Physical Society.

[57] Rogerio de Sousa, K. Birgitta Whaley, Frank K. Wilhelm, and Jan von Delft. Ohmic and step noise from a single trapping center hybridized with a fermi sea. *Phys. Rev. Lett.*, 95:

247006, Dec 2005. doi: 10.1103/PhysRevLett.95.247006. URL https://link.aps.org/doi/10.1103/PhysRevLett.95.247006.

[58] Clemens Müller, Jared H Cole, and Jürgen Lisenfeld. Towards understanding two-level-systems in amorphous solids: insights from quantum circuits. *Reports on Progress in Physics*, 82(12):124501, oct 2019. doi: 10.1088/1361-6633/ab3a7e. URL https://dx.doi.org/10.1088/1361-6633/ab3a7e.

[59] Igor Diniz and Rogério de Sousa. Intrinsic photon loss at the interface of superconducting devices. *Phys. Rev. Lett.*, 125:147702, Oct 2020. doi: 10.1103/PhysRevLett.125.147702. URL https://link.aps.org/doi/10.1103/PhysRevLett.125.147702.

[60] C. Wang, C. Axline, Y. Y. Gao, T. Brecht, Y. Chu, L. Frunzio, M. H. Devoret, and R. J. Schoelkopf. Surface participation and dielectric loss in superconducting qubits. *Applied Physics Letters*, 107(16):162601, 10 2015. ISSN 0003-6951. doi: 10.1063/1.4934486. URL https://doi.org/10.1063/1.4934486.

[61] G. Catelani, J. Koch, L. Frunzio, R. J. Schoelkopf, M. H. Devoret, and L. I. Glazman. Quasiparticle relaxation of superconducting qubits in the presence of flux. *Phys. Rev. Lett.*, 106:077002, Feb 2011. URL https://link.aps.org/doi/10.1103/PhysRevLett.106.077002.

[62] C. Bell, S. Milikisyants, M. Huber, and J. Aarts. Spin Dynamics in a Superconductor-Ferromagnet Proximity System. *Phys. Rev. Lett.*, 100:047002, Feb 2008. URL http://doi.org/10.1103/PhysRevLett.100.047002.

[63] Belli M. and R. de Sousa. Probing two-level systems with electron spin inversion recovery of defects at the Si/SiO_2 interface. *Phys. Rev. Res.*, 2:033507, 2020. URL http://doi.org/10.1103/physrevresearch.2.033507.

[64] P. G. de Gennes. Inelastic magnetic scattering of neutrons at high temperatures. *J. Phys. Chem. Solids*, 4:223, 1958. URL http://doi.org/10.1016/0022-3697(58)90120-3.

[65] H. S. Bennett and P. C. Martin. Spin Diffusion in the Heisenberg Paramagnet. *Phys. Rev.*, 138:A608, 1965. URL http://doi.org/10.1103/PhysRev.138.A608.

[66] S. Beairsto, M. Cazayous, R. S. Fishman, and R. de Sousa. Confined Magnons. *Phys. Rev. B*, 104:134415, 2021. URL http://doi.org/10.1103/PhysRevB.104.134415.

[67] J. Atalaya, J. Clarke, G. Schön, and A. Shnirman. Flux $1/f^{\alpha}$ noise in two-dimensional Heisenberg spin glasses: Effects of weak anisotropic interactions. *Phys. Rev. B*, 90:014206, 2014. URL http://doi.org/10.1103/PhysRevB.90.014206.

[68] P. M. Chaikin and T. C. Lubensky. *Principles of Condensed Matter Physics*. Cambridge University Press, Cambridge, U.K., 1995. ISBN 0521794501. URL https://books.google.ca/books?id=lAohAwAAQBAJ.

[69] B.I. Halperin and P.C. Hohenberg. Generalization of scaling laws to dynamical properties of a system near its critical point. *Phys. Rev. Lett.*, 19:700, 1967. URL http://doi.org/10.1103/PhysRevLett.19.700.

[70] F. Bloch. Nuclear induction. *Phys. Rev.*, 70:460–474, 1946. URL http://doi.org/10.1103/PhysRev.70.460.

[71] Shnirman A., Schön G., Martin I., and Makhlin Y. Low- and high-frequency noise from coherent two-level systems. *Phys. Rev. Lett.*, 94:127002, 2005. URL http://doi.org/10.1103/PhysRevLett.94.127002.

[72] J. H. Van Vleck. Paramagnetic relaxation times for titanium and chrome alum. *Phys. Rev.*, 57:426, 1940. URL https://doi.org/10.1103/PhysRev.57.426.

[73] R. de Sousa and S. Das Sarma. Gate control of spin dynamics in III-V semiconductor quantum dots. *Phys. Rev. B*, 68:155330, 2003. URL https://doi.org/10.1103/PhysRevB.68.155330.

[74] F. C. Wellstood, C. Urbina, and J. Clarke. Low frequency noise in dc superconducting quantum interference devices below 1 K. *Appl. Phys. Lett.*, 50:772, 1987. URL https://doi.org/10.1063/1.98041.

[75] T. Zaborniak and R. de Sousa. Benchmarking Hamiltonian Noise in the D-Wave Quantum Annealer. *IEEE Trans. Quantum Eng.*, 2:3100206, 2021. URL https://ieeexplore.ieee.org/document/9319535.

[76] D. C. Mattis and J. Bardeen. Theory of the anomalous skin effect in normal and superconducting metals. *Phys. Rev.*, 111:412–417, Jul 1958. doi: 10.1103/PhysRev.111.412. URL https://link.aps.org/doi/10.1103/PhysRev.111.412.

[77] J. Aumentado, Mark W. Keller, John M. Martinis, and M. H. Devoret. Nonequilibrium quasiparticles and $2e$ periodicity in single-cooper-pair transistors. *Phys. Rev. Lett.*, 92:066802, Feb 2004. doi: 10.1103/PhysRevLett.92.066802. URL https://link.aps.org/doi/10.1103/PhysRevLett.92.066802.

[78] K. Serniak, M. Hays, G. de Lange, S. Diamond, S. Shankar, L. D. Burkhart, L. Frunzio, M. Houzet, and M. H. Devoret. Hot nonequilibrium quasiparticles in transmon qubits. *Phys. Rev. Lett.*, 121:157701, Oct 2018. doi: 10.1103/PhysRevLett.121.157701. URL https://link.aps.org/doi/10.1103/PhysRevLett.121.157701.

[79] R. Barends et al. Minimizing quasiparticle generation from stray infrared light in superconducting quantum circuits. *Appl. Phys. Lett.*, 99:113507, 2011. URL https://doi.org/10.1063/1.3638063.

[80] S. Diamond, V. Fatemi, M. Hays, H. Nho, P. D. Kurilovich, T. Connolly, V. R. Joshi, K. Serniak, L. Frunzio, L. I. Glazman, and M. H. Devoret. Distinguishing parity-switching mechanisms in a superconducting qubit. *PRX Quantum*, 3:040304, Oct 2022. doi: 10.1103/PRXQuantum.3.040304. URL https://link.aps.org/doi/10.1103/PRXQuantum.3.040304.

[81] A.P. Vepsäläinen, A.H. Karamlou, J.L. Orrell, et al. Impact of ionizing radiation on superconducting qubit coherence. *Nature*, 584:551–556, 2020. doi: 10.1038/s41586-020-2619-8. URL https://doi.org/10.1038/s41586-020-2619-8.

[82] Thomas Connolly, Pavel D. Kurilovich, Spencer Diamond, Heekun Nho, Charlotte G. L. Bøttcher, Leonid I. Glazman, Valla Fatemi, and Michel H. Devoret. Coexistence of nonequilibrium density and equilibrium energy distribution of quasiparticles in a superconducting qubit. *Phys. Rev. Lett.*, 132:217001, May 2024. doi: 10.1103/PhysRevLett.132.217001. URL https://link.aps.org/doi/10.1103/PhysRevLett.132.217001.

[83] T. Yamamoto, Y. Nakamura, Yu. A. Pashkin, O. Astafiev, and J. S. Tsai. Parity effect in superconducting aluminum single electron transistors with spatial gap profile controlled by film thickness. *Applied Physics Letters*, 88(21):212509, 05 2006. ISSN 0003-6951. URL https://doi.org/10.1063/1.2207555.

[84] P. J. de Visser, D. J. Goldie, P. Diener, S. Withington, J. J. A. Baselmans, and T. M. Klapwijk. Evidence of a nonequilibrium distribution of quasiparticles in the microwave response of a superconducting aluminum resonator. *Phys. Rev. Lett.*, 112:047004, Jan 2014. doi: 10.1103/PhysRevLett.112.047004. URL https://link.aps.org/doi/10.1103/PhysRevLett.112.047004.

[85] R. P. Budoyo, J. B. Hertzberg, C. J. Ballard, K. D. Voigt, Z. Kim, J. R. Anderson, C. J. Lobb, and F. C. Wellstood. Effects of nonequilibrium quasiparticles in a thin-film superconducting microwave resonator under optical illumination. *Phys. Rev. B*, 93:024514, Jan 2016. doi: 10.1103/PhysRevB.93.024514. URL https://link.aps.org/doi/10.1103/PhysRevB.93.024514.

[86] F. Luthi, T. Stavenga, O. W. Enzing, A. Bruno, C. Dickel, N. K. Langford, M. A. Rol, T. S. Jespersen, J. Nygård, P. Krogstrup, and L. DiCarlo. Evolution of nanowire transmon qubits and their coherence in a magnetic field. *Phys. Rev. Lett.*, 120:100502, Mar 2018. doi: 10.1103/PhysRevLett.120.100502. URL https://link.aps.org/doi/10.1103/PhysRevLett.120.100502.

[87] Reprinted figure with permission from K. Serniak, M. Hays, G. de Lange, S. Diamond, S. Shankar, L. D. Burkhart, L. Frunzio, M. Houzet, and M. H. Devoret. Hot nonequilibrium quasiparticles in transmon qubits. *Phys. Rev. Lett.*, 121:157701, Oct 2018. doi: 10.1103/PhysRevLett.121.157701. URL https://link.aps.org/doi/10.1103/PhysRevLett.121.157701 , Copyright 2024 by the American Physical Society.

[88] Reprinted from A.P. Vepsäläinen, A.H. Karamlou, J.L. Orrell, et al. Impact of ionizing radiation on superconducting qubit coherence. *Nature*, 584:551–556, 2020. doi: 10.1038/s41586-020-2619-8. URL https://doi.org/10.1038/s41586-020-2619-8 , with the permission of Springer Nature Publishing.

[89] Gao J. The physics of superconducting microwave resonators, 2008. URL https://thesis.library.caltech.edu/2530/.

[90] F. Yan, S. Gustavsson, A. Kamal, et al. The flux qubit revisited to enhance coherence and reproducibility. *Nat Commun*, 7:12964, 2016. doi: https://doi.org/10.1038/ncomms12964. URL https://link.aps.org/doi/10.1038/ncomms12964.

[91] T. Lanting, M. H. S. Amin, M. W. Johnson, F. Altomare, A. J. Berkley, S. Gildert, R. Harris, J. Johansson, P. Bunyk, E. Ladizinsky, E. Tolkacheva, and D. V. Averin. Probing high-frequency noise with macroscopic resonant tunneling. *Phys. Rev. B*, 83:180502(R), 2011. URL https://doi.org/10.1103/PhysRevB.83.180502.

[92] L. P. Kadanoff and P. C. Martin. Hydrodynamic equations and correlation functions. *Ann. Phys.*, 24:419, 1963. URL https://doi.org/10.1016/0003-4916(63)90078-2.

[93] Zi-Huai Zhang, Kadircan Godeneli, Justin He, Mutasem Odeh, Haoxin Zhou, Srujan Meesala, and Alp Sipahigil. Acceptor-induced bulk dielectric loss in superconducting circuits on silicon, 2024. URL https://doi.org/10.48550/arXiv.2402.17155.

[94] A. P. M. Place, L. V. H. Rodgers, P. Mundada, et al. New material platform for superconducting transmon qubits with coherence times exceeding 0.3 milliseconds. *Nat Commun*, 12:1779, 2021. doi: 10.1038/s41467-021-22030-5. URL https://doi.org/10.1038/s41467-021-22030-5.

[95] J. M. Martinis. Surface loss calculations and design of a superconducting transmon qubit with tapered wiring. *npj Quantum Inf*, 8:26, 2022. doi: 10.1038/s41534-022-00530-6. URL https://doi.org/10.1038/s41534-022-00530-6.

APPENDIX A

Generalized Fluctuation-Dissipation Theorem

This appendix introduces fundamental concepts of linear response theory and derives the fluctuation-dissipation theorem, a key result utilized throughout this work. Additionally, we present a generalization of this theorem and justify its application to quasithermal distributions as in chapter 7.

Assume a system described by a hamiltonian $\mathcal{H}_0$ is perturbed by an external Hamiltonian $\mathcal{H}_{\text{ext}} = -F(t)\hat{\xi}$ with $\hat{\xi}$ an observable of interest coupled to its conjugate field $F(t)$. The *susceptibility operator* $\hat{\chi}_\xi$ is defined according to linear-response theory: $\hat{\xi}_{F\neq 0}(t) - \hat{\xi}_{F=0}(t) = \int_{-\infty}^{\infty} dt' \hat{\chi}_\xi(t-t')F(t')$. From time-dependent perturbation theory: $\hat{\chi}_\xi(t-t') = \frac{i}{\hbar}\theta(t-t')[\hat{\xi}(t), \hat{\xi}(t')]$, $\hat{\xi}$ here defined in the interaction picture. Using this result we can write

$$\hat{\tilde{\chi}}_\xi(\omega) = \frac{1}{2\pi\hbar}\int_{-\infty}^{\infty} d\omega' \frac{[\hat{\tilde{S}}_\xi(-\omega')]^\dagger - \hat{\tilde{S}}_\xi(\omega')}{\omega - \omega' + i\eta}, \tag{A.1}$$

where $\hat{S}_\xi(t) = [\hat{\xi}(t) - \langle\hat{\xi}(t)\rangle_{\hat{\rho}}][\hat{\xi}(0) - \langle\hat{\xi}(0)\rangle_{\hat{\rho}}]$ is the *correlation operator*, $\hat{\tilde{S}}_\xi(\omega) = \int_{-\infty}^{\infty} dt e^{i\omega t}\hat{S}_\xi(t)$ its Fourier transform and $\langle\hat{O}\rangle_{\hat{\rho}} = \text{Tr}\{\hat{\rho}\hat{O}\}$ is the thermal average of $\hat{O}$ assuming the density matrix $\hat{\rho}$ is time-independent. Taking the imaginary part of the thermal average of equation (A.1) we get a generalized version of the fluctuation dissipation theorem:

$$2\hbar\text{Im}\left(\langle\hat{\tilde{\chi}}_\xi(\omega)\rangle_{\rho(E)}\right) = \langle\hat{\tilde{S}}_\xi(\omega)\rangle_{\rho(E)} - \langle\hat{\tilde{S}}_\xi(\omega)\rangle_{\rho(E+\hbar\omega)}, \tag{A.2}$$

where we used the result $\langle[\hat{\tilde{S}}(-\omega')]^\dagger\rangle_{\rho(E)} = \langle\hat{\tilde{S}}(\omega)\rangle_{\rho(E+\hbar\omega)}$, valid if the density matrix is diagonal in the basis formed by the energy eigenstates $\{|E\rangle\}$ of $\mathcal{H}_0$: $\langle E|\hat{\rho}|E'\rangle = \rho(E)\delta_{E,E'}$ with $\rho(E)$ a real

function. Note that in equation (A.2), $\langle\hat{\tilde{\chi}}_\xi(\omega)\rangle_{\rho(E)}$, $\langle\hat{\tilde{S}}_\xi(\omega)\rangle_{\rho(E)}$ are the usual susceptibility and power spectral density (PSD) of $\hat{\xi}$, respectively, the notation makes their dependence on $\rho(E)$ explicit. Having information about the density matrix allows us to link the fluctuations in the system to its reaction to external forces.

When $\rho(E)$ is of the form $\rho(E) \propto e^{-E/(k_B T)}$ as is the case in thermal or quasithermal systems, Eq. (A.2) is reduced to the known fluctuation-dissipation theorem:

$$\langle\hat{\tilde{S}}_\xi(\omega)\rangle = 2\hbar\left[n_B(\omega)+1\right]\mathrm{Im}\left(\langle\hat{\tilde{\chi}}_\xi(\omega)\rangle\right), \tag{A.3}$$

where $n_B(\omega)$ is the Bose-Einstein distribution. Note that in the main text we simply write $\langle\hat{\tilde{\chi}}_\xi(\omega)\rangle_{\rho(E)} \equiv \tilde{\chi}_\xi(\omega)$, $\langle\hat{\tilde{S}}_\xi(\omega)\rangle_{\rho(E)} \equiv \tilde{S}_\xi(\omega)$.